Technical Report
TR-22-01
September 2022

Analysis of corrosion products on filter housings in the Lasgit field experiment

Erik Wendel
Andrew Gordon
Eric Börjesson
Alexander Wärnheim
Erik Bergendal
Johannes Johansson
Daniel Svensson

SVENSK KÄRNBRÄNSLEHANTERING AB

SWEDISH NUCLEAR FUEL
AND WASTE MANAGEMENT CO

Box 3091, SE-169 03 Solna
Phone +46 8 459 84 00
skb.se

SVENSK KÄRNBRÄNSLEHANTERING

ISSN 1404-0344
SKB TR-22-01
ID 1970892
September 2022

Analysis of corrosion products on filter housings in the Lasgit field experiment

Erik Wendel, Andrew Gordon, Eric Börjesson, Alexander Wärnheim
RISE Research Institutes of Sweden

Erik Bergendal, Johannes Johansson, Daniel Svensson
Svensk Kärnbränslehantering AB

This report is published on www.skb.se

Summary

Large scale gas injection test (Lasgit) was a field experiment purposed to study gas transport in (artificially) hydrated bentonite in a repository-like environment in the Äspö Hard Rock laboratory (HRL). The project addressed uncertainties pertaining to the scalability in previously reported lab-scale experiments. The Lasgit canister (full-size, albeit with modified components) was installed in 2005 at the −420 m level in Äspö HRL, after which a series of sequences of artificial hydration and gas injection followed. The Lasgit canister was retrieved in the beginning of 2021. Corrosion analyses were performed on a series of copper components, housing the filters installed in the canister mantel, and used for gas injection. The extent of corrosion on the analysed copper housings was low and in accordance with experience from previous field experiments. A thin layer of corrosion products and shallow pits or defects were observed in analysis of sample cross-sections. Cuprite and malachite were identified on filter housings. Paratacamite was identified in a scrape sample from the canister surface, however, this corrosion product was concluded to have formed after the field experiment and retrieval of the canister.

Sammanfattning

Large scale gas injection test (Lasgit) var ett fältförsök utformat för att studera gastransport i artificiellt vattenmättad bentonit under förvarsliknande förhållanden vid Äspölaboratoriet. Vid tidigare laboratoriestudier av gastransport har det funnits osäkerheter kring resultatens skalbarhet och tillförlitlighet i fullskala, vilket Lasgit-försöket adresserar. Lasgit-kapseln, en fullstor kapsel (med i vissa avseenden modifierade komponenter) installerades 2005 vid 420 meters djup i Äspölaboratoriet. Därpå följde en försöksserie med varierad artificiell vätning av, och gasinjicering i bentoniten. Kapseln återtogs i början av 2021. Korrosionsanalyser utfördes på ett antal filterhållare (filterhus) av koppar, installerade i kapselns utsida. Omfattningen av kopparkorrosion på filterhusen bedöms som låg och i enighet med erfarenhet från tidigare fältförsök. Ett tunt lager korrosionsprodukter och grunda gropar eller defekter kunde observeras vid tvärsnittsanalys. Kuprit och malakit kunde identifieras på filterhusen. Paratakamit identifierades i ett skrapprov från kapselns yta, noteras bör dock att det kan konstateras att denna korrosionsprodukt hade bildats först efter försökets avslut och kapselns återtag från deponeringshålet.

Contents

1 Introduction

Lasgit, or large scale gas injection test, was a field test conducted at the Äspö Hard Rock laboratory (HRL) to investigate gas transport in compacted and (artificially) hydrated bentonite under unheated (but otherwise repository-like) conditions for 16 years (Harrington et al. 2008, Cuss et al. 2010). A final project report is provided in Cuss et al. (2022)

This report primarily presents the findings from the examination of a selection of copper components from the Lasgit canister. The purpose of performing the corrosion analyses is to gather more information about the corrosion mechanisms that can occur under repository-like conditions. In addition to the analysis of the canister components, a sample of corrosion products from the Lasgit canister mantle area was characterised. Also, iron corrosion products on the canister insert – resulting from an initially opened valve in the canister base – were analysed for presence of microorganisms able to conduct microbially influenced corrosion (MIC).

1.1 Background and objectives

Lasgit was primarily undertaken to address issues pertaining to previously performed lab-scale tests, notably the sensitivity of the gas migration process to experimental boundary conditions and the possible scale-dependency of measured responses in lab-scale experiments (Harrington and Horseman 2003). The Lasgit field experiment included full-size, albeit modified, components. The copper shell of a full scale KBS-3 canister was fitted with a total of 13 filter assemblies composed of porous brass filters mounted in copper (C103/Cu-OF) housings. The filter assemblies (brass filter and copper housing) were used for pore water pressure measurements, with gas and hydraulic injection through separate tubing for each filter assembly. The copper tube used in Lasgit was T34, which originally was produced in cooperation with Posiva as part of a manufacturing test. This tube is further described in Nieminen and Pihlainen (2001) and Koivula and Pihlainen (2003). The copper shell, insert, and filter housings prior to deposition are shown in Figure 1-1.

The T34 had been used earlier and had a stained appearance, whereas the filter housings were specifically manufactured for the Lasgit project and had a pristine appearance upon deposition. The filter housings (copper housings without the brass filter) were thus deemed most suitable for the analysis of corrosion products formed during the course of the experiment, and were chosen as the main focus to be investigated – despite the lack of pre-characterisation of the filter housings before deposition. The extent of corrosion and expected corrosion products could be compared with previously retrieved field experiments, such as LOT, ABM, Prototype, and Febex (Gordon et al. 2018, Taxén et al. 2012, Johansson et al. 2020, Wersin et al. 2017). From this comparison, cuprite (Cu_2O) is expected to be the main corrosion product, possibly with formation of some Cu(II) corrosion product, e.g. paratchamite or malachite, and possibly also with some small amount of copper sulfide. Based on the same comparison, the extent of general corrosion is expected to be in the range of 1–10 micrometres. While reducing conditions are expected to establish before full saturation of the bentonite clay in the vast majority of deposition holes in the spent fuel repository, the Lasgit experiment was saturated at the start of the experiment and may thus have been in a initially weakly oxidizing and saturated state. This is in contrast to most other field tests, e.g. LOT and Prototype, which were unsaturated at the start of the tests, but comparable with ABM, in which an artificial hydration system was applied (Gordon et al. 2018).

The filter assemblies were placed in groups of four at three heights on the canister mantle with each filter displaced to its nearest radial and axial neighbor by 90° and 45°, respectively, as depicted in Figure 1-2. The upper, middle, and lower filter rows are denoted as UFA1–4, MPFA1–4, and LFA1–4, respectively, corresponding to identifications FU909–912, FM905–908, and FL901–904 used in Cuss et al. (2010). At the base of the canister, a 13th filter assembly was placed, in communication with the empty canister volume through a gas-actuated valve (in this report denoted PC901 and named FC901 in Cuss et al. (2010)). A detailed outline of the Lasgit experiment is provided in the summary report Cuss et al. (2010).

Figure 1-1. *The canister used in the Lasgit experiment. A full-size canister and cast iron insert was used (a). 12 filter assemblies (b) where placed in recesses on the canister surface (c). A 13th filter assembly was situated at the base of the canister. Filters and 45° markings along the canister are visible together with pipework through the canister lid, in the top view in (d).*

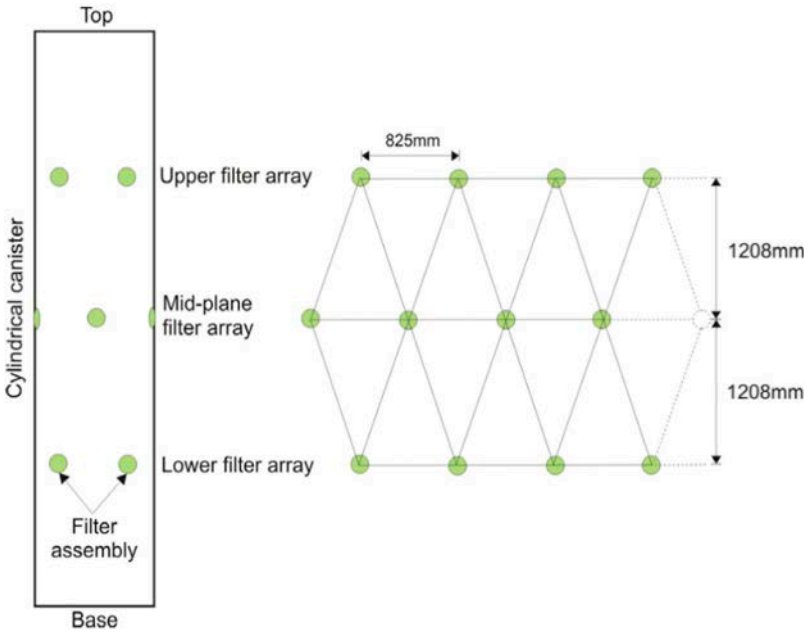

Figure 1-2. *Schematic side view of canister and visible filters (shown in green). The right-hand graphic is a 2D representation of the canister surface showing the relative positions of the 12 injection filters.*

1.2 Physicochemical environment

The deposition hole was sealed on experiment day 0 on February 1 in 2005. At this time the deposition hole was flushed with water to remove air trapped in engineering voids. Throughout the first years (1 385 days) of the Lasgit experiment, a series of stages with artificial hydration and gas injection was conducted. The pre-compacted bentonite was saturated to 95.1–99.7 % before deposition. After deposition, and before the first stage of artificial hydration, groundwater inflow through discrete fractures initiated saturation of the bentonite, however, this also lead to piping, bentonite extrusion and discharge of groundwater in the tunnel, requiring the installation of two pressure-relief holes. During the first stage of artificial hydration (experiment days 108–843), water was injected from a nearby sealed borehole through all twelve filters on the canister surface. The high degree of initial saturation, the flushing of water during installation and the artificial hydration through the canister filters should have ensured the bentonite in Lasgit was fully saturated in a very early phase of the experiment. This is especially true for the bentonite close to the filter houses. However, the recorded pore pressure inside the bentonite and the suction below and above the canister showed that hydraulic equilibrium was not reached during the first three years. During the first 20 days of artificial hydration, the valve connected to the filter at the base of the canister was unintentionally left open. This resulted in an inlet of water into the canister, which provided a corrosive environment for the iron insert. After the first 20 days of artificial hydration, the valve was closed and no more water is expected to have entered the canister. The corrosion following this initial water inlet into the insert is further detailed below. Following the first stage of artificial hydration, the first stage of hydraulic and gas injection started on day 843, and finished on day 1 110. During this stage, artificial hydration continued through the filters in the middle and upper filter arrays on the canister mantle. In the lower filter array, gas injection started trough the filter LFA3 on day 917. The second stage of artificial hydration took place between days 1 110 and 1 385. Cuss et al. (2010) provides an in-depth description and analysis of the saturation, gas injection and migration, and pressure and stress evolution during the first 1 385 days of the Lasgit experiment. After the first gas injection test, the hydraulic properties were tested in the same filter and the results showed that the gas passage had led to no changes in the hydraulic properties of the bentonite. In total, six gas injection tests were performed in the filters on the canister surface: four in one filter in the lower array (LFA3) and two in a filter in the upper array (UFA2). Finally, one gas test was performed through a filter in the base of the canister.

For the first 1 385 days (3.5 years) of the Lasgit experiment, the temperature around the −420 m level in the Äspö HRL followed seasonal variations between 10 and 16 °C, while the canister temperature only varied by ±0.5 °C from 13.3 °C. This temperature is expected to have been maintained until retrieval, which started on September 2, 2020 and the canister was retrieved from the deposition hole on January 25, 2021.

After excavation the bentonite in the deposition hole was extensively sampled, ~1 500 samples in the blocks and ~400 in the pellets, and tested for water content and dry density. The results are reported in the final report for Lasgit (Cuss et al. 2022).

1.3 Retrieval and samples

The work to retrieve the Lasgit canister was carried out between September 2, 2020 to January 25, 2021. After removing and sampling the bentonite surrounding the canister, it was lifted form the deposition hole on January 25, 2021, after which it was kept in the Äspö HRL tunnels for approximately one month before being transported to the Canister Laboratory for sampling, measuring, and disassembly. During the time the canister was kept in the Äspö HRL tunnels, it was subject to the ambient tunnel atmosphere, with a temperature of 10–16 °C and a relative humidity of 52–82 %RH (see Appendix B). Visual examination and documentation of the Lasgit canister was made by SKB staff in the Äspö HRL during retrieval of the canister and again approximately one month later at the Canister Laboratory. A few images from the retrieval are presented in Figure 1-3, showing a filter assembly (UFA1) attached to the canister, the removal of a filter assembly (PC901), and the full size canister at the Canister Laboratory, after retrieval and removal of the insert. During retrieval of the Lasgit canister, as the filter assemblies were revealed from the bentonite, they were sealed from the tunnel atmosphere with plastic films to protect the surfaces and to some degree limit further oxidation. After removal from the canister, selected filter assemblies were place in air-tight bags filled with inert gas, and sent to

RISE in Kista in February 2021 for analysis. It should be noted that most of these bags were observed to be perforated upon arrival at RISE for corrosion analysis, as depicted in Appendix A. How the perforation of the transport bags occurred has not been uncovered. The importance of this for the asessment of oxic corrosion is expected to be minor, as the filter assemblies were subject to – at least partially – oxic conditions already upon removal of the surrounding bentonite in the deposition hole. The plastic film in the deposition hole and transport bags have rather filled the purpose to protect the surfaces from further physical damage (i.e scratches) that could influence the subsequent analysis. Samples taken from the corroded iron insert were sent to Microbial Analytics for analysis of the microbial populations present.

The filter house surfaces were analyzed with Scanning Electron Microscopy (SEM) with Energy-Dispersive X-ray Spectroscopy (EDS); X-ray Diffraction (XRD); and Fourier-Transform Infrared Spectroscopy (FTIR) with Infrared Reflection Absorption Spectroscopy (IRRAS). Filter housing cross section samples were analyzed with SEM/EDS. The purpose of the analyses was to characterize the form and extent of corrosion, which had occured during the field exposure.

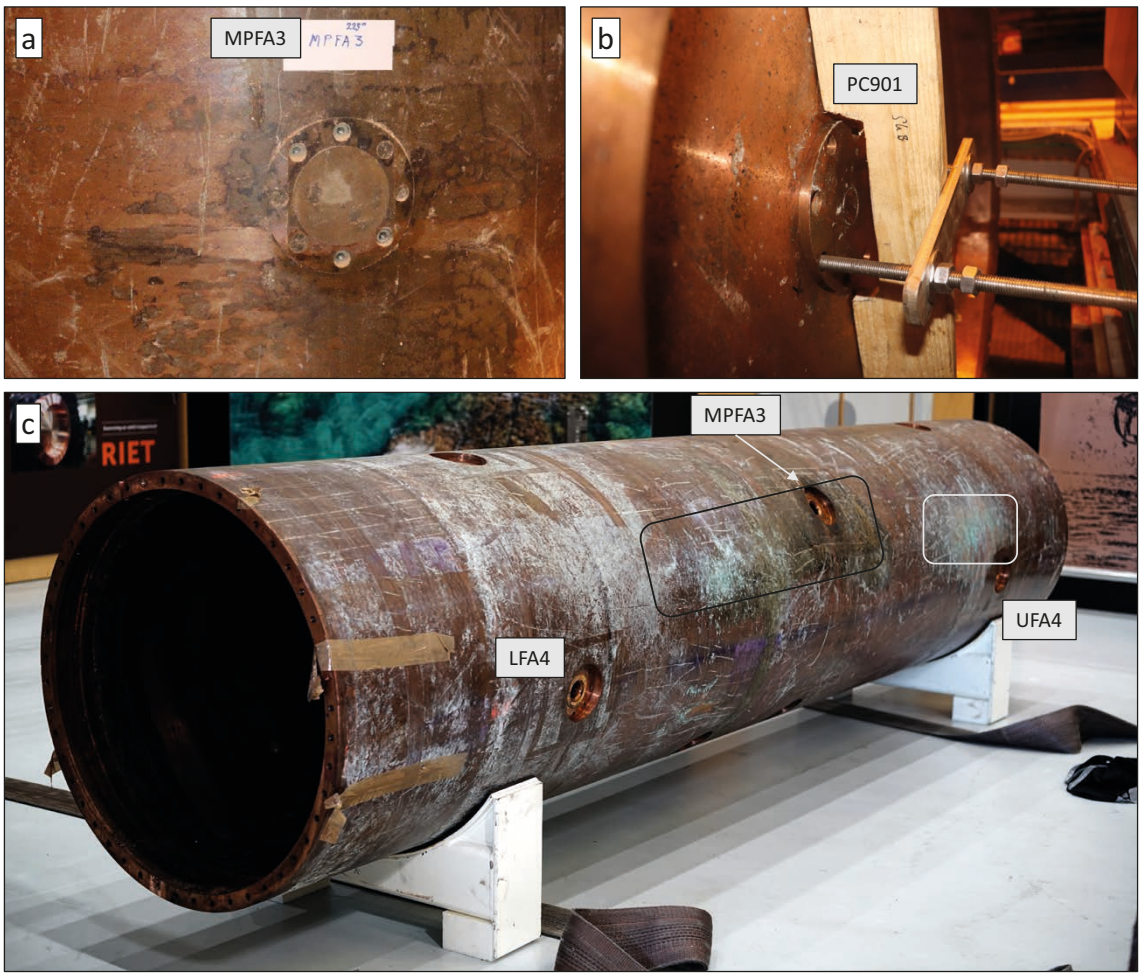

Figure 1-3. *Images of (a) the Lasgit canister upon retrieval with filter assembly still in place, (b) removal of filter assembly (PC901), and (c) the Lasgit canister after removal of the cast iron insert and filter assemblies. A sample of corrosion products on the canister surface was extracted from the area marked with a light grey rectangle to the right in image (c). Further details are provided in the results section below.*

2 Materials and methods

Upon arrival at RISE, the filter housings were unpacked and documented with photography. The filter housings were stored before and between analyses in a containment tent continuously purged with nitrogen gas to maintain an atmosphere of low oxygen level. This was done despite the fact that the filter housings had almost certainly been in contact with air during transport due to the perforation of the foil bags they were delivered in.

One copper filter housing from each row of filter assemblies (copper filter housing and brass filter) at the Lasgit canister was investigated. In addition, the filter housing situated on the base of the Lasgit canister was investigated. Altogether, the following four filter housings were investigated, originally situated from top to base on the Lasgit canister, UFA4, MPFA1, LFA2, and PC901. First, four smaller sample pieces were extracted from the filter housings by dry cutting. Three of the four samples were chosen for surface analysis with SEM/EDS, XRD and FTIR/IRRAS. The fourth sample was prepared for cross sectional analysis in SEM/EDS. Second, on each smaller sample, representative areas or sites were chosen for analysis. A sample overview can be seen in Table 2-1.

Table 2-1. Overview for the sampling and analyses of each of the four filter housings UFA4, MPFA1, LFA2, and PC901.

Filter housing			
Sample 1	**Sample 2**	**Sample 3**	**Sample 4**
SEM/EDS XRD FTIR/IRRAS	SEM/EDS XRD FTIR/IRRAS	SEM/EDS XRD FTIR/IRRAS	SEM/EDS cross-sect.

2.1 SEM/EDS

SEM/EDS analysis was performed in Zeiss Sigma 3000VP. The electron beam energy used was 10–20 keV and the working distance around 8.5 mm. Secondary electron detector was used for images and a backscatter detector was used for EDS, which was used for obtaining contrast in elemental analysis. The EDS method is semi-quantitative and the accuracy of the measurements is therefore hard to define, but generally the detection limits are approximately 0.1 % and in optimal conditions (a sample with homogenous properties) the error for each element is less than 5 %. Carbon is removed from the EDS results as it is assumed to be a contaminant which reduces the signal of the rest of the results. In the cross section analysis, the samples were first analysed after dry grinding. The silicon carbide particles from the grinding paper were leaving marks and the particles adhered to the copper surface, and therefore the surfaces were analysed one more time with wet polishing. A comparison of the surfaces can be seen in Figure 2-1 where A is the dry polished cross section from filter housing LFA2 and B is the same cross section after wet polishing.

2.2 XRD

XRD analysis at RISE was carried out in a Bruker D8 Discover. Data was collected between 4° and 110° (2θ) with a copper Kα beam of 1.5418 Å. Measurements were obtained down to a depth of approximately 5 µm. For peak assignments, the Crystallography Open Database (COD) was used together with the American Mineralogist Crystal Structure Database (Vaitkus et al. 2021, Quirós et al. 2018, Merkys et al. 2016, Gražulis et al. 2009, 2012, 2015, Downs and Hall-Wallace 2003).

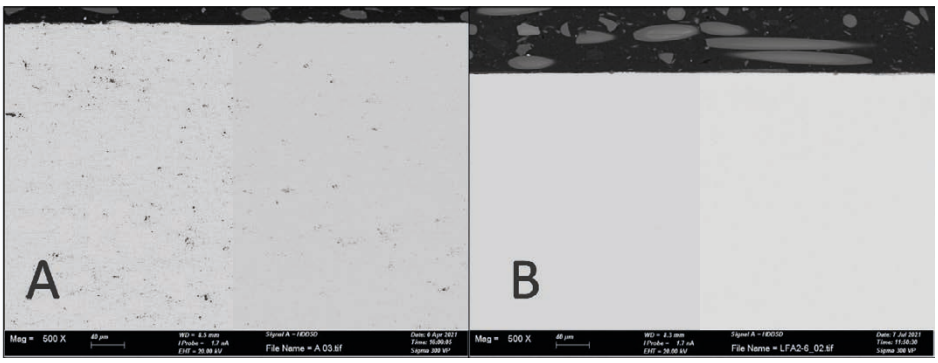

Figure 2-1. *A comparison between a dry polished surface A) and a wet polished surface B) from filter housing LFA2. The left-hand side of each image has been treated by (equally) increasing the black–white contrast, to highlight the difference in surface finish between the samples.*

For XRD analysis of green-blue copper corrosion products, sampling from the surface of the Lasgit canister was done using a sharp plastic object. Sampling was done from the area marked with a grey rectangle in Figure 1-3. The sample was photographed in an optical microscope and presented in Figure 2-2, which showed what appeared to be a couple of different phases. The sample was milled to a powder by hand, in an agate mortar. XRD analysis of the milled copper corrosion products samples from the canister surface, were performed at the Äspö Hard Rock Laboratory, using a Panalytical XPert diffractometer with a Co X-ray tube (1.789 Å), and a PIXcel detector. A programmable divergence slit was used, and data was collected between 4 and 100° (2θ) for approximately 15 minutes. A zero background silicon substrate was used as a sample holder. The Panalytical Highscore software was used for data evaluation including the database of reference data, as well as for plotting.

Figure 2-2. *Copper corrosion products scraped from the Lasgit canister after retrieval at the Canister Laboratory. Sampling was made from the area marked with a grey rectangle in Figure 1-3c.*

2.3 FTIR/IRRAS

FTIR/IRRAS analysis was carried out in Vertex 70 coupled with a Hyperion 3000 accessory. IRRAS is a molecular spectroscopy technique, based on FTIR that is often used to determine the chemical composition of thin films with high sensitivity. Each measurement acquired the IR spectra of an area of approximately 200 × 200 µm. Griffiths and de Haseth (2007), Malvault et al. (1995), Socrates (1994), and internal reference materials were used for peak assignmenets.

2.4 X-ray fluorescence (XRF) spectroscopy

In order to determine the chemical composition of the green-blue corrosion products sampled from the mantle area of the canister surface, the ground copper corrosion products were analyzed with XRF at Äspö Hard Rock Laboratory. The equipment used was a Panalytical Epsilon spectrometer using a Rh X-ray tube. The measurement setup and evaluation were the standard provided from the manufacturer (called Omnian). The sample was placed on a mylar foil as a powder during the measurement. The XRF does not measure elements with atomic number lower than sodium, and due to the mylar foil used in this case, sodium could not be measured for the scraping sample. The reported elements are reported as oxides and the sum is normalized to 100 %, however minor elements are sometimes excluded as a simplification of the dataset.

2.5 Microbially influenced corrosion of the iron insert

A valve connected to a filter housing at the base of the canister was open for the first approximately 20 days of artificial hydration. As a consequence, stagnant water accumulated in the canister insert. This resulted in extensive corrosion at the base of the insert, as demonstrated in Figure 2-3 a–e. The water entered the canister through a roughly 30 cm long metal tube (Figure 2-3 f), and the rust layer (consistently around 7 cm and a maximum of around 15 cm) in Figure 2-3 b–c indicates that the water level was never that high. It can therefore be assumed that all water which entered the canister through the open filter housing, actually stayed in the canister throughout the field experiment – it did not exit back through the tube. The canister was placed horizontally in the deposition tunnel after retrieval from the deposition hole, during this time, it is possible the remainder of the accumulated water could have seeped out of the canister or evaporated, as the filter assemblies had then been removed. The iron corrosion products were not characterized chemically, however, samples of moist corrosion products and surface deposits were taken to be analysed for the possible presence of microorganisms potentially influencing the corrosion.

The presence of microorganism able to conduct MIC was analysed by the QuantArray®-MIC, provided by Microbial Insights, USA, through Micans (Microbial Analytics Sweden), Sweden. The method provides an estimate of MIC activity by quantitative analysis of DNA of specific microbes relating to MIC. The following samples were collected on April 14, 2021:

- Sample 1 (Water): <5 mL murky water, which was left in the canister upon opening the canister base.
- Sample 2 (Cast iron insert): approximately 20–30 mL solid corrosion products collected from the corroded cast iron insert. The sample included red and dark sheets and powdered corrosion products.
- Sample 3 (Copper canister): <5 mL dark corrosion products collected from the inside of the canister base. Due to the thin nature of the corrosion product/surface deposit, a relatively large area was required for sampling.

The samples were handled by Micans, and analysis was performed by Microbial Insights.

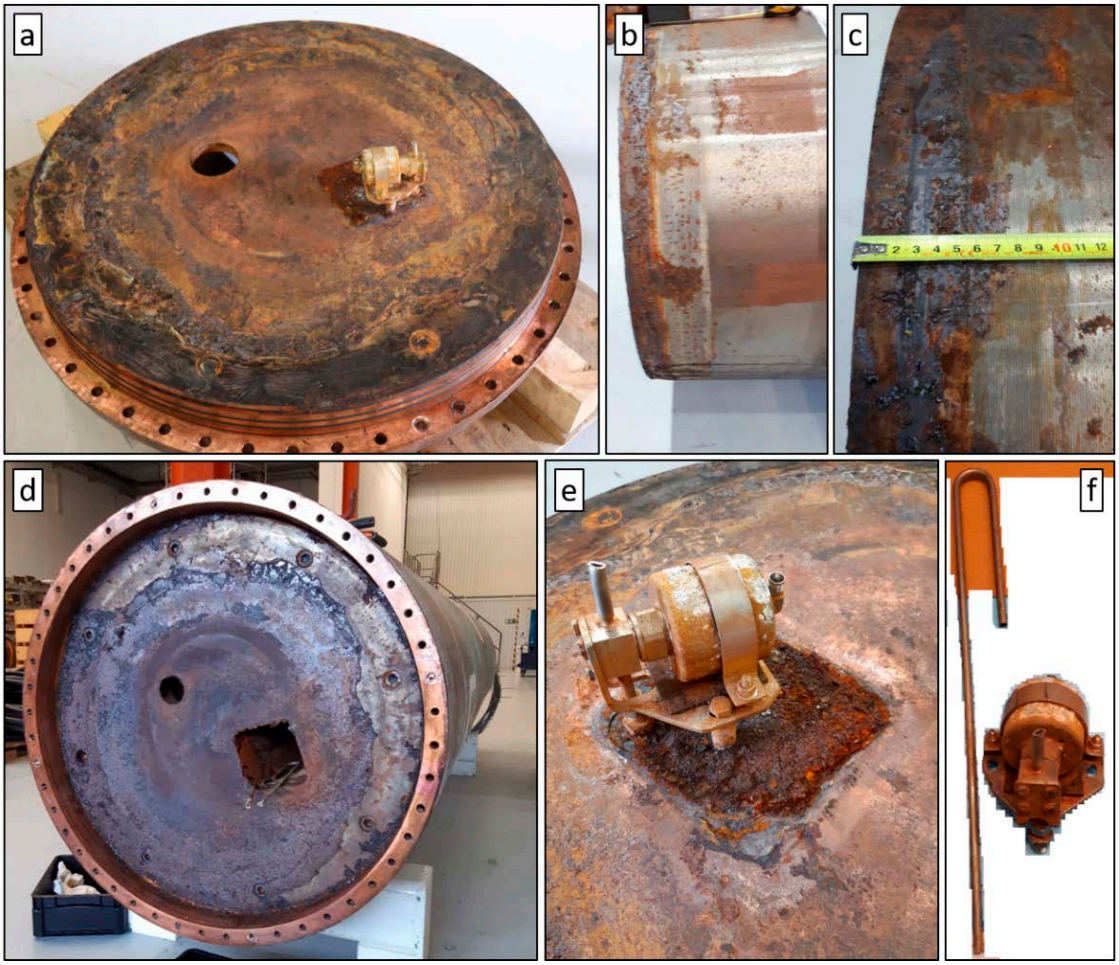

Figure 2-3. *Images showing (a) the inside of the copper canister base, (b) the base of the cast iron insert (from side), (c) close-up of the base of the cast iron insert (from side) with measuring tape showing the extent of cast iron corrosion from the open valve, (d) cast iron insert base (from below), (e) a close-up of the valve which leaked water, (f) and a side-by-side view of the valve and appurtenant metal tube. Images (a) and (d) show the circular hole connected to the filter assembly and the square-shaped hole for the opened valve. Samples for MIC-analysis were collected from the base of the cast iron insert (d), from the inside of the canister base (a), and from a small volume of residual water which was present upon removal of the canister base. In the left-hand side of image (e) is the cut off metal tube through which the water entered the canister, also shown with the filter valve in in image (f). This metal tube extended roughly 30 cm into the canister, thus no water exited the canister this way.*

3 Results

3.1 Sample overview

The sample filter housings were removed from their bags to be inspected and photographed and then placed in a nitrogen tent. The four filter housings that were chosen for analysis A) PC901, B) MPFA1, C) LFA2, D) UFA4, are shown below in Figure 3-1. The sample preparation performed for the surface samples included dry cutting smaller sample coupons to match analysis instrument dimensions. The cross section samples were in addition to dry cutting also cast into epoxy resin and polished.

3.2 PC901

Figure 3-2 depicts an overview of filter housing PC901 with the designated area for sample coupons marked with a black rectangle. The selected area was chosen due to its diverse – yet representative – appearance. After dry cutting, one sample coupon was chosen for cross section analysis with SEM/EDS. The surface of the other three coupons were analyzed in SEM/EDS, XRD and FTIR/IRRAS. An overview of the four sample coupons from filter housing PC901 can be seen in Figure 3-3 along with their designated surface analysis sites, marked with red rectangles and a dashed red line indicating where the cross section sample was cut. The sites were selected to enclose areas of diverse appearance in order to analyze multiple species of corrosion products. The lower part of the two rightmost samples in Figure 3-3 highlights the machining marks from the manufacturing from the filter housings. The machining marks were present on the entirety of all filter housings, however not clearly seen on all images.

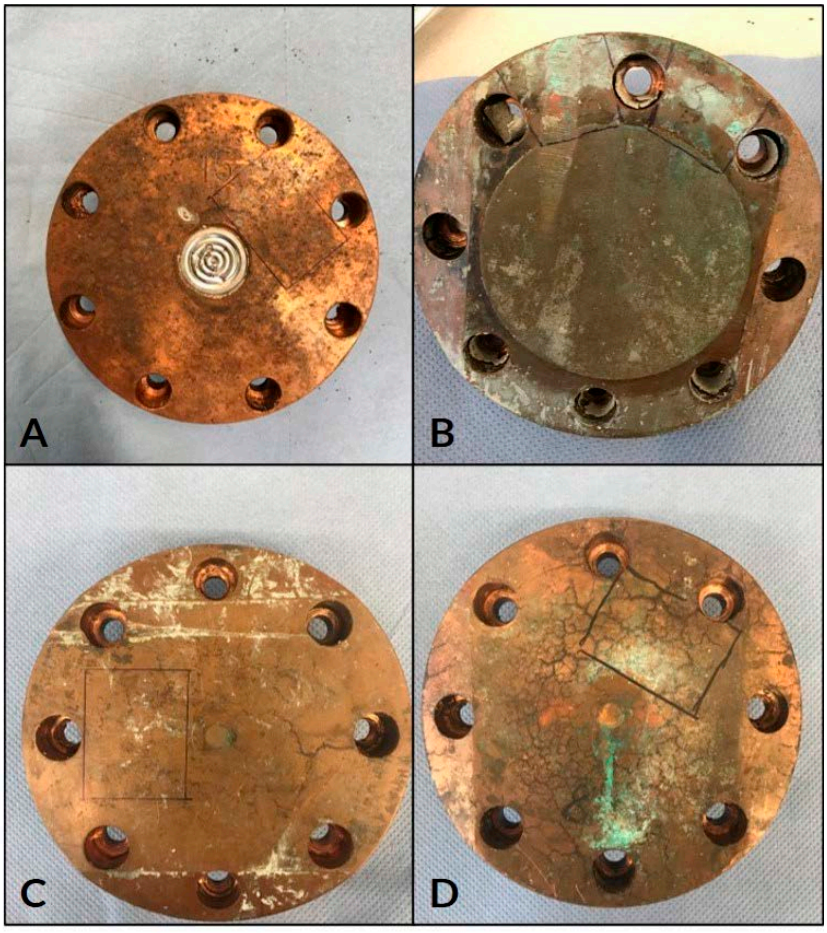

Figure 3-1. *The four filter housings that were analysed; A) PC901, B) MPFA1, C) LFA2 and D) UFA4 with sample areas marked by black rectangles.*

Figure 3-2. *Overview of filter housing PC901 and the area of which sample coupons for analysis were to be taken, marked on the filter housing with a black rectangle.*

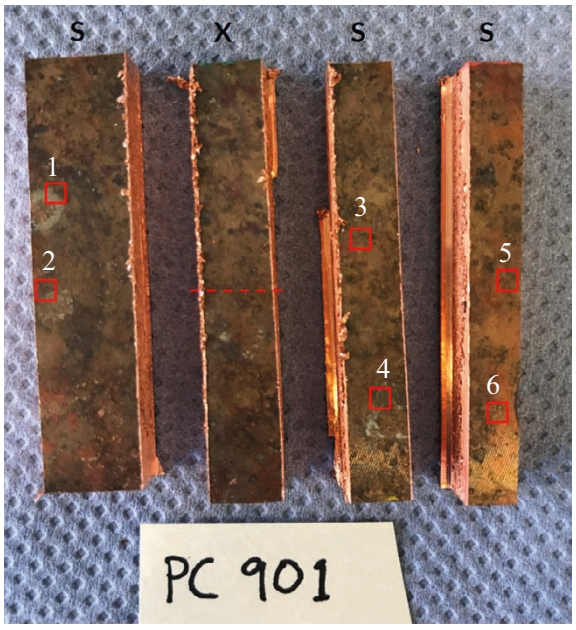

Figure 3-3. *The four test coupons taken from filter housing PC901. 'S' denotes coupons chosen for surface analysis and 'X' for cross section analysis. Machining marks (present on the entire surface) are clearly visible on the lower part of the two rightmost samples.*

3.2.1 Surface analysis

SEM/EDS

SEM/EDS analysis was carried out on the surface of the samples. Images showed clear machining marks from the manufacturing of the filter housings. Elemental analysis on the surface showed mainly copper and oxygen with remains of bentonite (Si- and Al-rich deposits on the surface) still adhering to the surface. In addition, small amounts of chlorine, iron, and sulfur was also observed for PC901 which can be seen in Figures 3-4–3-15 and corresponding tables. Light grey areas appear to be a visibly bare copper surface with a thin oxide layer and darker areas with bright white peaks to be bentonite. The white regions are caused by the charging effect of the non-conductive bentonite where a thicker layer becomes more charged. Although the level of sulfur was generally a few at% when analyzed over larger areas (as in Figures 3-10–3-15), there are a few observations of locally

higher levels using higher magnification. The observation of 5-8 at% sulfur and 6-7 at% calcium in Figure 3-6 indicate the presence of $CaSO_4$ from the bentonite clay. The detection of 9 at% sulfur, but only 2 at% calcium and 2 at% iron at a spot in Figure 3-7 could indicate the formation of copper sulfide. These observations are in line with the results from earlier field tests such as LOT (Johansson et al. 2020).

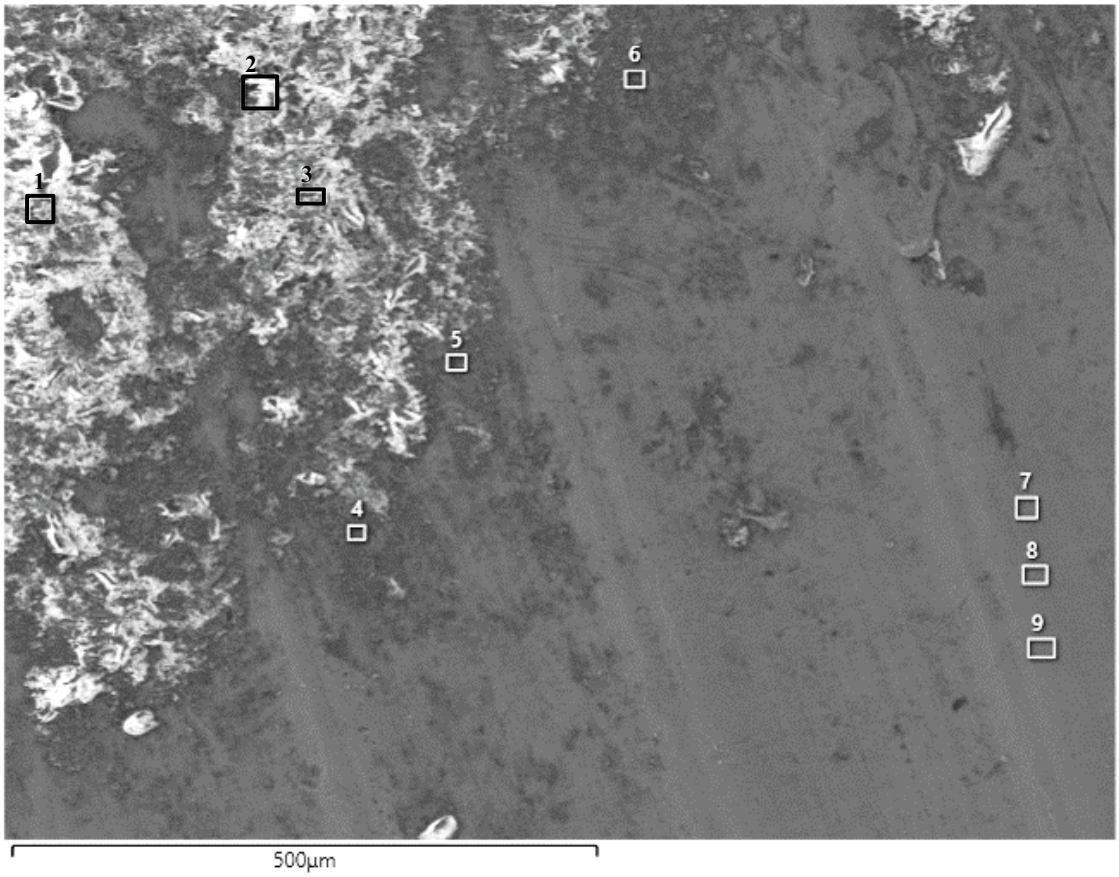

Element (At%)	1	2	3	4	5	6	7	8	9
N						13.33			
O	50.45	54.01	53.38	51.99	48.04	43.37	18.72	14.2	12.28
Na	2.97	1.96				1.94			
Mg	1.55	1.19	1.55	1.75	1.74	1.5			
Al	4.19	3.82	3.67	2.5	3.13	3.78			
Si	9.2	8.66	8.7	4.97	6.27	8.06	0.79		
S	1.14	1.24	1.54	1.08	0.96	0.81	0.65	0.48	
Cl	5.06	4.94	8.12	2.44	5.08	1.17	0.45		0.4
K	0.62	0.43	0.42	0.28	0.36	0.62			
Ca	2.75	2.39	2.07	6.1	1.97	1.87			
Ti	2.95	2.31	1.58	1.85	2.33	1.63			
Fe	5.66	6.3	3.56	5.22	3.78	3.9			
Cu	11.8	12.73	15.41	21.81	26.34	18.02	79.39	85.32	87.32
Zn	1.67								
Total	100	100	100	100	100	100	100	100	100

Figure 3-4. *SEM image of sample PC901 site 1. The EDS result of PC901 site 1 is shown in the table.*

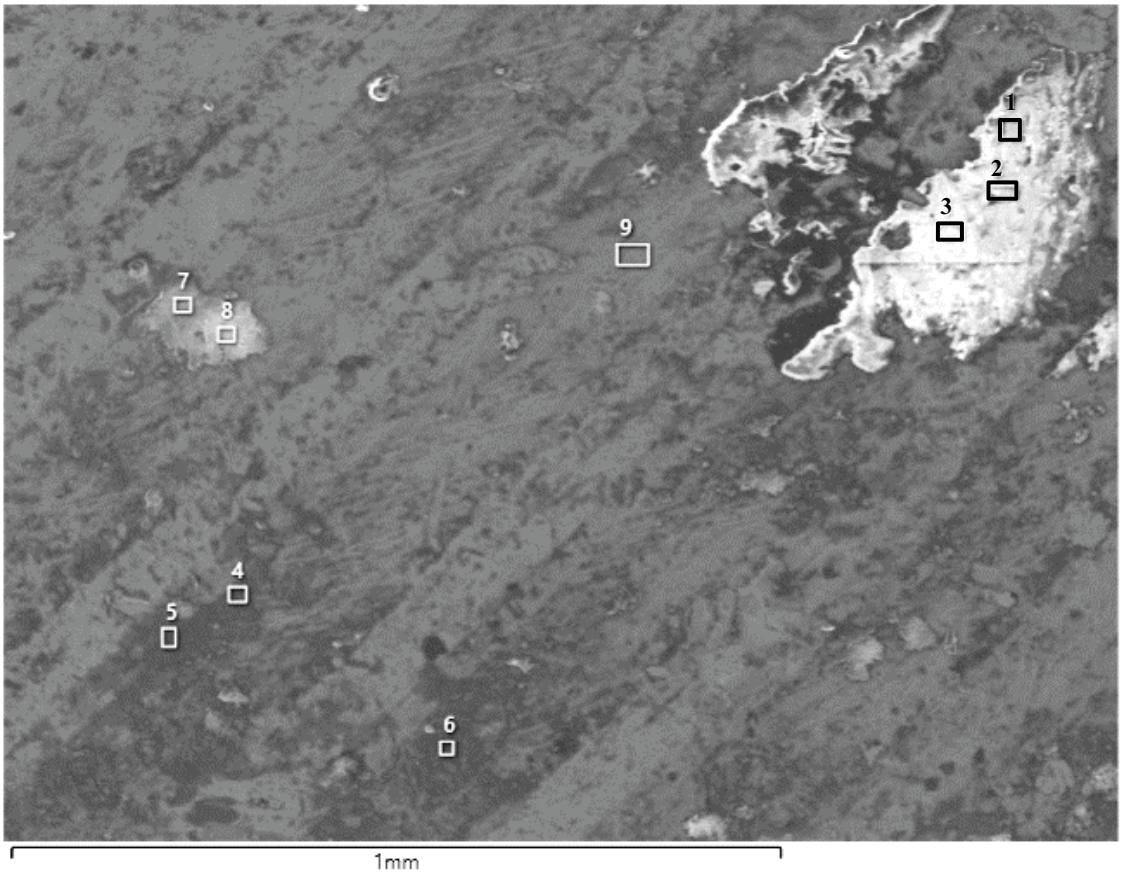

Element (At%)	1	2	3	4	5	6	7	8	9
O	75.81	58.72	75.55	51.3	52	56.62	57.76	53.35	22.78
Na		0.72	0.87	1.41		1.73	1.51		
Mg		0.46	0.6	1.57	1.87	2.73	1.97	1.24	
Al	2.48	0.8	2.14	5.75	4.63	3.27	4.72	3.52	0.76
Si	1.19	2.16	2.49	13.45	11.53	7.34	11.83	8.5	1.25
S	0.25	0.44	0.28	0.95	0.84	0.85	0.68	0.6	0.42
Cl	0.23		0.45	0.54	0.74	0.88	4.41	9.32	0.75
K				0.32	0.18	0.2			
Ca	0.45	0.43	0.86	3.71	6.17	9.46	3.64	0.34	0.61
Ti	0.55		0.44	1.14	0.58	2.17			0.61
Cr		8.68							
Fe	16.45	20.04	9.02	3.06	2.68	4.15	2.62	2.61	0.69
Cu	2.6	7.54	7.29	16.8	18.78	10.6	10.84	20.51	72.12
Total	100	100	100	100	100	100	100	100	100

Figure 3-5. *SEM image of PC901 site 2. The EDS result of PC901 site 2 is shown in the table.*

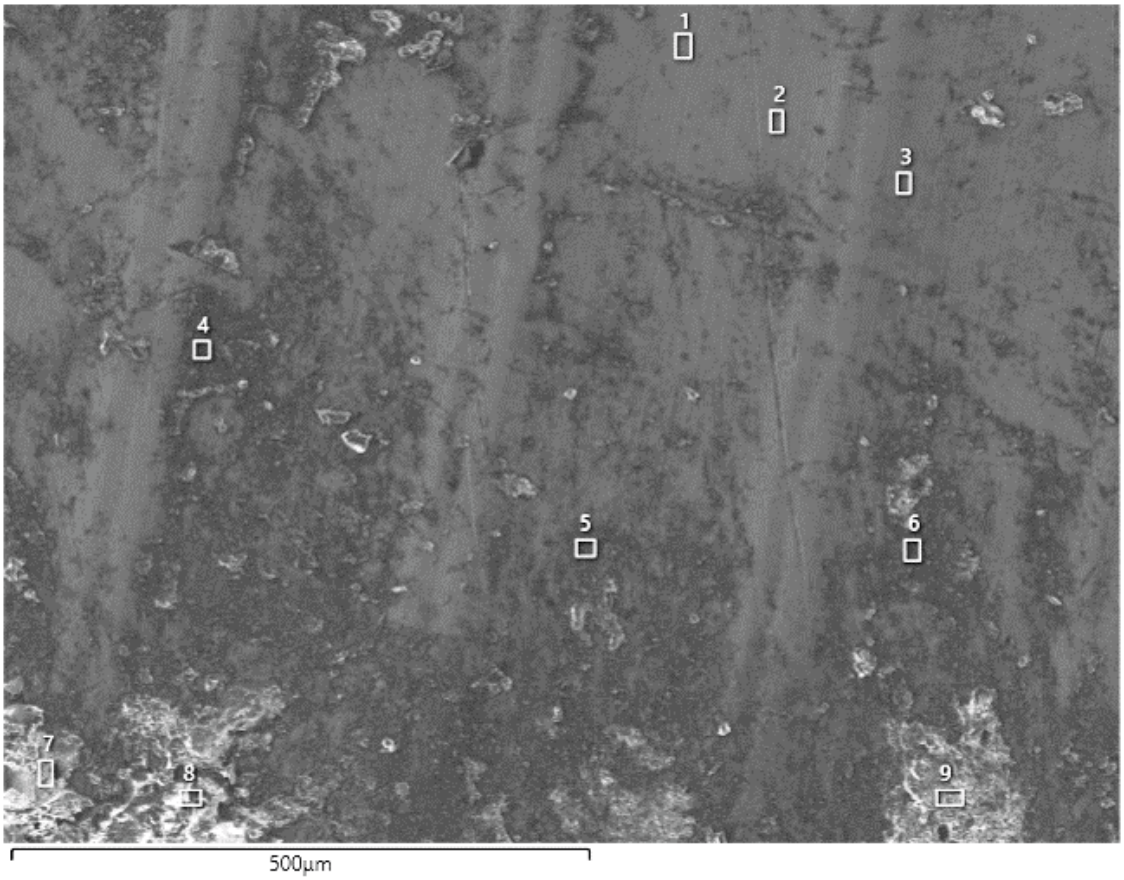

Element (At%)	1	2	3	4	5	6	7	8	9
N							12		
O	14.56	21.05	24.46	50.88	48.79	52.09	51.12	36.03	56.77
Na				2.46	7.33	2.19	2	22.2	10.59
Mg				0.81	0.89	1.23	0.65		0.83
Al				2.67	2.1	3.5	4.46	0.56	2.39
Si		0.89	0.85	3.58	3.76	7.28	3.48	1.1	5.32
P					0.25				
S	1.34	1.31	2.27	6.15	2.89	4.56	8.09	6.67	3.46
Cl			0.34	0.89	0.9	1.12	1.73	24.72	0.77
K				0.32	0.44	0.38	0.32	0.21	0.47
Ca	0.72	0.93	1.46	6.19	3.15	6.66	7.21	5.88	5.72
Ti		0.72		2.45	1.93	2.14	2.24	0.32	1.57
Fe				4.77	3.03	4.56	2.23		3.94
Cu	83.37	75.09	70.61	18.83	24.55	14.3	4.47	2.32	8.18
Total	100	100	100	100	100	100	100	100	100

Figure 3-6. *SEM image of PC901 site 3. The EDS result of PC901 site 3 is shown in the table.*

Element (At%)	1	2	3	4	5	6	7	8	9
N		15.45	13.59						
O	51.58	49.22	37.28	56.55	50.92	51.03	15.26	19.98	14.03
Na						1.12			
Mg	1.13			2.48	1.01	1.1			
Al	5.58	1.04	1.61	3.84	2.62	4.7			
Si	8.36	2.86	3.75	7.56	5.08	9.76			0.38
P	0.22					0.27			
S	3.41	0.55	9.17	1.23	1.64	4.72		0.45	0.31
Cl	0.41	0.13		0.37	0.36	0.55			
K	0.44		0.32	1.1	0.5	0.94			
Ca	3.08	7.87	2.21	8	7.28	4.87			
Ti	4.49	0.8	2.42	0.44	2.75	4.71			
Fe	5.92	2.05	2.12	2	2.44	6.16			
Cu	14.26	20.04	27.53	16.43	23.5	10.05	84.74	79.56	85.29
Zn	1.1				1.87				
Total	100	100	100	100	100	100	100	100	100

Figure 3-7. *SEM image of PC901 site 4. The EDS result of PC901 site 4 is shown in the table.*

Element (At%)	1	2	3	4	5	6	7	8	9
N	14.7								
O	59.41	61.9	64.86	59.37	64.31	47.76	13.63	12.23	12.14
Na	0.67	1.14	1.14	1.51					
Mg	1.24	1.87	1.55	1.72					
Al	3.42	5.84	6.99	7.06	2.91	1.9			
Si	7.78	18.81	19.8	19.08	6.15	4.1	0.53	0.48	0.44
S	0.7	2.68	0.32	2.11	2.39	2.28	0.51	0.4	0.65
Cl	0.16	0.37	0.12	0.18	0.4	0.43	0.45		
K		0.26	0.28	0.33	0.24				
Ca	8	2.82	2.5	2.64	13.55	2.91			
Ti	0.8	0.68		1.37	2.97	4.93			
Fe	0.73	0.98	0.43	1.54	1.53	1.5			
Cu	2.13	2.64	2	3.09	5.54	34.2	84.87	86.89	86.78
Zn	0.27								
Total	100	100	100	100	100	100	100	100	100

Figure 3-8. *SEM image of PC901 site 5. The EDS result of PC901 site 5 is shown in the table.*

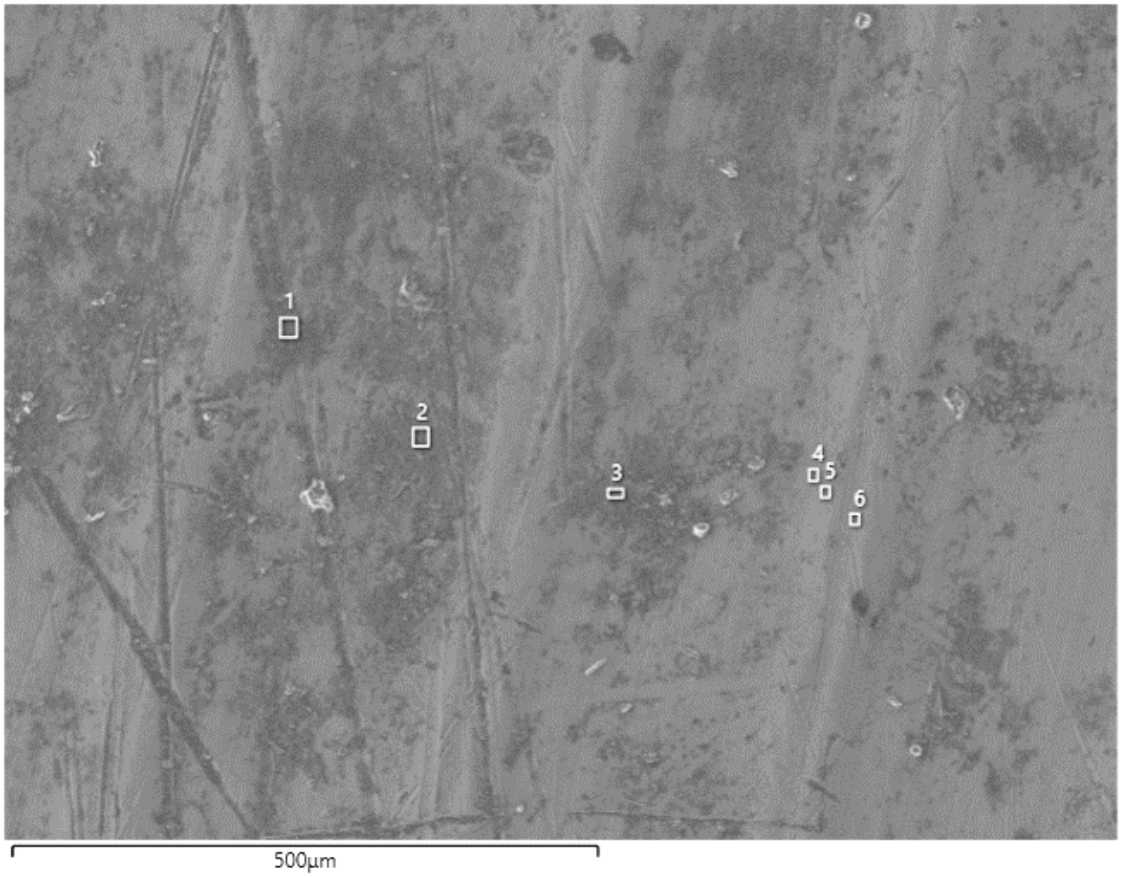

Element (At%)	1	2	3	4	5	6
N		13.57				
O	63.14	42.49	56.69	15.01	14.38	12.83
Na	0.89					
Mg	1.41	0.85	0.9			
Al	1.34	1.94	1.41			
Si	2.94	3.7	3.08	0.73	0.51	0.68
S	1.47	2.25	1.81	0.46	0.6	0.51
Cl	0.42	0.65	0.65	0.53	0.49	0.4
K	0.17	0.22				
Ca	16.12	7.02	13.57			
Sc	0.27					
Ti	0.87	0.78	0.3			
Fe	1.2	1.1	0.92			
Cu	9.76	25.43	20.68	83.27	84.02	85.58
Total	100	100	100	100	100	100

Figure 3-9. *SEM image of PC901 site 6. The EDS result of PC901 site 6 is shown in the table.*

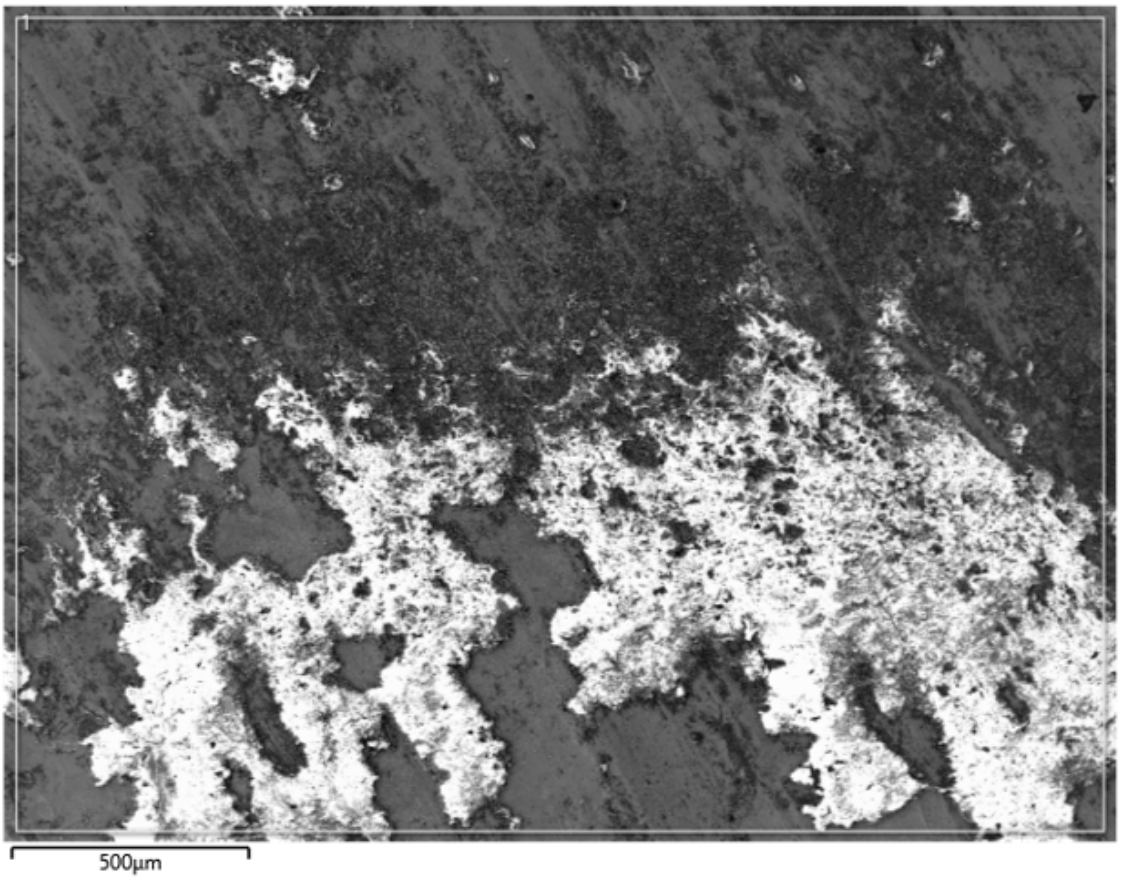

Element (At%)	1
O	50.05
Na	2.84
Al	3.39
Si	6.67
S	1.76
Cl	3.16
K	0.38
Ca	3.02
Ti	1.07
Fe	2.75
Cu	24.92
Total	100

Figure 3-10. *SEM image of PC901 site 1. The EDS result of PC901 site 1 is shown in the table. EDS over larger area.*

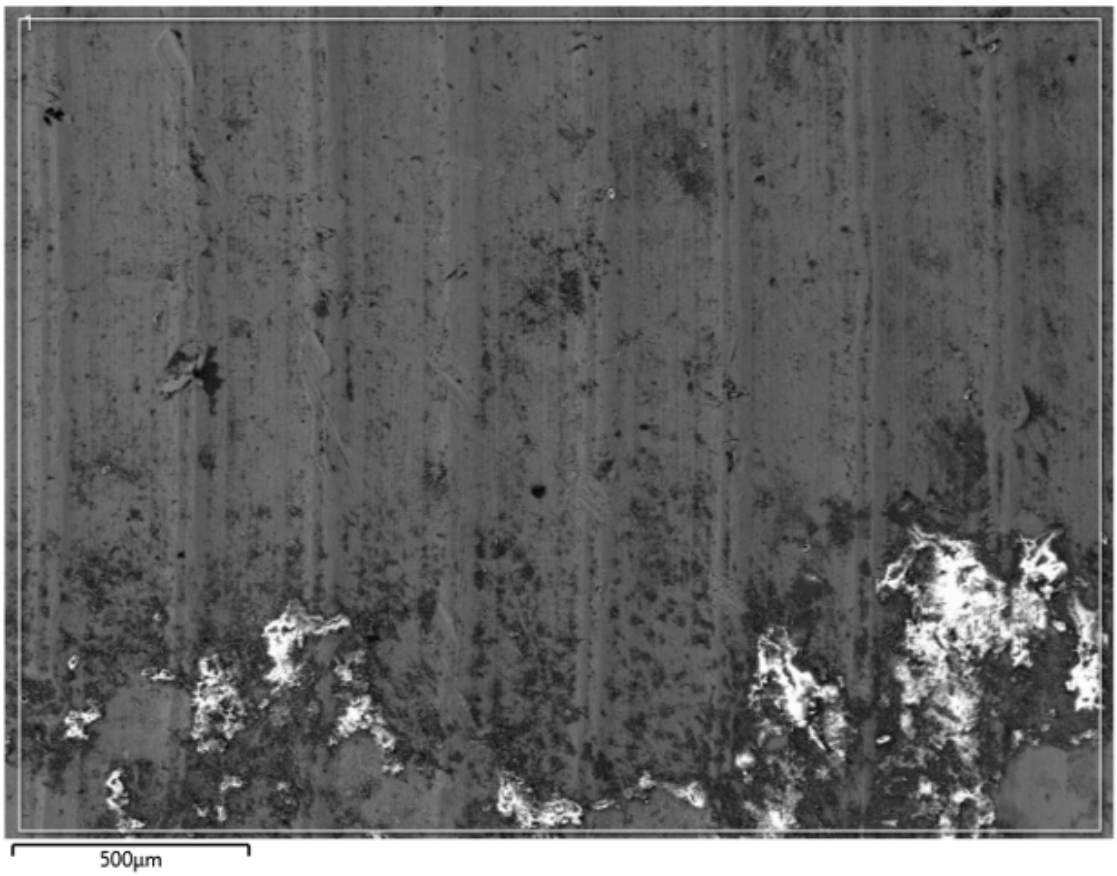

Element (At%)	1
O	31.7
Na	3.85
Al	1.4
Si	2.54
S	1.52
Cl	1.59
K	0.3
Ca	1.72
Ti	0.55
Fe	1.25
Cu	53.59
Total	100

Figure 3-11. *SEM image of PC901 site 2. The EDS result of PC901 site 2 is shown in the table. EDS over larger area.*

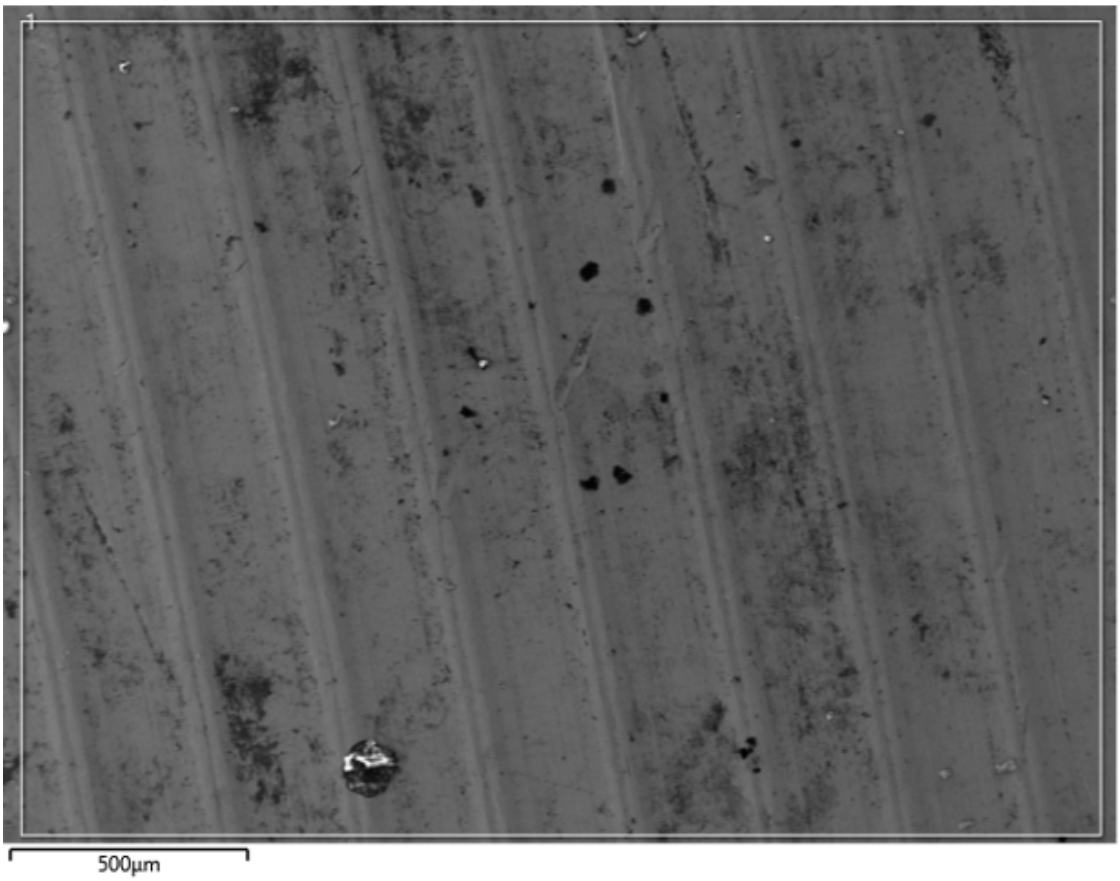

Element (At%)	1
O	21.93
Si	1.05
S	0.72
Cl	0.27
Ca	0.59
Ti	0.36
Fe	0.74
Cu	74.35
Total	100

Figure 3-12. *SEM image of PC901 site 3. The EDS result of PC901 site 3 is shown in the table. EDS over larger area.*

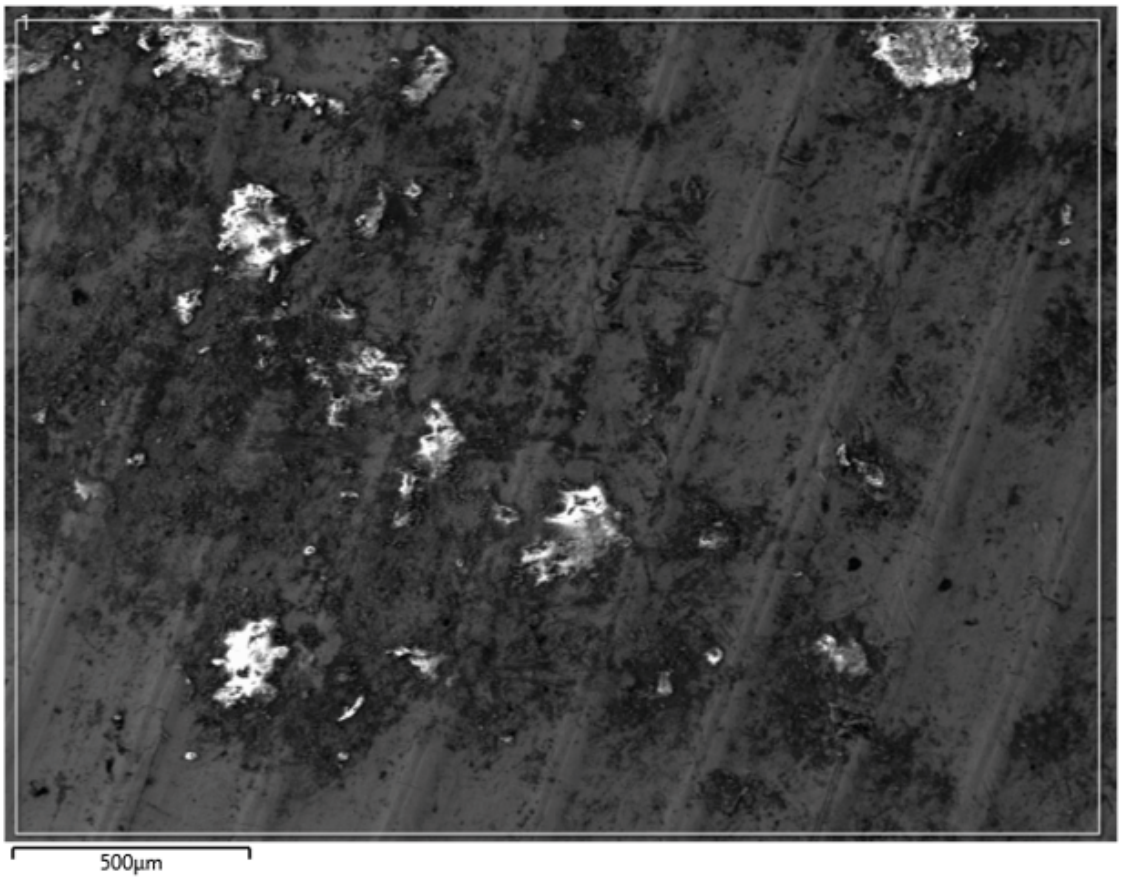

Element (At%)	1
O	39.21
Na	4.02
Mg	1.11
Al	2.21
Si	3.86
S	1.56
Cl	2.34
K	0.22
Ca	3.14
Ti	0.69
Fe	1.74
Cu	39.89
Total	100

Figure 3-13. *SEM image of PC901 site 4. The EDS result of PC901 site 4 is shown in the table. EDS over larger area.*

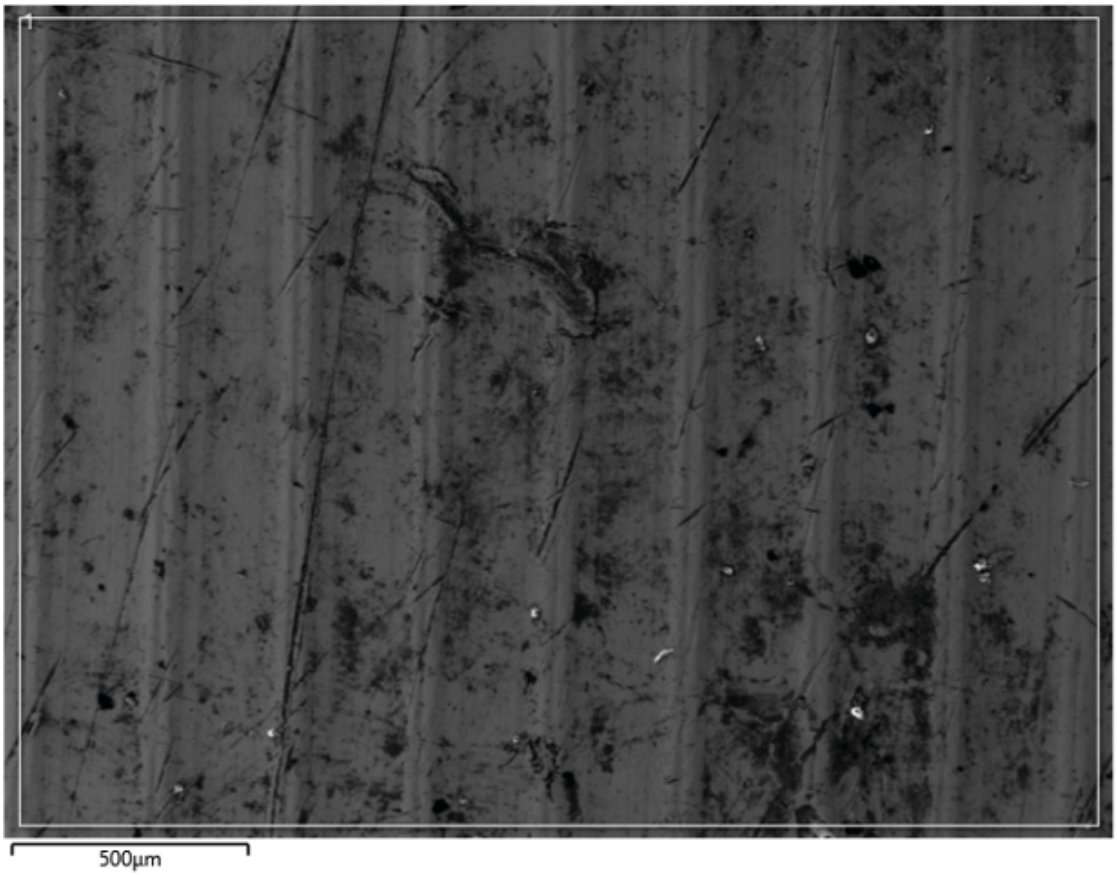

Element (At%)	1
O	24.11
Al	0.98
Si	1.57
S	1.51
Cl	0.36
Ca	1.62
Ti	0.31
Fe	0.65
Cu	68.89
Total	100

Figure 3-14. *SEM image of PC901 site 5. The EDS result of PC901 site 5 is shown in the table. EDS over larger area.*

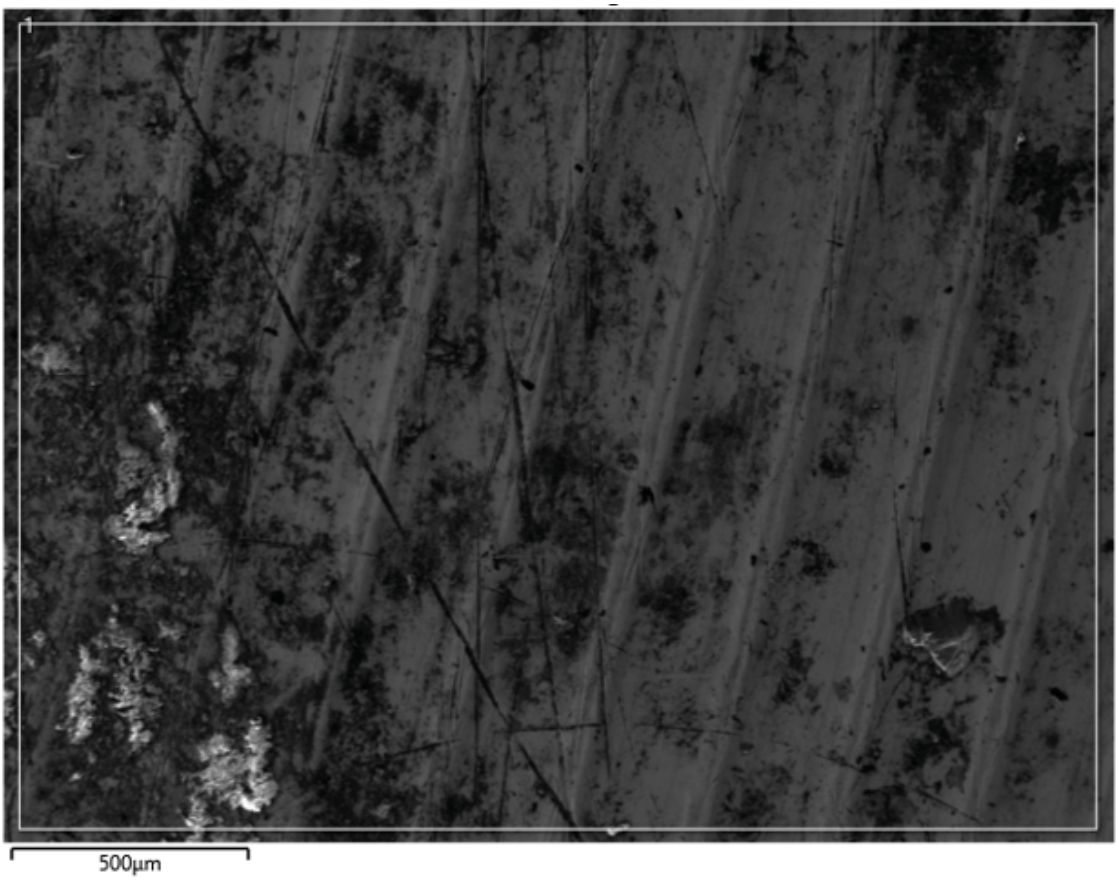

Element (At%)	1
N	11.85
O	26.1
Al	1.36
Si	2.22
S	2.28
Cl	0.91
K	0.18
Ca	2.45
Ti	0.53
Fe	0.82
Cu	51.31
Total	100

Figure 3-15. *SEM image of PC901 site 6. The EDS result of PC901 site 6 is shown in the table. EDS over larger area.*

XRD

Corrosion products were analyzed by XRD on the sample coupon surfaces. Apart from metallic copper, small peaks of cuprite were observed at 36.5 2θ, which can be seen in Figure 3-16. MgO was detected at angle 62 2θ for bentonite which was added to see the contribution of bentonite on the copper samples. No clear peaks of MgO was observed for PC901 or any of the other filter housing samples. Several "satellite peaks" can be seen around the main copper peaks, similar to the findings in previous studies from field tests (Johansson et al. 2020). The unidentified "satellite peaks" were located at 39, 41.5, 45.5 and 48.5 2θ and were observed on all samples. A Ni-filter was used to remove Cu Kβ X-rays along with other high energy background radiation, see red graph in Figure 3-17. After removing Kβ X-rays and other background radiation only cuprite and metallic copper peaks could be seen. However, the Cu Kβ X-rays were only seen at 39 and 45.5 2θ leaving the peaks at 41.5 and 48.5 2θ unidentified. Aged X-ray tubes with tungsten filaments deposit W on the inside glass envelope. This produces W Lα peaks and it could be found that it coincides with the peaks at 41.5 and 48.5 which is also filtered out by the Ni-filter.

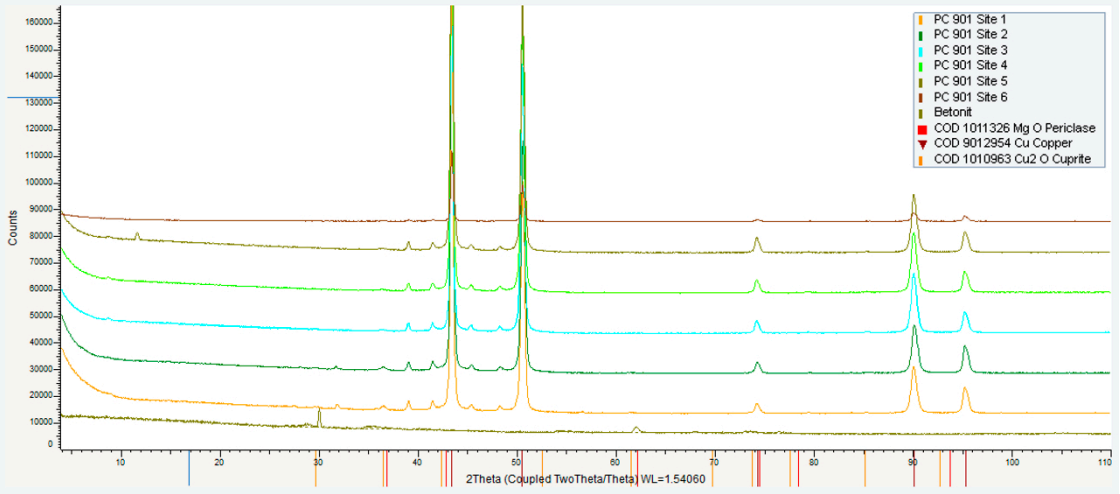

Figure 3-16. *XRD diffractograms obtained from the surface of PC901.*

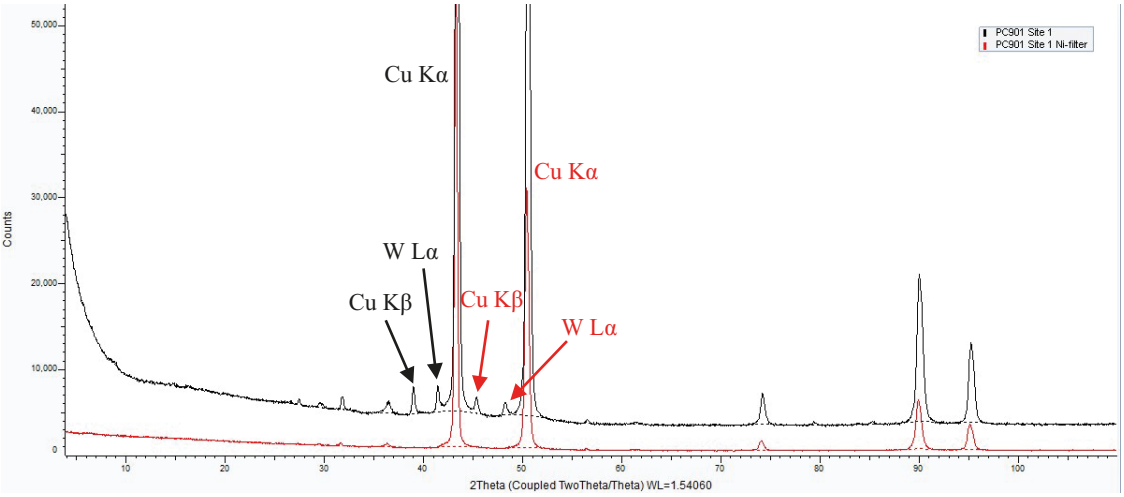

Figure 3-17. *XRD diffractogram of PC901 site 1 (black) and the same diffractogram where a Ni-filter was used to filter away Cu Kβ and W Lα peaks (red).*

FTIR/IRRAS

FTIR/IRRAS-measurement were performed on the samples sites. On a microscopic level, the areas were relatively varied but largely consisted of a combination of dark and bright (black and white, respectively) surfaces. In some areas, metal shine and reddish hues were observed. When possible, each separate colour of surface was subjected to a distinct measurement.

Although there might be multiple types of compounds resulting in brighter (e.g. clay and oxide) and darker (e.g. oils and malachite – $Cu_2(CO_3)(OH)_2$) areas, the focus and colour reproduction of the microscope was not sufficient to categorize the constituents further with any great deal of accuracy.

IRRAS measurements were made on the PC901 coupons and their corresponding IR-spectra can be seen in Figure 3-18. A characteristic cuprite peak around 630 cm^{-1} can be seen for most measured areas, indicating the presence of the corrosion product. The double peak around 1 300–1 600 cm^{-1} are slightly visible and could indicate malachite. The peaks at 1 000 cm^{-1} and 3 600 cm^{-1}, and the double peak at 500–600 cm^{-1} indicate bentonite. In addition, site 5 and the area with red appearance, shows a sulfate peak around 1 150 cm^{-1}.

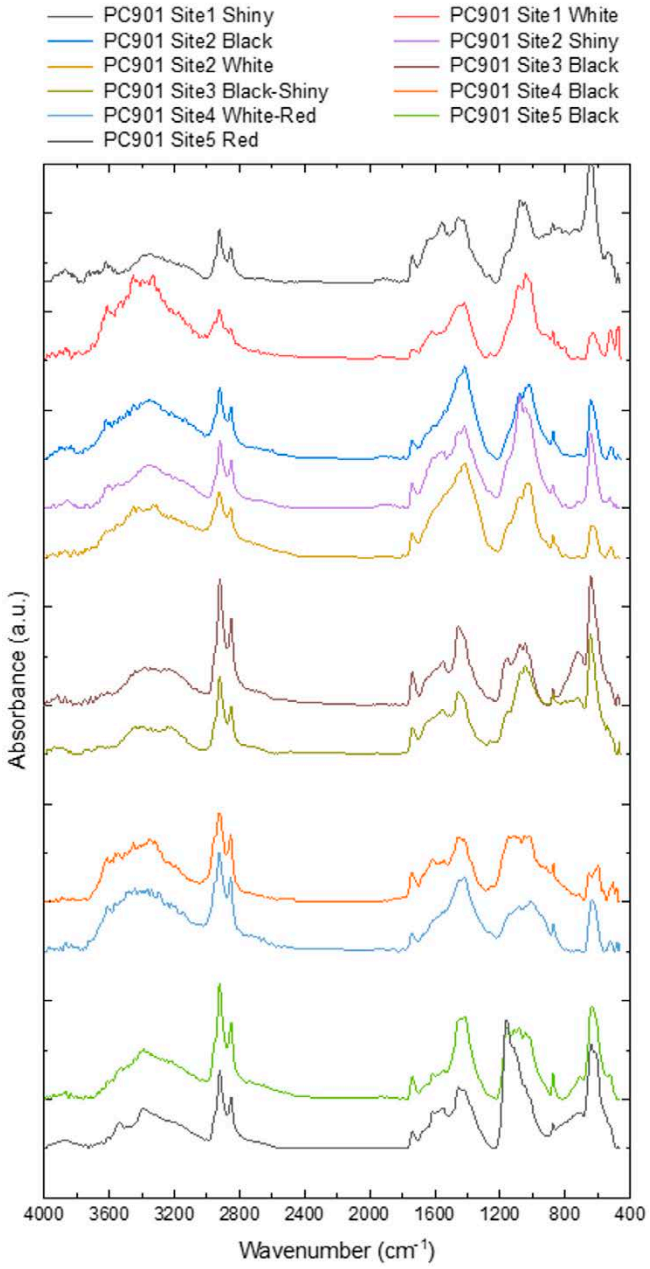

Figure 3-18. *Infrared spectra from FTIR/IRRAS measurement on surface of sample PC901.*

3.2.2 Cross section analysis

SEM/EDS

The cross section samples were cut in half, cast into epoxy resin while mounted surface-to-surface (in order to try and protect the surface oxides during sample preparation), grinded or polished, and analysed with SEM/EDS. In Figures 3-19–3-20 and corresponding tables, the cross section of PC901 are presented after dry grinding. Subsequently, in Figures 3-21–3-27 and corresponding tables, the cross section of PC901 are presented after diamond polishing. The cross section images showed that the surfaces were generally observed to be smooth, with some minor features, possibly resulting from the manufacturing process (machining), but no clear sign of localised corrosion. In Figure 3-22 two surfaces can be seen mounted against each other, which is indicated with a red dashed line. The oxide layer was observed to be in the range of 1–2 µm in thickness. The EDS results show signs of sulfur being present (Figure 3-19).

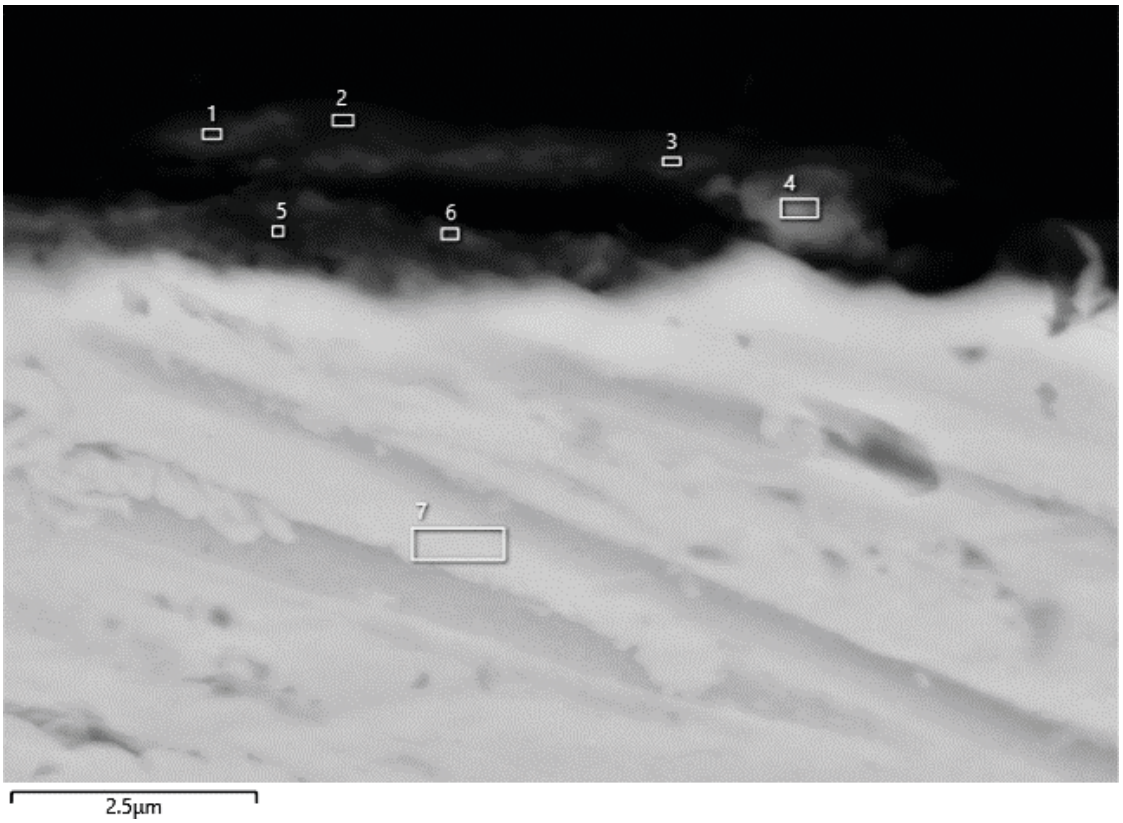

Element (At%)	1	2	3	4	5	6	7
O	25.38	34.21	15.17	15.29	36.47	25.51	
Mg	1.56	1.94					
Al	4.69	8.21	3.53	1.96	2.86	3.13	
Si	12.25	19.56	7.48	4.5	7.56	7.38	
S	3.38	2.75	9.23	12.24	4.21	7.45	
Cl	0.38	0.29	0.25		0.16	0.19	
K	0.17	0.22	0.16	0.18	0.12	0.1	
Ca	5.15	6.09	2.17	2.68	12.79	5.34	0.11
Ti		0.08	0.15	0.21			
Cr						0.11	
Fe	0.66	1.44	0.56	0.35	0.5	0.52	
Cu	46.38	25.19	61.29	62.58	35.32	50.27	99.89
Total	100	100	100	100	100	100	100

Figure 3-19. *SEM image of the cross section of PC901. The EDS result of the cross section of PC901 is shown in the table.*

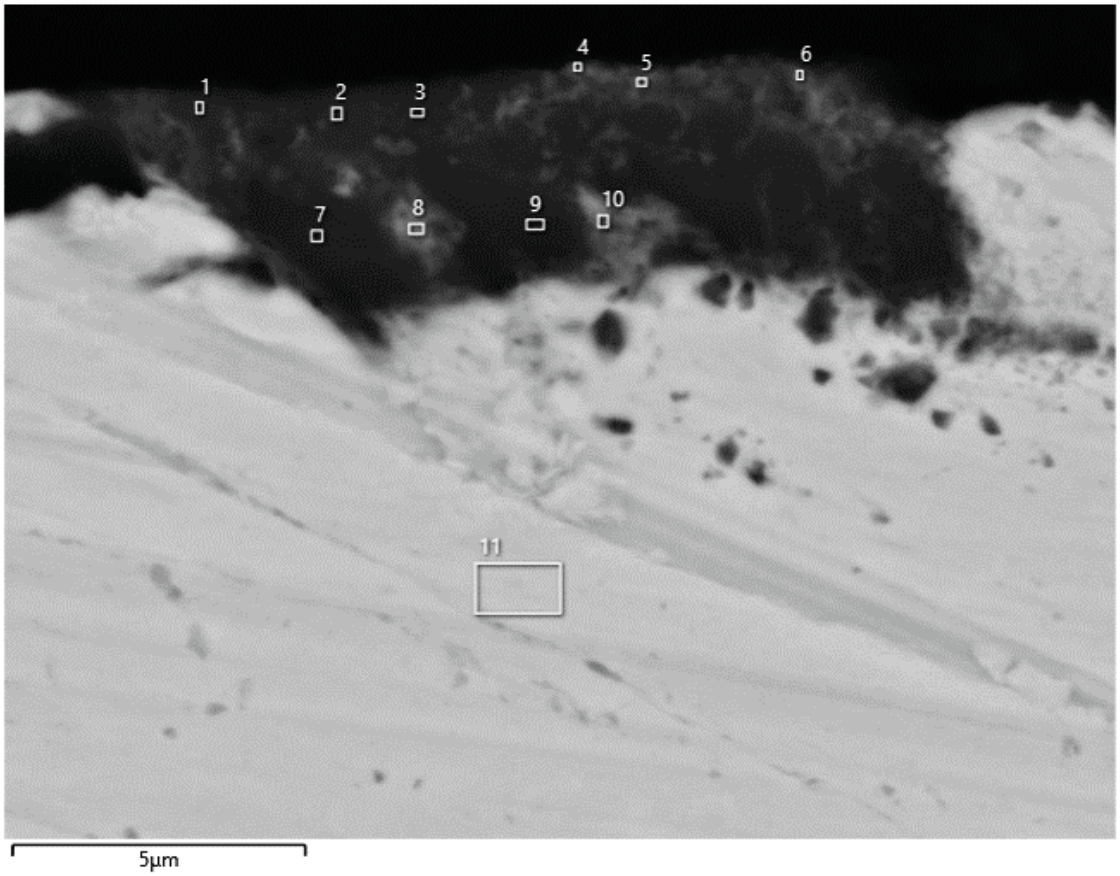

Element (At%)	1	2	3	4	5	6	7	8	9	10	11
O	8.48	8.21	8.42	10.38	8.93	8.61	1.84	3.08	2.14	3.63	
Al	0.41	0.21			0.41	0.34					
Si	77.33	82.5	82	40.22	55.27	51.62	91.63	63.08	92.01	60.2	0.09
S	0.15		0.12	0.12	0.08	0.12					
Cl						0.07					
K	0.09										
Ca	0.2	0.18		3.61	0.39	0.36				0.12	
Ti	0.16	1.1	0.76								
Fe				0.19	0.14	0.14					
Cu	13.18	7.79	8.69	44.69	34.78	38.74	6.53	33.84	5.86	36.04	99.91
Br				0.78							
Total	100	100	100	100	100	100	100	100	100	100	100

Figure 3-20. *SEM image of the cross section of PC901, depicting a surface defect with a SiC particle from the polishing. The EDS result of the cross section of PC901 is shown in the table.*

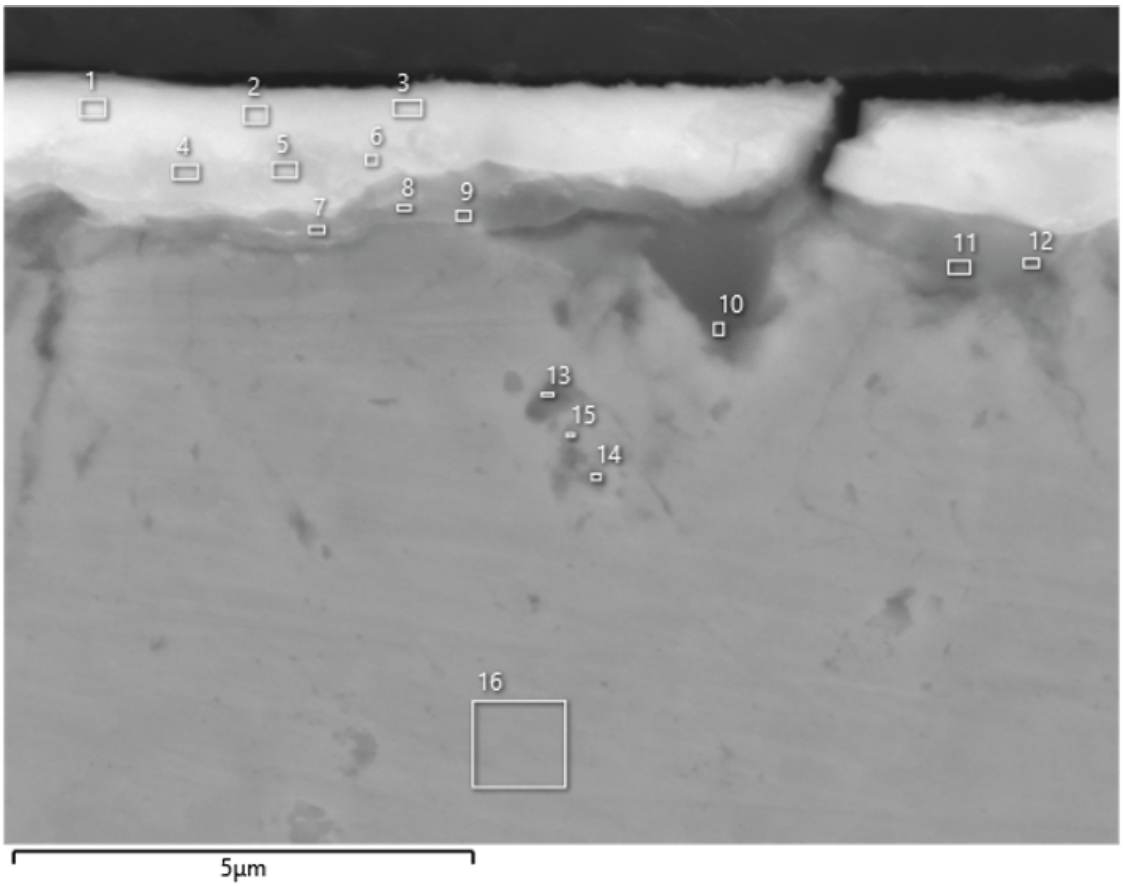

Element (At%)	1	2	3	4	5	6	7	8	9	10	11	12	13	14	15	16
O	70.56	70.58	71.56	54.83	55.27	56.76	27.83	34.4	31.67	4.58	17.31	21.4	2.01	2.53	4.31	
Na				5.61	7.2	7.07	4.14	4.74	3.69			2.92				
Mg	1.34	1.4	1.34	1.07	0.96	1.01	0.6	0.56	0.59							
Al	1.05	1.11	0.87	0.46	0.65	0.53	0.23	0.28	0.31							
Si	0.99	1.01	1.07	0.6	0.71	0.8	0.54	0.4	0.69	44.12	0.3	0.49	22.26	18.07	9.11	
S	1.97	2.19	2.15	2.29	2.62	2.61	1.32	1.55	1.34		0.71	1.03				
Cl	0.38	0.44	0.34	0.66	0.67	0.51	0.92	0.74	0.6		0.33	0.63				
K	0.27	0.29	0.3	0.27	0.29	0.32		0.21	0.17			0.14				
Ca	0.94	0.89	0.89	1.02	0.94	0.95	0.55	0.52	0.52		0.44	0.62				
Ti	0.07	0.09	0.13			0.12										
Fe	0.08	0.08	0.08		0.1	0.07										
Cu	22.35	21.91	21.25	33.18	30.6	29.26	63.87	56.6	60.41	51.3	80.9	72.77	75.73	79.4	86.59	100
Total	100	100	100	100	100	100	100	100	100	100	100	100	100	100	100	100

Figure 3-21. *SEM image of the cross section of PC901, diamond polished. A crack in the thin oxide layer is depicted. The EDS result of the cross section of PC901, diamond polished, is shown in the table.*

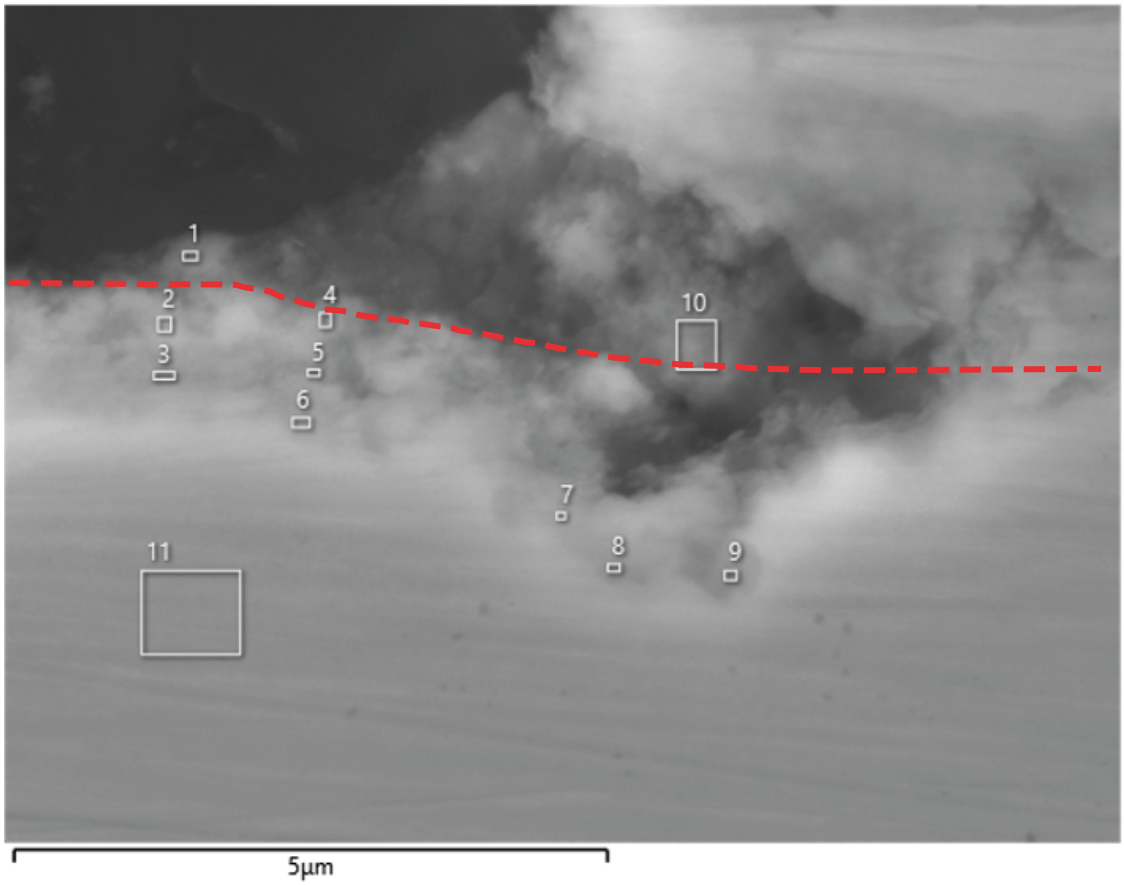

Element (At%)	1	2	3	4	5	6	7	8	9	10	11
O	48.55	44.15	37.25	48.82	40.92	29.91	35.33	31.44	29.79	40.23	
Mg	0.97	0.69		0.96	0.74						
Al	1.32	0.77	0.49	1.08	0.45	0.29	0.35		0.31	0.83	
Si	2.03	1.15	0.77	1.24	0.88	0.52	0.69	0.46	0.66	1.37	
S	0.83	0.71	0.71	0.7	0.75	0.38	0.65	0.39	0.44	1.02	
Cl	0.5	0.63	0.5	0.52	0.45	0.51	0.79	0.76	0.68	0.63	
K										0.15	
Ca	2.92	1.39	0.9	3.95	1.99	0.69	0.64	0.53	0.98	2.57	
Ti	0.5	0.29	0.15	0.43	0.2		0.14	0.15	0.22	0.93	
Fe	0.49	0.33	0.12	0.28	0.12		0.2		0.18	1.08	
Cu	41.89	49.89	59.1	42.03	53.5	67.7	61.22	66.28	66.73	51.18	100
Total	100	100	100	100	100	100	100	100	100	100	100

Figure 3-22. *SEM image of the cross section of PC901, diamond polished. A dashed red line indicates approximately where two surface-to-surface mounted samples meet. Closest to the dashed line is the exposed surface of the sample with corresponding oxide layer and clay particles. The EDS result of the cross section of PC901, diamond polished, is shown in the table.*

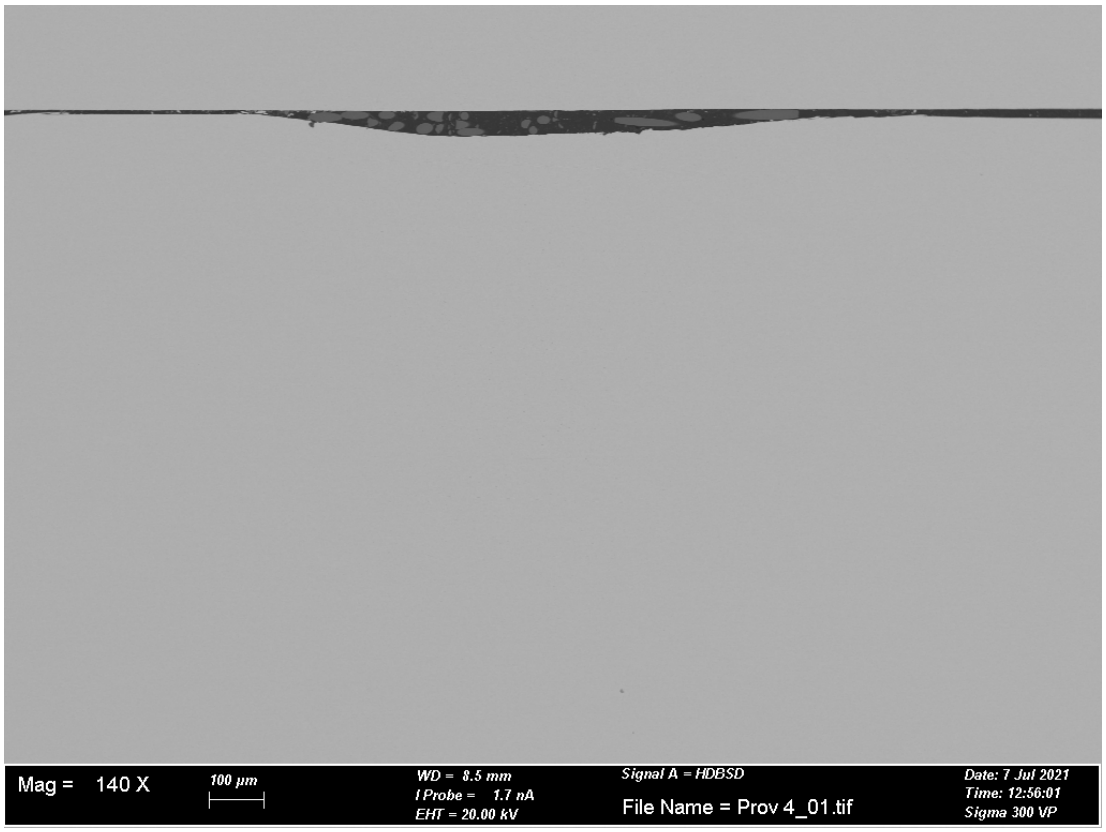

Figure 3-23. *SEM image overview of cross section mounted in epoxy resin surface to surface at ×140 magnification, PC901.*

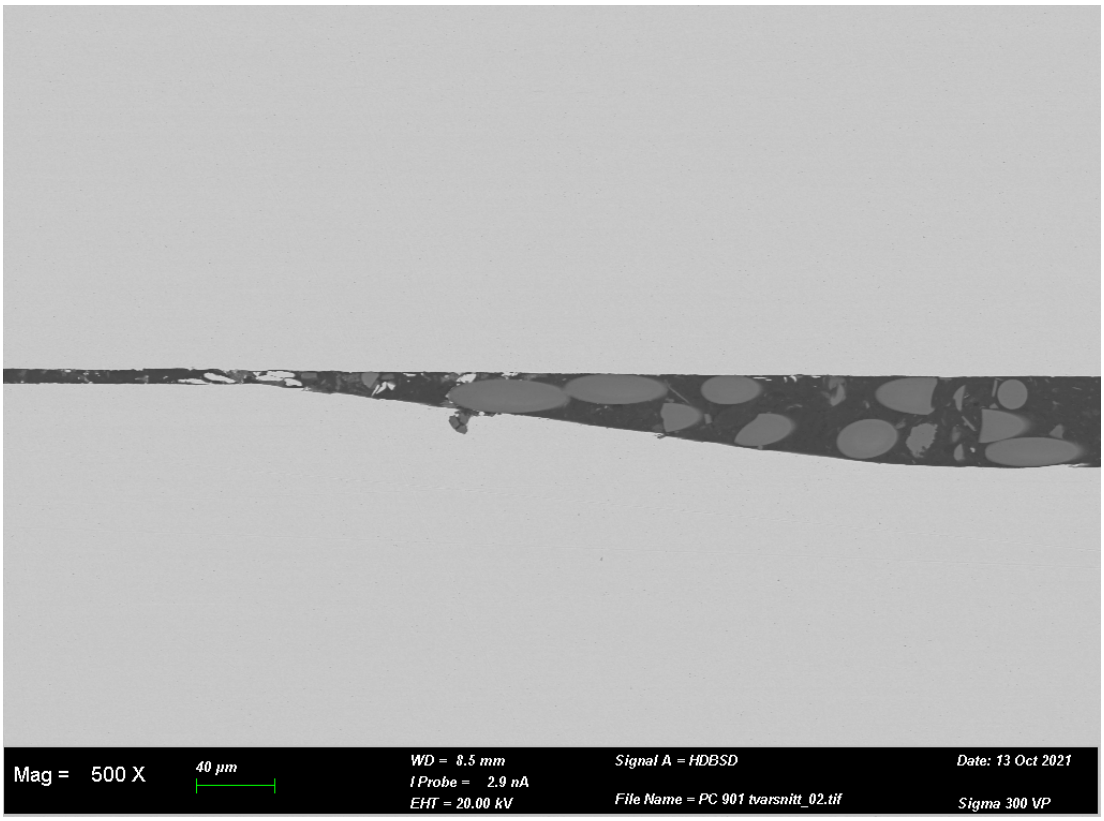

Figure 3-24. *SEM image overview of cross section mounted in epoxy resin surface to surface at ×500 magnification, PC901.*

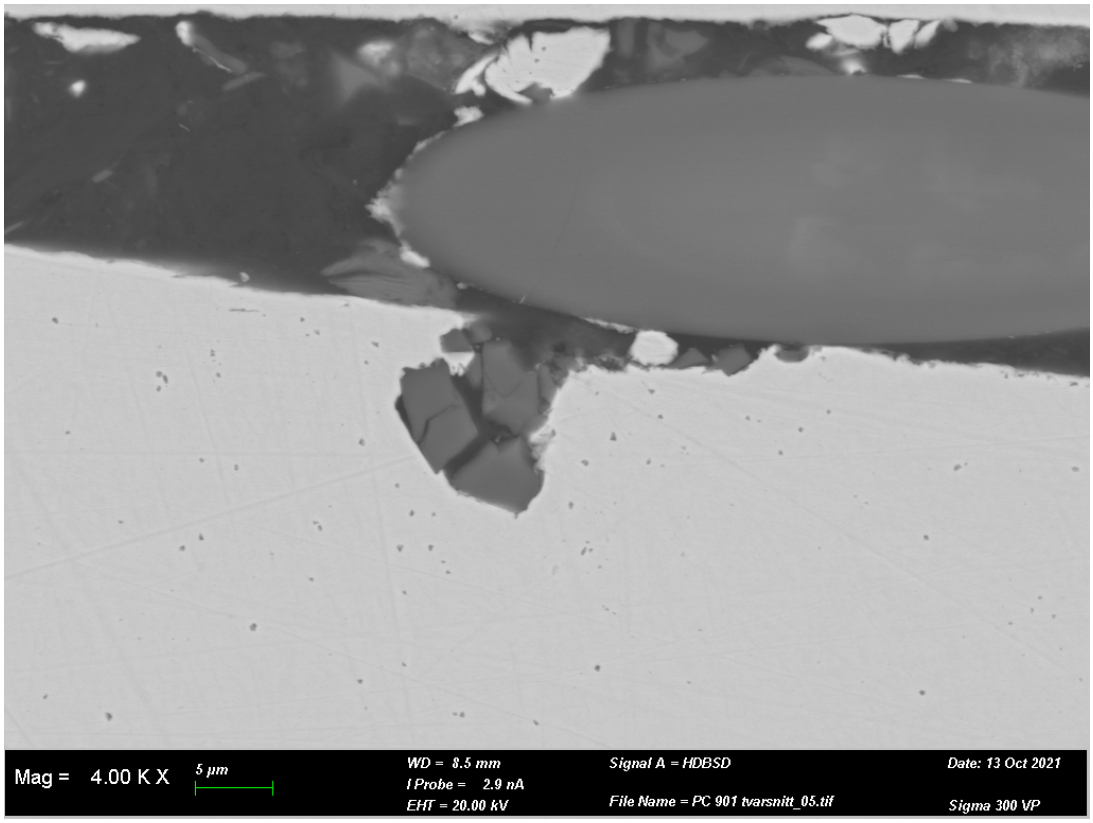

Figure 3-25. *SEM image overview of cross section mounted in epoxy resin surface to surface at ×4 000 magnification, PC901. The cavity formed shape in the image is likely consisting of particles from the sample preparation. It cannot be said for certain if the cavity was formed due to corrosion or sample preparation or if it is a cavity at all.*

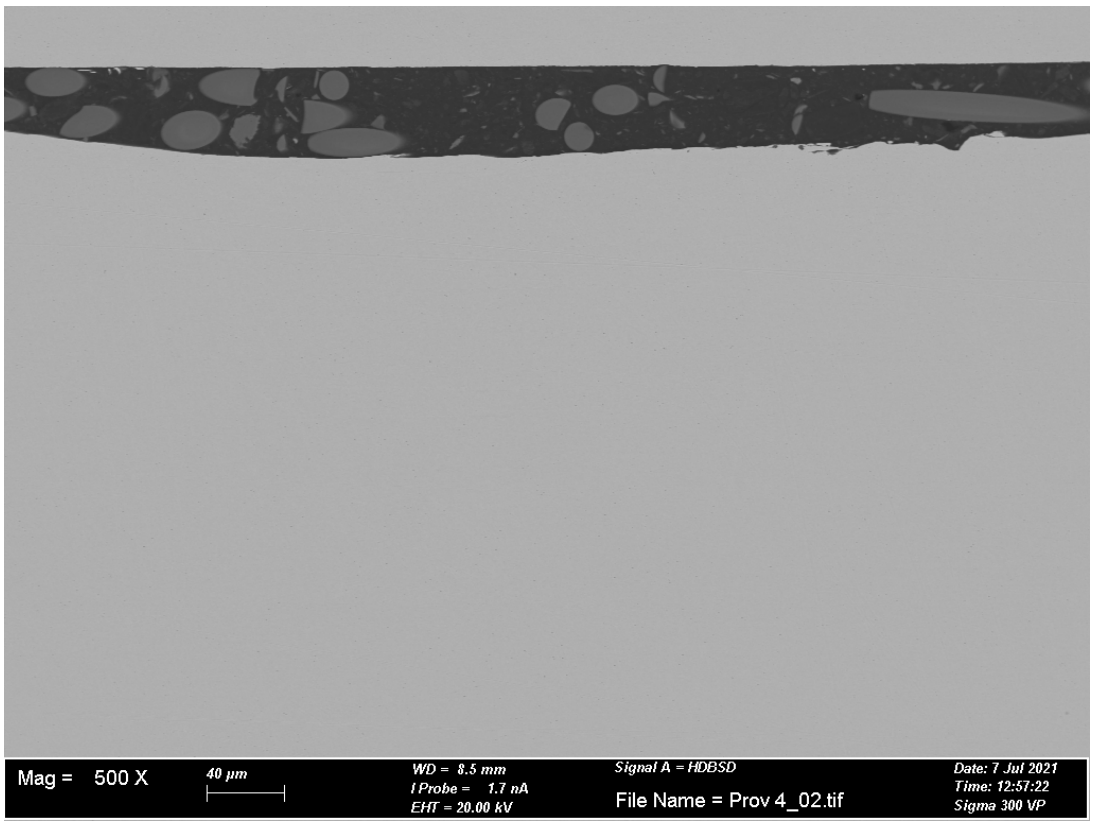

Figure 3-26. *SEM image overview of cross section mounted in epoxy resin surface to surface at ×500 magnification, PC901.*

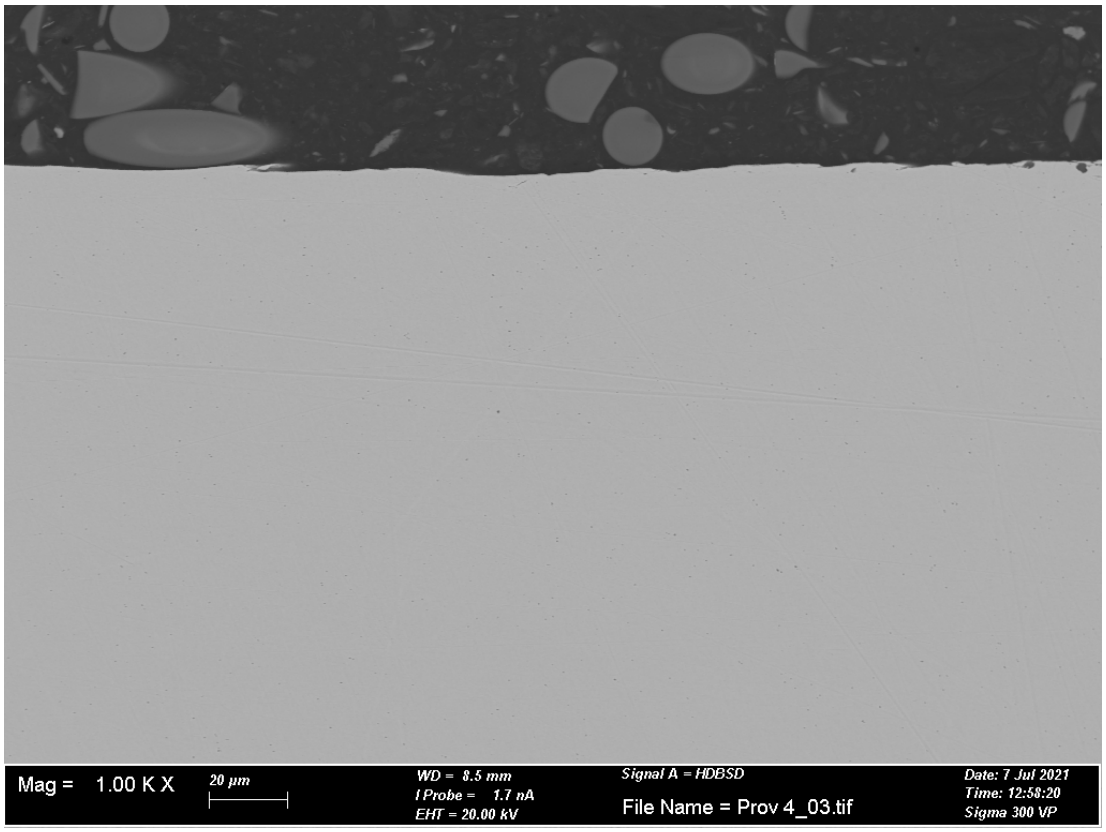

Figure 3-27. *SEM image overview of cross section at ×1 000 magnification, PC901.*

3.3 MPFA1

Figure 3-28 shows an overview of filter housing MPFA1, with its designated areas for sample coupons indicated by two black rectangles. Sample preparation was carried out in a similar way as for PC901, with dry cutting and epoxy resin casting for cross section sample. However, due to a variation in filter housing design compared to PC901, the sample coupons for MPFA1 were cut from two separate areas of the filter housing surface. An overview of the four sample coupons for filter housing MPFA1 can be seen in Figures 3-29–3-30 along with their designated surface analysis sites, marked with red rectangles.

Figure 3-28. *Overview of filter housing MPFA1 and the areas of which sample coupons for analysis were taken, indicated with two black rectangles.*

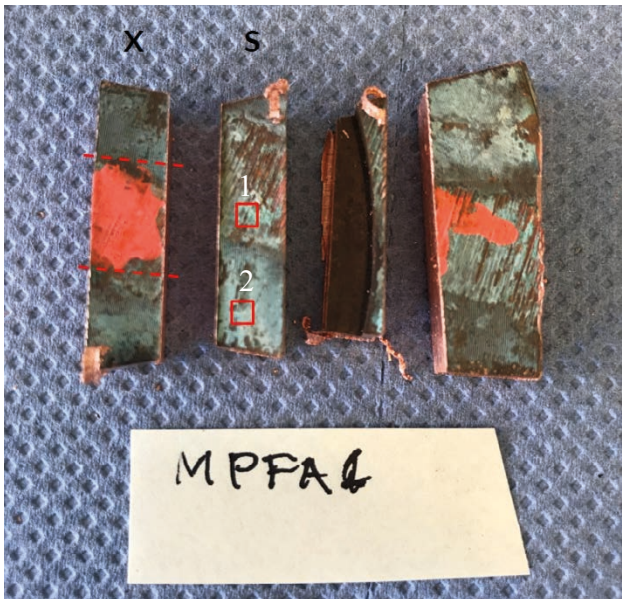

Figure 3-29. *Two out of four test coupons taken from filter housing MPFA1. 'S' denotes coupons chosen for surface analysis and 'X' for cross section analysis (the orange/red markings are ink used during the sample preparation and were not included in the analyses).*

Figure 3-30. *Two out of four test coupons taken from filter housing MPFA1. 'S' denotes coupons chosen for surface analysis.*

3.3.1 Surface analysis

SEM/EDS

SEM/EDS analysis was carried out on the surface sample sites. Images show clear machining marks from manufacturing of the filter housings. Elemental analysis on the surface show mainly copper and oxygen with clustered bentonite or bentonite located inside the machining grooves. Small amounts of chlorine, iron, and sulfur were also observed for MPFA1 which can be seen in Figures 3-31–3-41 and corresponding tables. Light grey areas appear visibly as a bare copper surface with a thin oxide layer and darker areas to be bentonite and corrosion products. The level of sulfur was generally lower than 1 at% when analyzed over larger areas (as in Figures 3-37–3-41), and even observations using higher magnification showed at most a few at% sulfur (Figures 3-31–3-36).

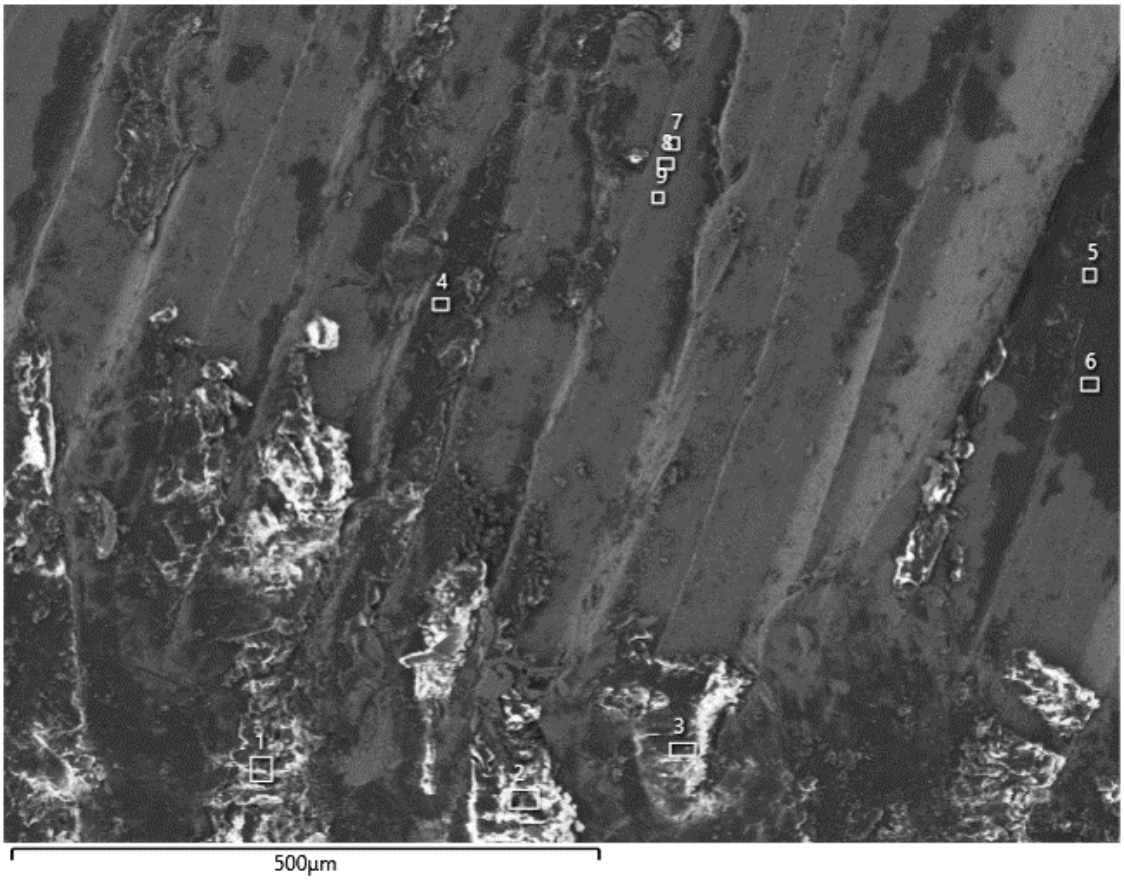

Element (At%)	1	2	3	4	5	6	7	8	9
O	62.38	62.51	62.87	63.53	63.24	63.46	23.71	22.76	23.84
Na	4	2.53	2.92	3.03	2.94	2.48			
Mg	1.48	1.37	1.46	1.41	1.79	1.74			
Al	7.13	7.19	7.09	8.22	7.71	4.97			
Si	17.16	18.72	16.53	20.19	17.95	11.63	0.55	0.41	0.51
S	0.57	0.46	0.54	0.46	0.58	0.57	0.28	0.25	
Cl	0.58	1.03	1.53	0.11	0.2	0.41	1.01	0.86	0.83
K	0.1	0.12	0.13	0.3					
Ca	0.91	1.33	0.25	0.28	1.4	5.41			
Fe	0.97	0.93	0.43	0.7	0.96	0.74			
Cu	4.72	3.81	6.26	1.77	3.24	8.58	74.45	75.73	74.83
Total	100	100	100	100	100	100	100	100	100

Figure 3-31. *SEM image of MPFA1 site 1. The EDS result of MPFA1 site 1 is shown in the table.*

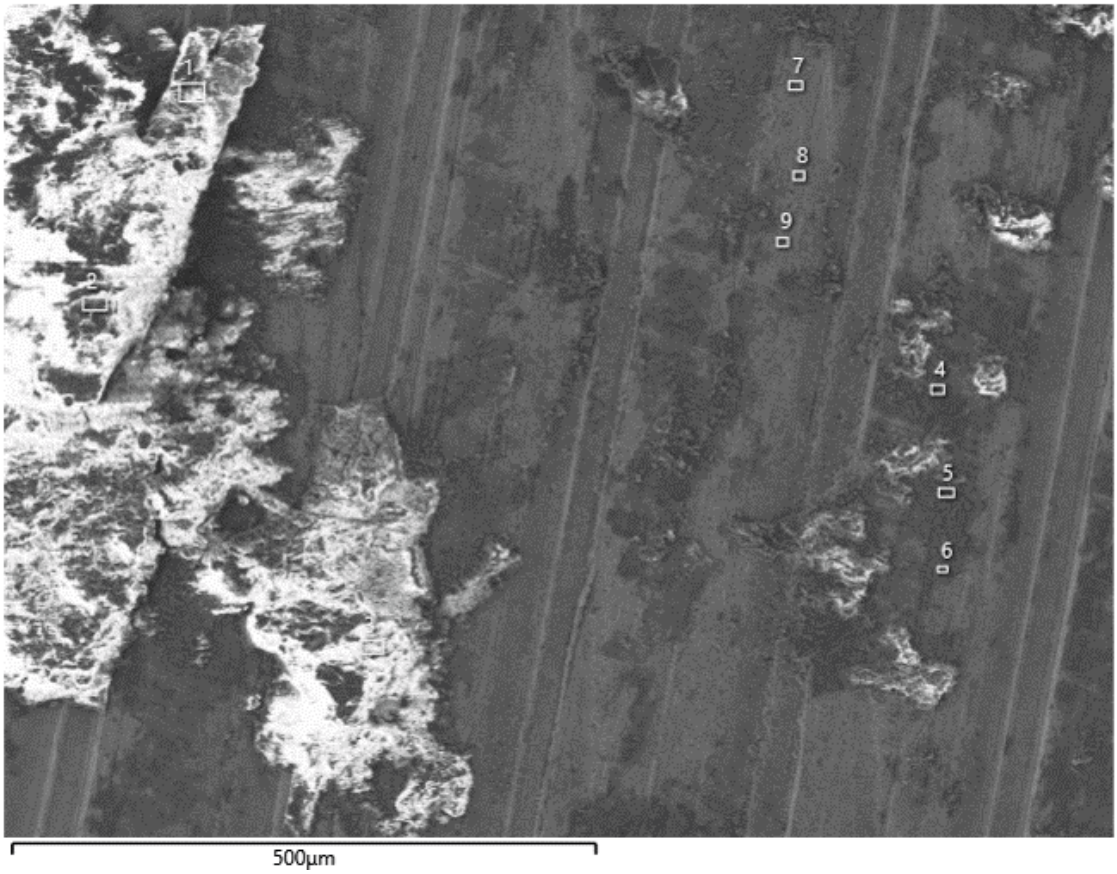

Element (At%)	1	2	3	4	5	6	7	8	9
O	65.82	59.81	54.21	60.53	63.36	56.78	29.97	23.64	21.05
Na	4.51	2.87	2.41	4.67	10.05	4.09			
Mg	1.38	1.49	1.73	1.89	1.05	1.31			
Al	7.29	8.83	10.31	4.1	3.8	3.68			
Si	17.29	22.27	27.36	9.87	9.61	8.1	0.43		0.78
S	0.41	0.72	0.54	0.63	0.52	0.82			
Cl		0.2	0.31	0.32	0.19	0.44	3.67	1.72	0.8
K		0.13	0.23						
Ca	0.23	0.53	0.41	2.55	0.5	0.61			
Fe	0.42	1.1	1.44	0.61	0.54				
Cu	2.64	2.05	1.06	14.83	10.37	24.17	65.93	74.64	77.38
Total	100	100	100	100	100	100	100	100	100

Figure 3-32. *SEM image of MPFA1 site 2. The EDS result of MPFA1 site 2 is shown in the table.*

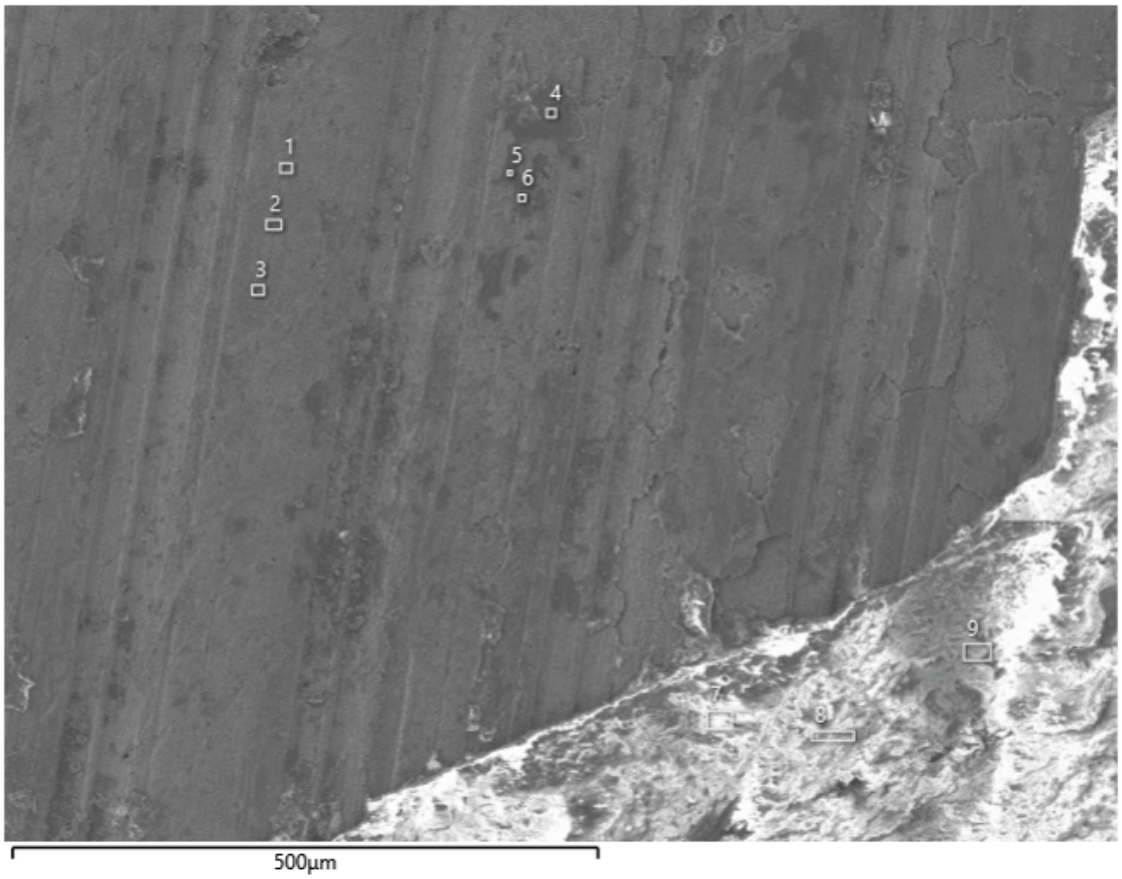

Element (At%)	1	2	3	4	5	6	7	8	9
O	35.07	40.1	36.59	49.16	54.12	57.81	58.29	58.6	54.38
Na				5.4	3.87	3.92			
Mg				0.84	1.08	0.95			
Al				2.18	4.63	4.73	3.5	3.73	2
Si	0.55	0.61		5.22	10.56	11.38	7.94	8.33	4.77
S	0.37	0.51	0.56	2.74	2.03	2.21	0.63	0.61	0.36
Cl	2.57	3.32	3.95	4.51	2.05	3.77	9.25	7.79	13.19
Ca	0.89	0.35		0.24	0.22	0.2	0.22	0.21	
Fe					1.3	1.13			
Cu	60.54	55.11	58.9	29.72	20.13	13.89	20.16	20.74	25.3
Total	100	100	100	100	100	100	100	100	100

Figure 3-33. *SEM image of MPFA1 site 3. The EDS result of MPFA1 site 3 is shown in the table.*

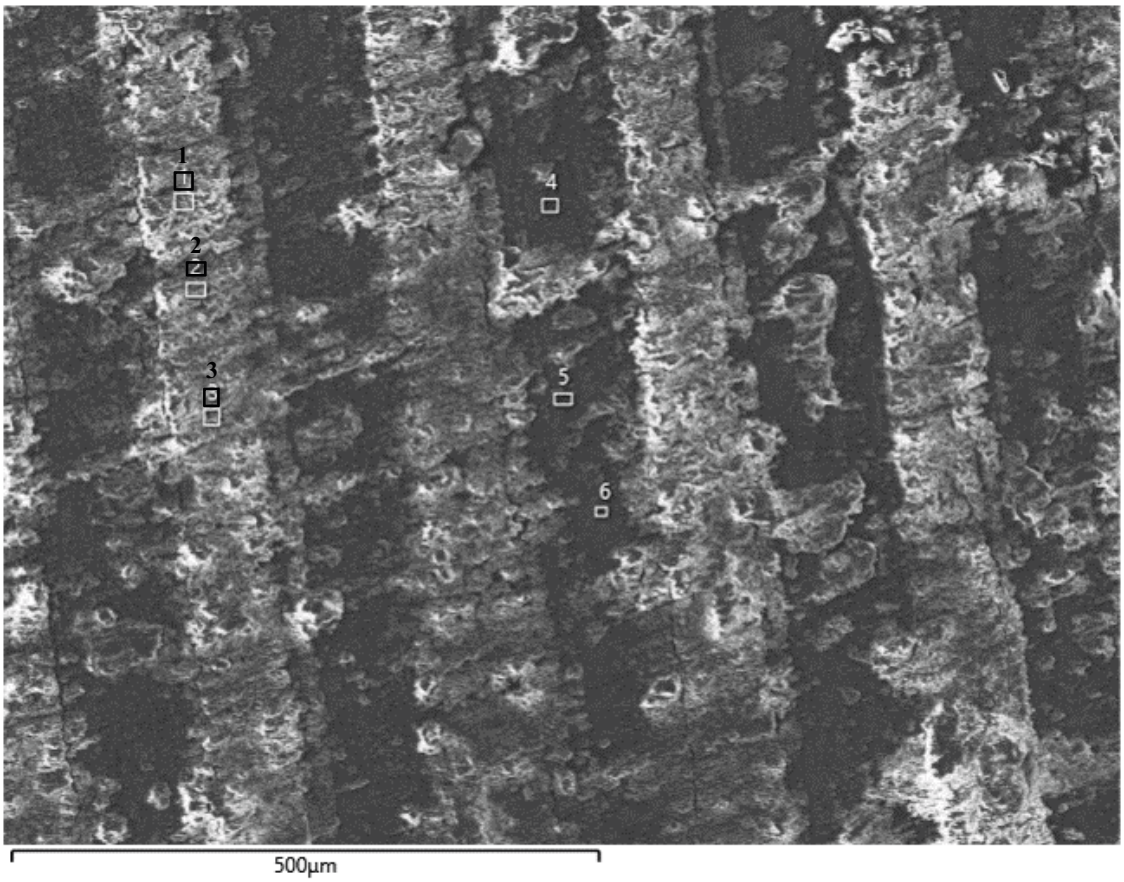

Element (At%)	1	2	3	4	5	6
O	61.69	65.34	62.09	57.24	55.01	53.21
Na	9.49	17.63	14.6	11.04	9.94	8.09
Mg	1		0.72	0.88	0.91	0.99
Al	4.92	1.88	3.16	2.85	3.28	3.38
Si	11.95	4.7	7.7	6.73	7.81	8.15
S	0.6	0.25	0.69	1.07	1.15	1.17
Cl	1.08		0.17	0.72	0.95	1.09
K	0.17					
Ca	0.38	0.2	0.66	0.6	0.71	1.34
Fe			1.05		0.7	
Cu	8.74	9.98	9.16	18.87	19.54	22.58
Total	100	100	100	100	100	100

Figure 3-34. *SEM image of MPFA1 site 4. The EDS result of MPFA1 site 4 is shown in the table.*

Element (At%)	1	2	3	4	5	6
O	60.48	61.75	61.1	66.12	64.43	65.42
Na				16.92	14.66	14.7
Mg	1.48					
Al	2.46	2.75	3.02	1.43	2.15	2.28
Si	6.03	6.23	7.31	3.34	5.38	5.38
S	0.69	0.77	0.8	0.31	0.72	0.82
Cl	0.47	0.54	0.55	0.22	0.44	0.46
Ca	1.04	1.41	0.83		0.27	0.26
Fe					0.64	
Cu	27.36	26.54	26.39	11.66	11.32	10.69
Total	100	100	100	100	100	100

Figure 3-35. *SEM image of MPFA1 site 5. The EDS result of MPFA1 site 5 is shown in the table.*

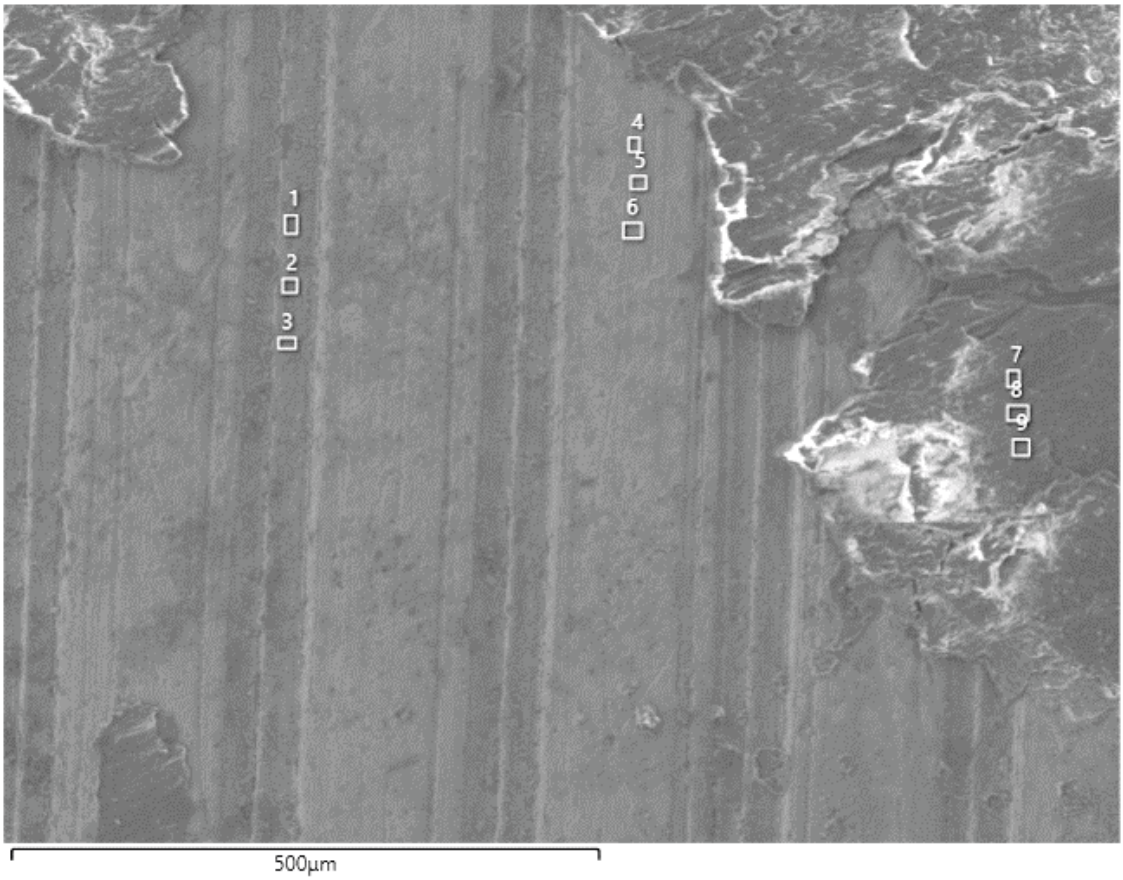

Element (At%)	1	2	3	4	5	6	7	8	9
O	45.01	50.15	41.5	31.16	30.74	31.75	61.77	61.98	63.51
Na							3.19	3.24	3.15
Mg	1.02	0.93					1.34	1.28	1.28
Al	1.28	1.22					7.8	7.53	7.56
Si	2.4	3.02	0.7		0.43		18.79	18.49	18.28
S	1.65	1.66	1.33		0.43	0.48	0.79	0.77	0.69
Cl	1.59	0.88	1.46	2.55	2.22	3.28	0.53	0.75	0.47
K							0.32	0.12	0.18
Ca	4.36	6.38	4.42				0.77	0.67	0.74
Fe							0.99	0.68	0.86
Cu	42.68	35.76	50.59	66.29	66.19	64.48	3.71	4.5	3.27
Total	100	100	100	100	100	100	100	100	100

Figure 3-36. *SEM image of MPFA1 site 6. The EDS result of MPFA1 site 6 is shown in the table.*

Element (At%)	1
O	57.41
Na	5.04
Mg	1.31
Al	6.19
Si	14.38
S	0.58
Cl	0.33
K	0.09
Ca	1.05
Fe	0.87
Cu	12.76
Total	100

Figure 3-37. *SEM image of MPFA1 site 1. The EDS result of MPFA1 site 1 is shown in the table. EDS over larger area.*

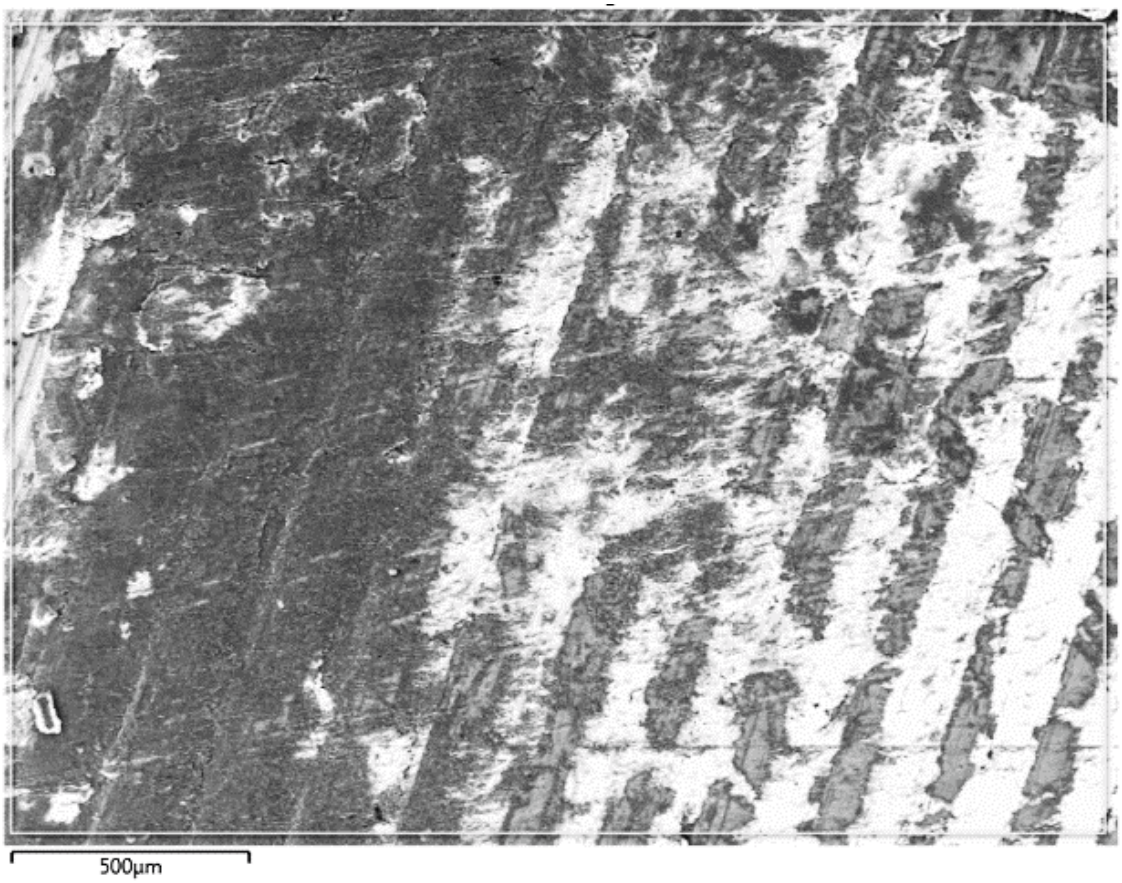

Element (At%)	1
O	61.94
Na	6.4
Al	5.55
Si	13.52
S	0.92
Cl	0.57
K	0.12
Ca	1.35
Fe	0.82
Cu	8.81
Total	100

Figure 3-38. *SEM image of MPFA1 site 2. The EDS result of MPFA1 site 2 is shown in the table. EDS over larger area.*

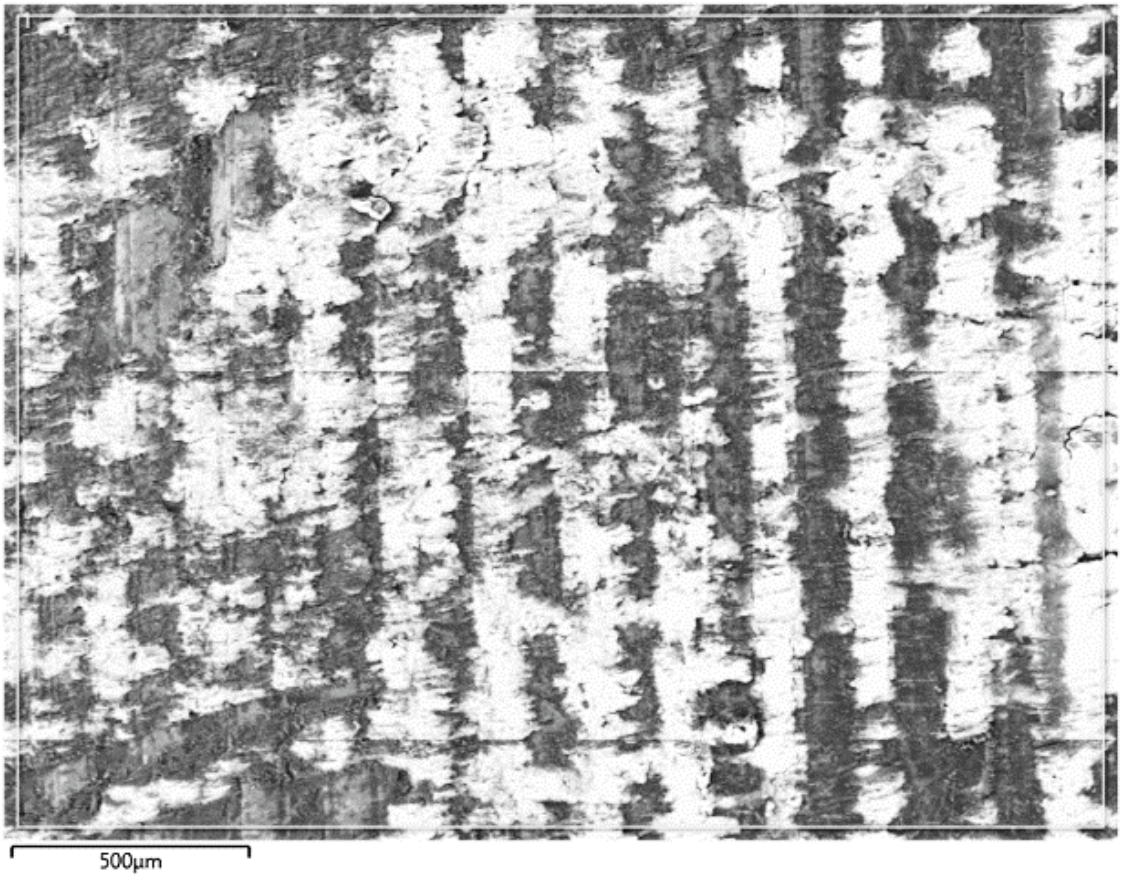

Element (At%)	1
O	63.69
Na	10.55
Al	3.67
Si	8.97
S	0.8
Cl	0.58
K	0.1
Ca	0.96
Fe	0.82
Cu	9.87
Total	100

Figure 3-39. *SEM image of MPFA1 site 3. The EDS result of MPFA1 site 3 is shown in the table. EDS over larger area.*

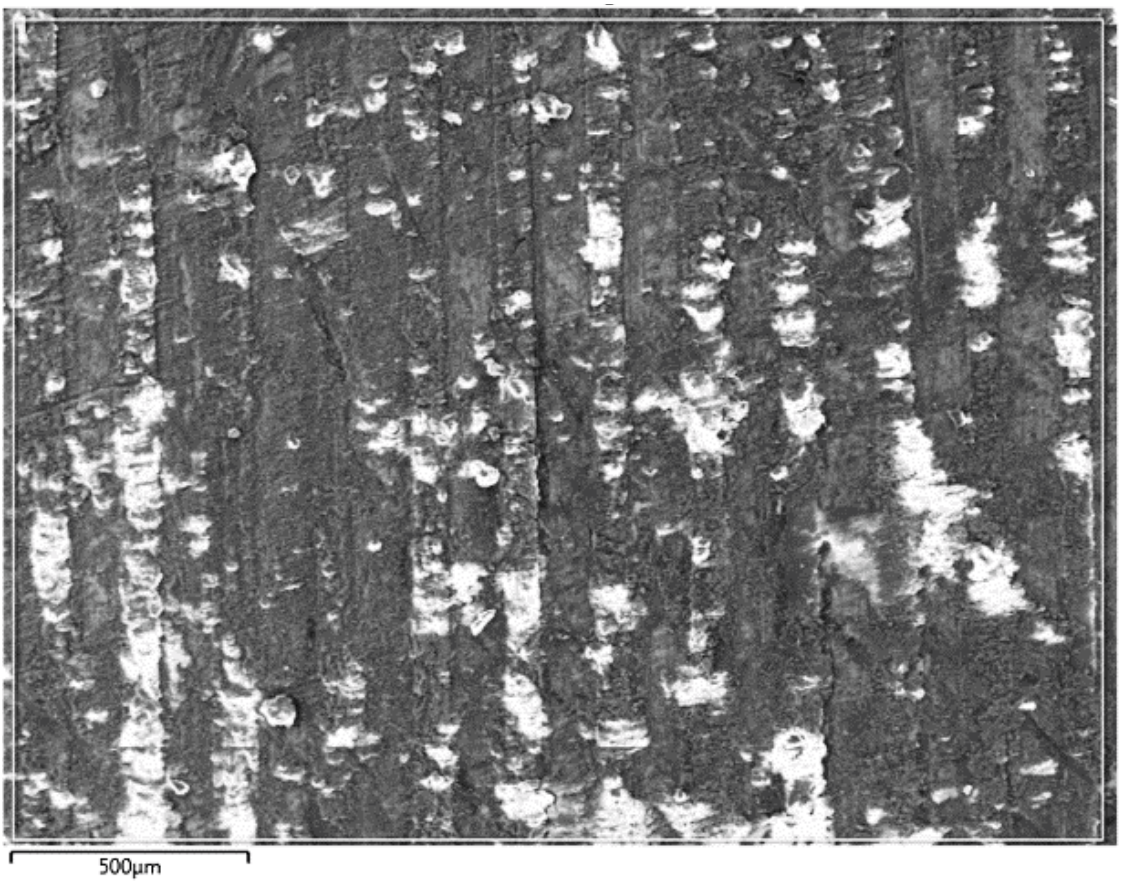

Element (At%)	1
N	15.7
O	53.46
Na	8.78
Al	3.36
Si	7.98
S	0.56
Cl	0.35
K	0.07
Ca	0.82
Ti	0.12
Fe	0.7
Cu	8.1
Total	100

Figure 3-40. *SEM image of MPFA1 site 4. The EDS result of MPFA1 site 4 is shown in the table. EDS over larger area.*

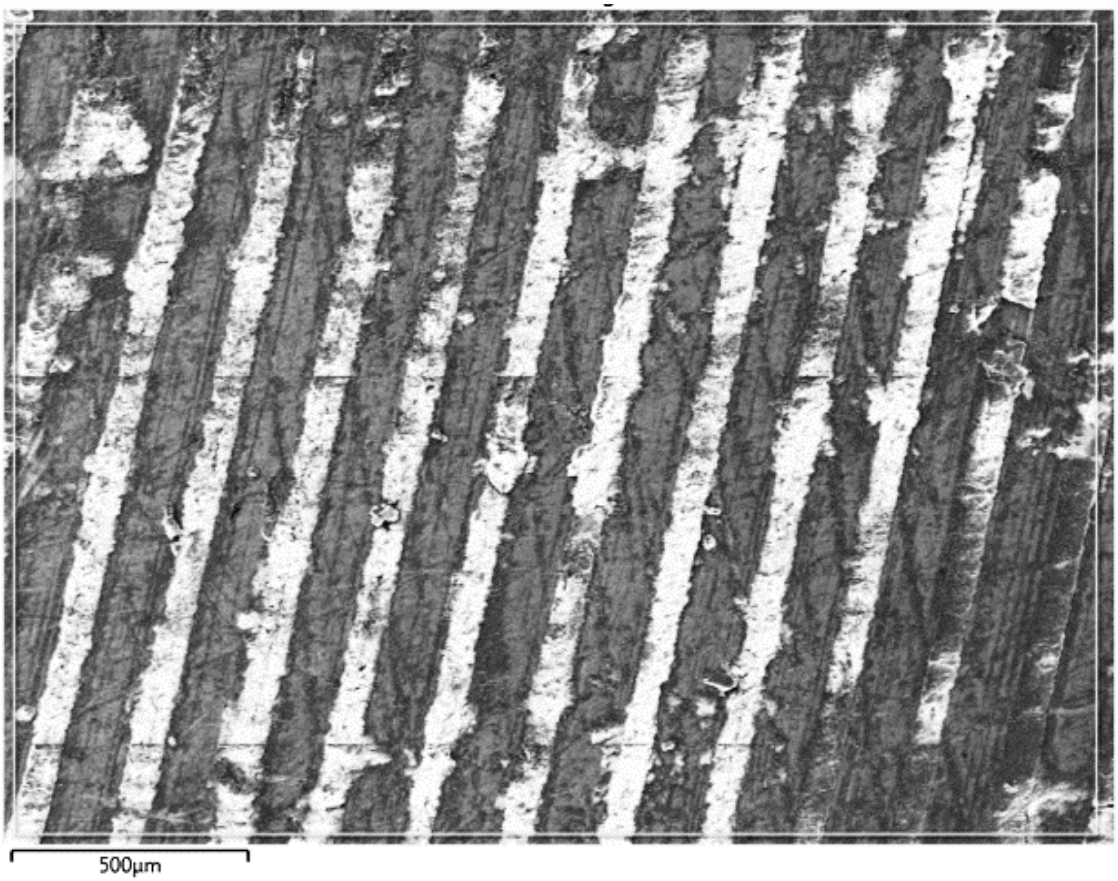

Element (At%)	1
O	58.84
Na	7.77
Al	3.77
Si	9.18
S	0.92
Cl	0.63
Ca	0.92
Fe	0.67
Cu	17.29
Total	100

Figure 3-41. *SEM image of MPFA1 site 5. The EDS result of MPFA1 site 5 is shown in the table. EDS over larger area.*

XRD

Corrosion products were analyzed in the XRD on the sample coupon surfaces. Peaks of cuprite at 36.5 and 61.5 2θ could be found for MPFA1, more visible here than for PC901, along with metallic copper, which can be seen in Figure 3-42.

FTIR/IRRAS

IRRAS measurements were made on the MPFA1 coupon sites and their corresponding IR-spectra can be seen in Figure 3-43. Only site 6 shows a clear cuprite peak around 630 cm^{-1}. Double peaks around 1 300–1 600 cm^{-1} are again visible and indicates malachite. Peak at 1 000 cm^{-1}, 3 600 cm^{-1} and double peaks at 500–600 cm^{-1} indicate bentonite.

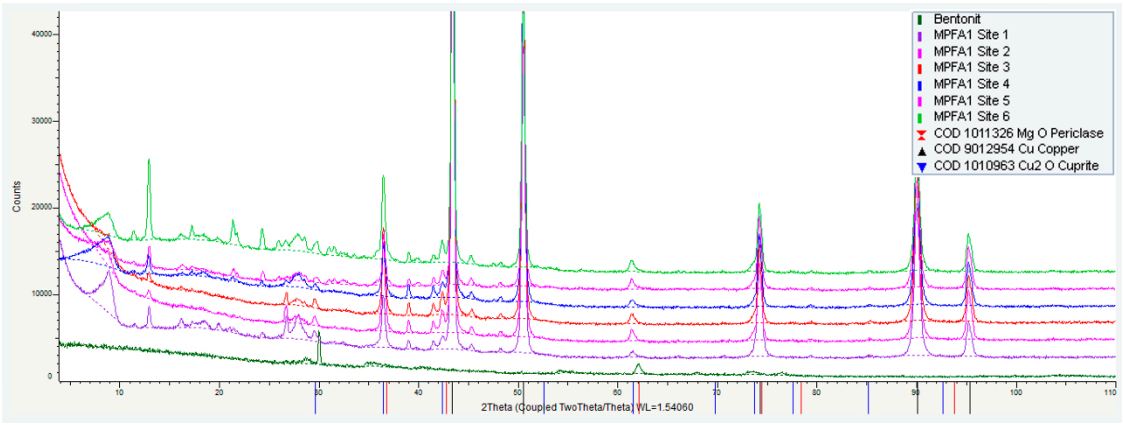

Figure 3-42. *XRD diffractograms obtained from the surface of MPFA1.*

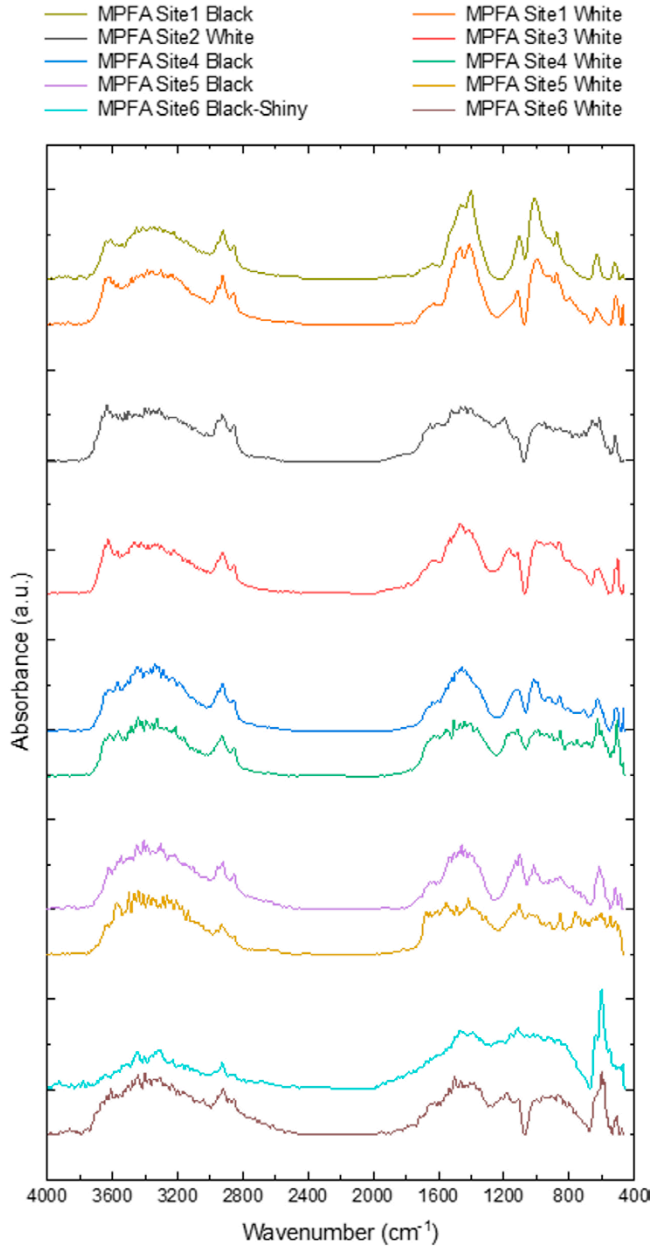

Figure 3-43. *Infrared spectra from FTIR/IRRAS measurement on surface of sample MPFA1.*

3.3.2 Cross section analysis

SEM/EDS

The cross section samples were cut in half, cast into epoxy resin while mounted surface to surface, polished, and analysed with SEM/EDS. Images and EDS analysis after dry grinding of the cross section of MPFA1 can be seen in Figures 3-44–3-46. Subsequently the cross section was diamond polished and analysed, which can be seen in Figures 3-47–3-51. The cross section images show a slightly rough surface appearance, with a porous oxide layer visible for some samples, although no clear explanation for this have been found. No clear signs of localised corrosion were observed. The SEM images seem to show a slightly thicker oxide layer in general than for PC901. However, no quantitative comparison has been attempted. The EDS result show bentonite and small amounts of chlorine while sulfur is not distinctly detected.

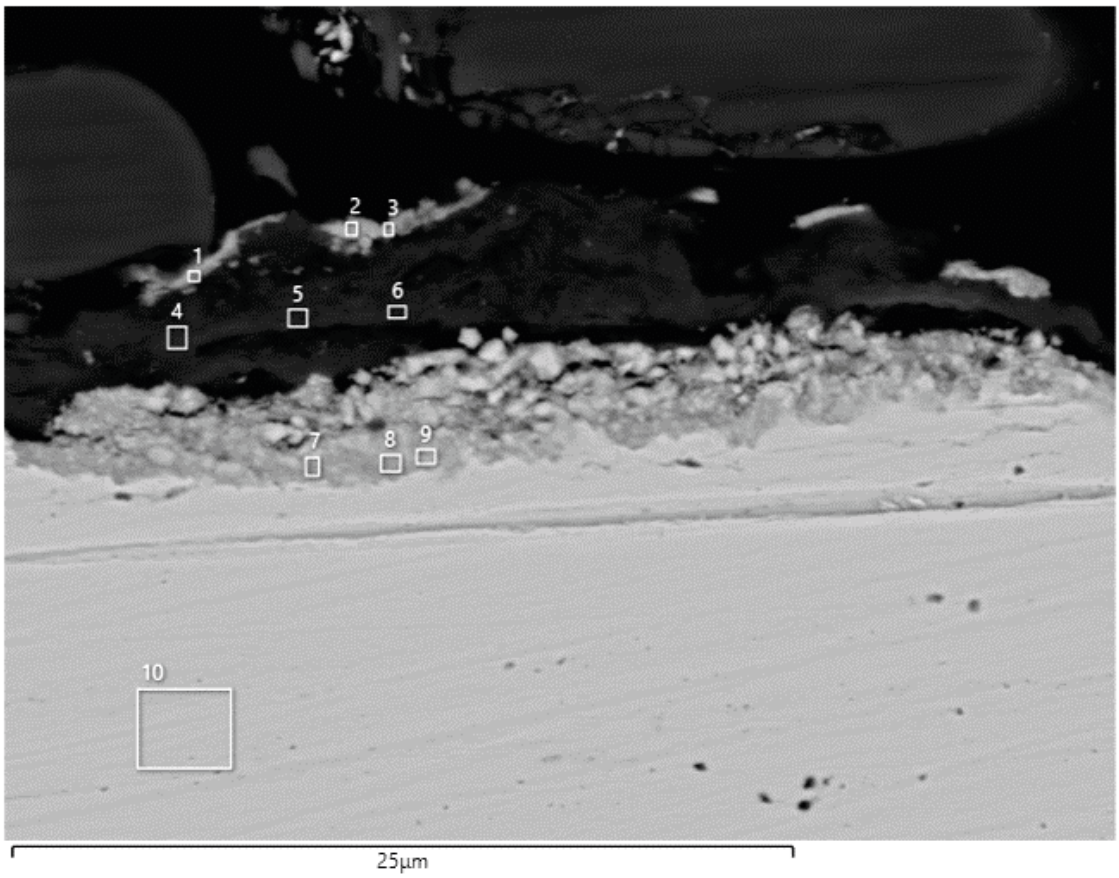

Element (At%)	1	2	3	4	5	6	7	8	9	10
O	22.73	12.97	16.59	41.4	41.66	40.04	8.79	8.86	4.76	
Na				1.18	1.78	1.56				
Mg	0.94	0.73	1	1.84	1.72	1.87				
Al	4.76	1.55	3.35	11.52	10.5	11.04				
Si	13.55	2.84	6.69	28.84	29.19	29.33				
S	0.33	0.17	0.3	0.55	0.75	0.66	0.74	0.72	0.52	
Cl	2.41	3.83	3.56	0.4	0.42	0.48	1.39	1.47	1.26	
K				0.2	0.13	0.14				
Ca	1.4	0.7	0.76	0.57	0.72	0.99	0.58	0.24		
Ti			0.8			0.16				
Fe	0.93	0.47	0.62	2.46	2.3	2.57				
Cu	52.96	76.75	66.31	11.06	10.84	11.16	88.51	88.72	93.47	100
Total	100	100	100	100	100	100	100	100	100	100

Figure 3-44. *SEM image of the cross section of MPFA1. The EDS result of the cross section of MPFA1 is shown in the table.*

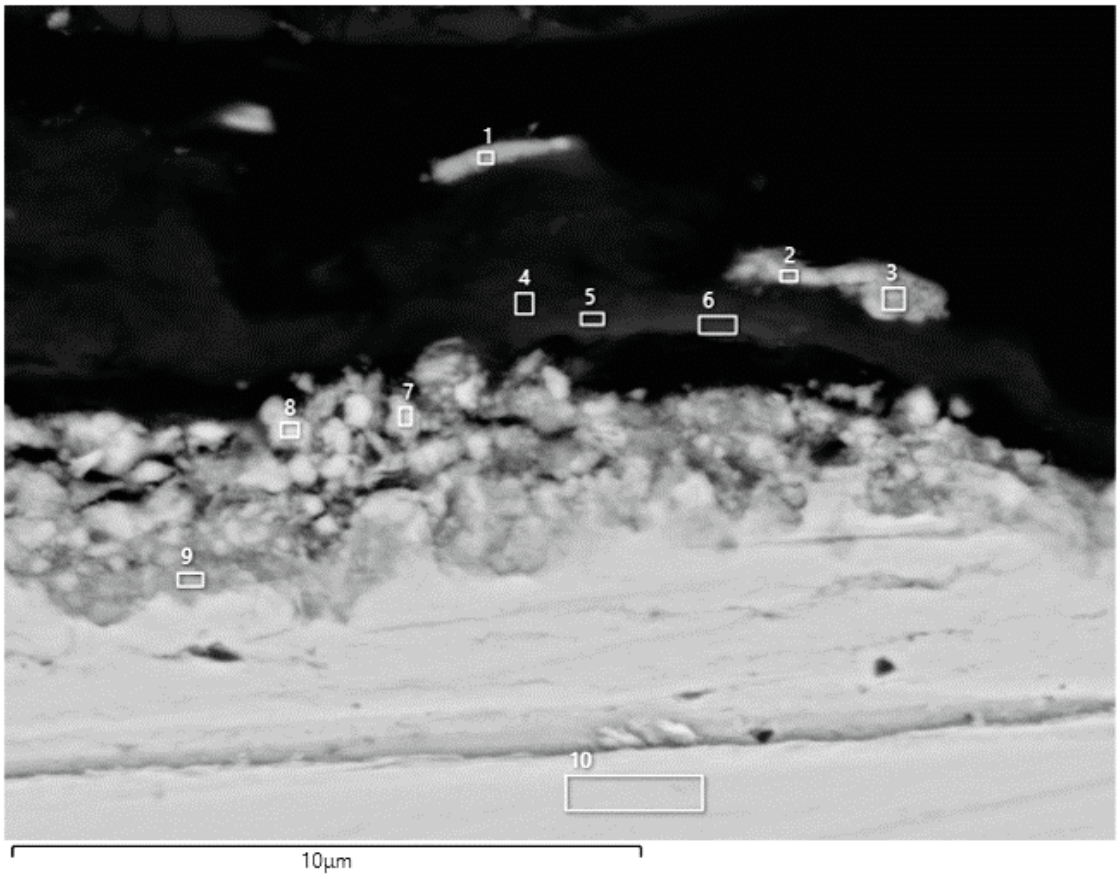

Element (At%)	1	2	3	4	5	6	7	8	9	10
O	19.81	19.08	17.08	39.8	39.94	39.09	10.18	14.16	7.38	
Na				2.02	2.34	2.82				
Mg	1	1.11	0.93	1.86	1.89	1.85		0.29		
Al	4.73	4.42	3.62	10.38	9.74	9.57	0.82			
Si	9.83	8.61	7.07	27.1	25.35	23.16	2.11	2.13		
S	0.18	0.52	0.52	0.9	0.87	0.9	0.73	0.84	0.62	
Cl	1.43	2.74	2.68	0.5	0.55	0.7	1.76	1.44	1.56	
K				0.11	0.19	0.58				
Ca	0.66	0.76	0.71	1.4	1.85	1.23	0.5	0.34	0.38	
Fe	0.61	0.49	0.87	2.14	2.09	1.82		0.22		
Cu	61.74	62.28	66.52	13.79	15.18	18.27	83.88	78.22	90.06	100
Br								2.37		
Total	100	100	100	100	100	100	100	100	100	100

Figure 3-45. *SEM image of the cross section of MPFA1. The EDS result of the cross section of MPFA1 in the table.*

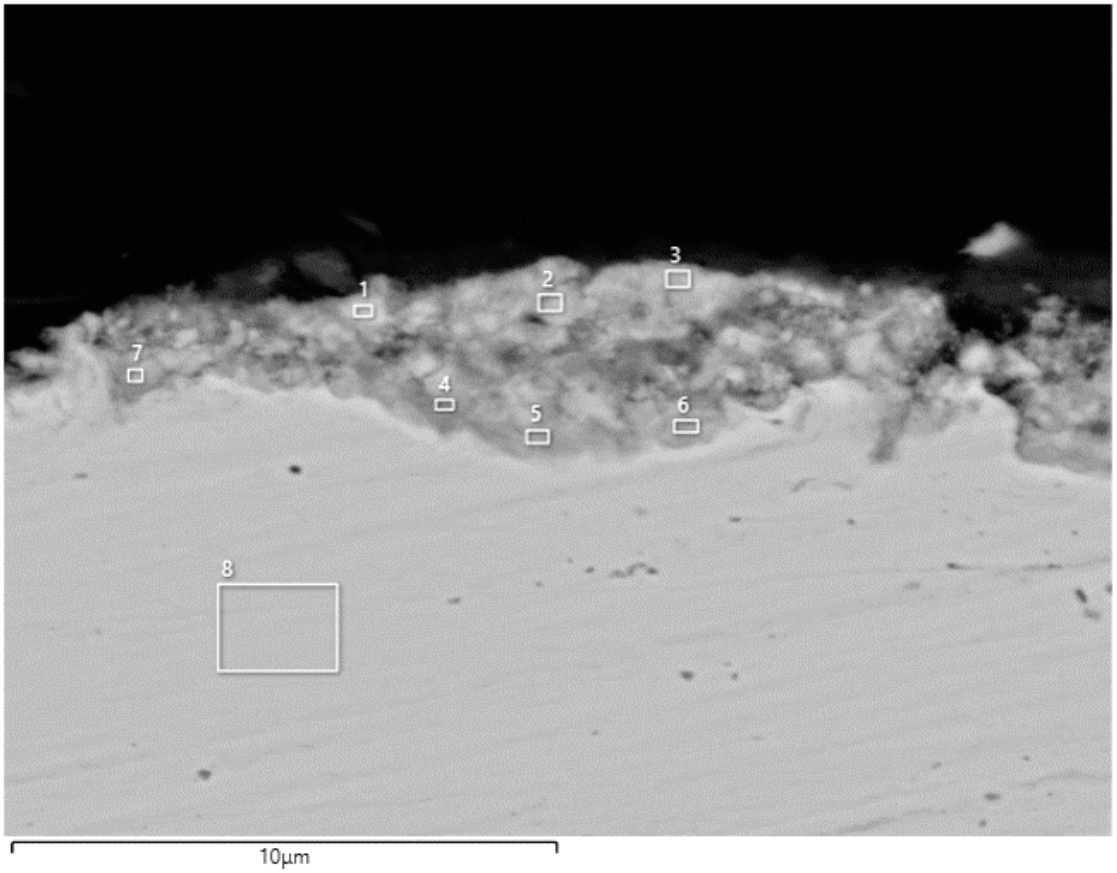

Element (At%)	1	2	3	4	5	6	7	8
O	12.29	11.83	13.49	9.25	6.44	8.78	10.21	
Mg	0.26	0.38	0.62					
Al	0.38	0.17	0.46					
Si	5.74	0.36	0.92			0.15		
S	1.01	0.78	0.8	0.75	0.57	0.82	0.72	
Cl	0.57	0.78	0.6	0.65	0.54	0.72	0.66	
Ca	0.74	0.58	2.18				0.17	
Fe			0.19	0.2				
Cu	79.01	85.13	80.74	89.14	92.46	89.53	88.24	100
Total	100	100	100	100	100	100	100	100

Figure 3-46. *SEM image of the cross section of MPFA1. The EDS result of the cross section of MPFA1 is shown in the table.*

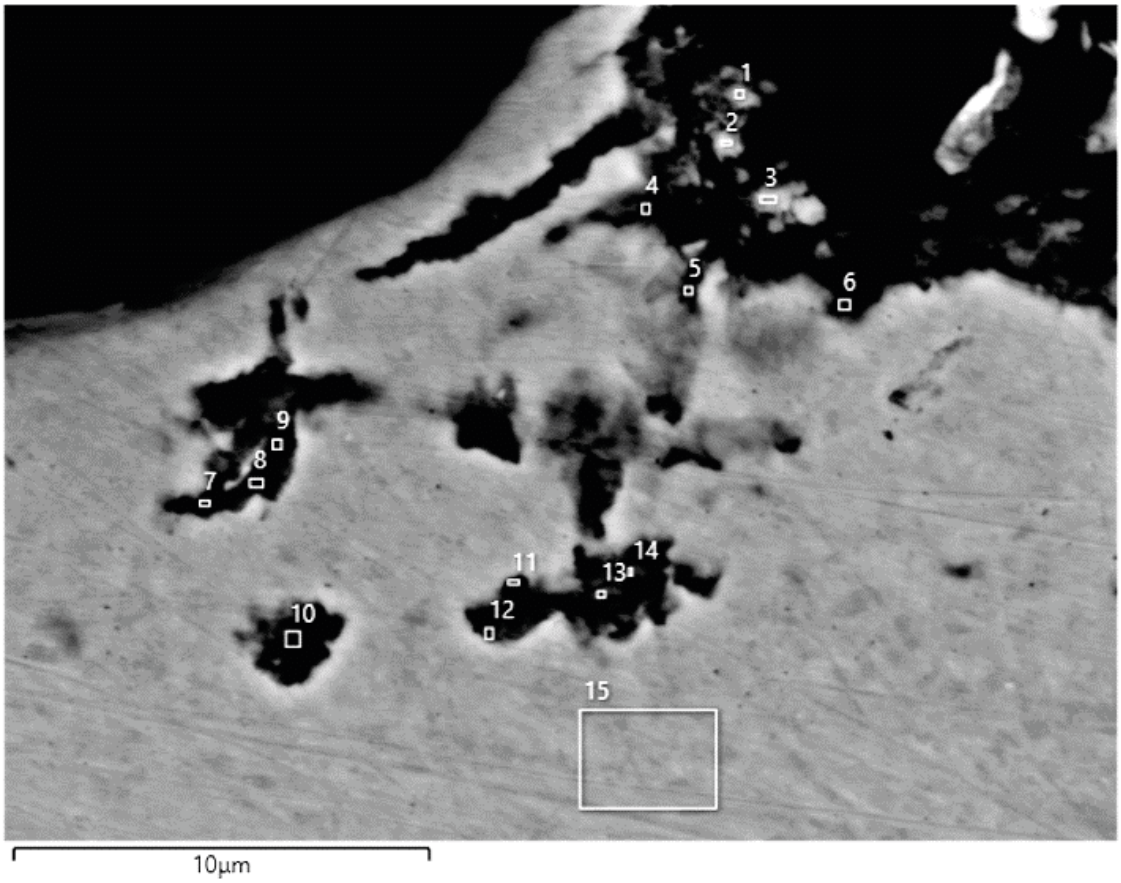

Element (At%)	1	2	3	4	5	6	7	8	9	10	11	12	13	14	15
O	41.85	39.95	42.78	29.68	26.73	36.05	25.32	27.97	29.45	22.04	21.46	21.11	30.29	29.56	
Mg	0.89	0.48	0.64												
Al	2.65	1.42	1.54	0.51	0.54	1.79							0.37		
Si	7.87	4.45	4.65	3.53	2.45	6.01	1.08	0.71	0.57	1.58	0.57	0.24	1.14	0.99	
S	0.28	0.22	0.17	0.33	0.25	0.3	0.23	0.21	0.2	0.19			0.28	0.81	
Cl	1.19	1.4	1.17	1.58	1.54	1.23	1.47	1.68	1.82	2.09	1.59	1.94	1.72	1.69	
Ca	2.35	1.29	1.24	1.18	1.26	1.3	0.18		0.13	0.18	0.17	0.13	0.2	0.34	
Fe		0.11	0.11	0.16	0.15	0.2							0.11	0.13	
Cu	42.91	50.67	47.68	63.03	67.08	53.12	71.73	69.44	67.83	73.92	76.21	76.58	65.89	66.48	100
Total	100	100	100	100	100	100	100	100	100	100	100	100	100	100	100

Figure 3-47. *SEM image of the cross section of MPFA1, diamond polished. The EDS result of the cross section of MPFA1, diamond polished, in the table.*

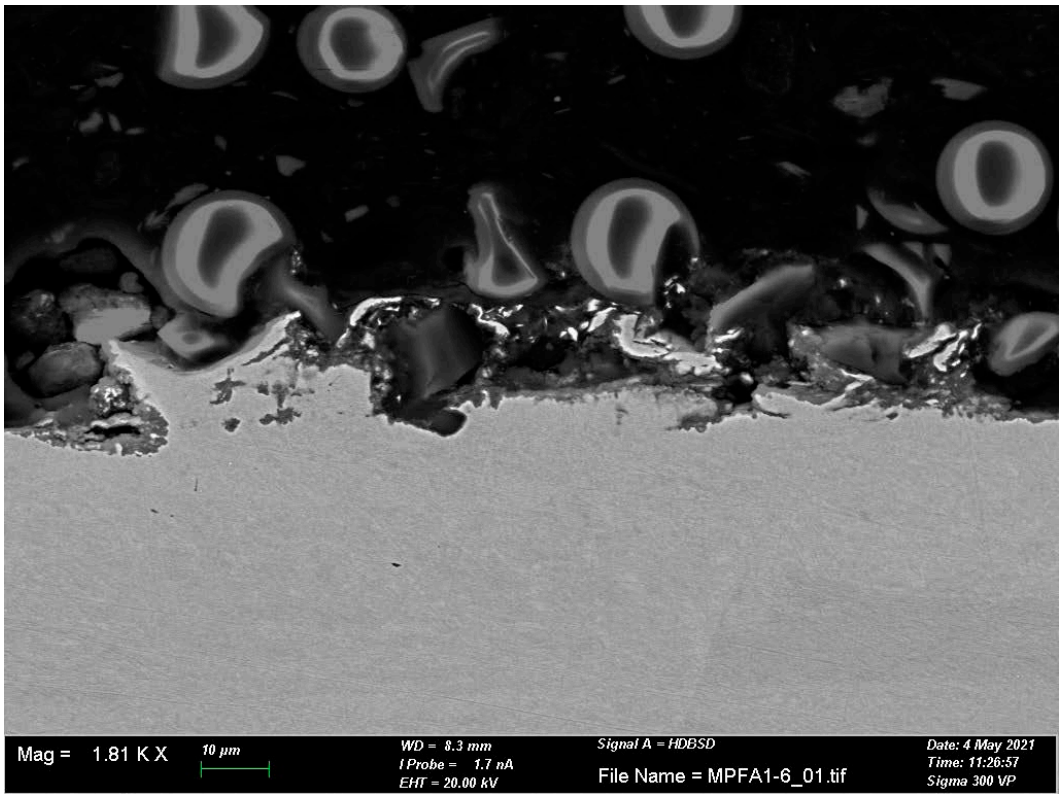

Figure 3-48. *SEM image of the cross section of MPFA1, at higher magnification (×1 800) than in Figure 3-50, showing the appearance of the surface after dry grinding and subsequent polishing. It appears that the surface is uneven, which may correspond to the machining process prior to exposure (grooves approximately 10 µm deep into the surface). Some areas of deformation are observed, possibly due mechanical forces applied during polishing of the sample.*

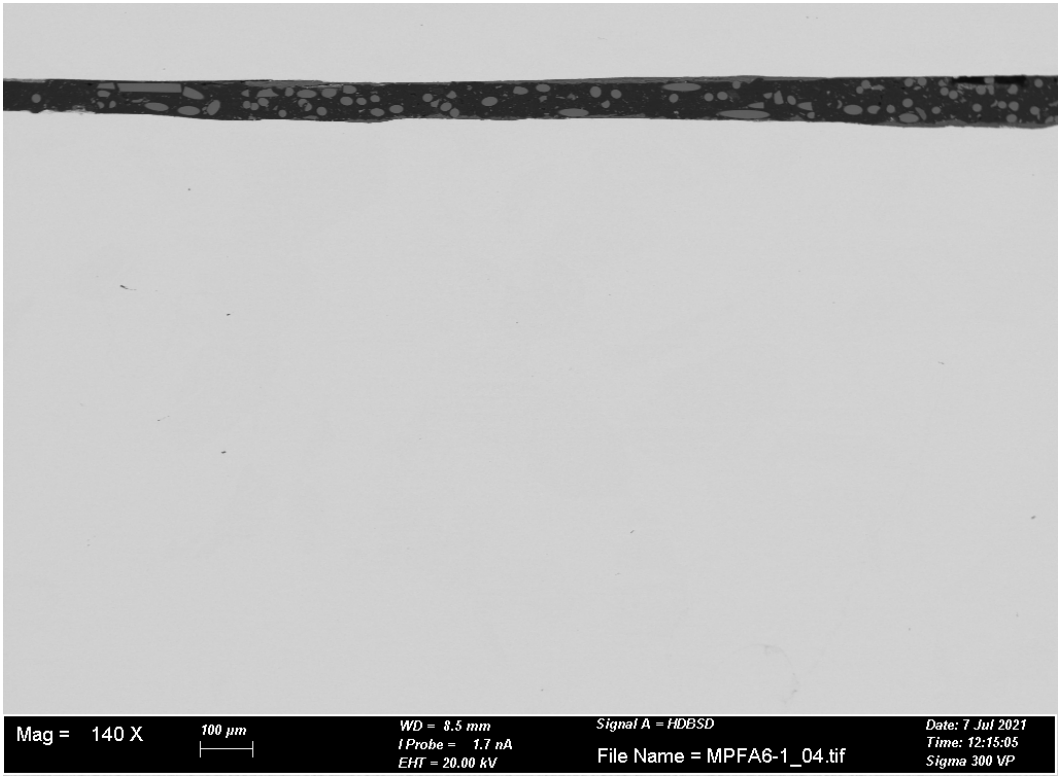

Figure 3-49. *SEM image overview of cross section mounted in epoxy resin surface to surface at ×140 magnification, MPFA1.*

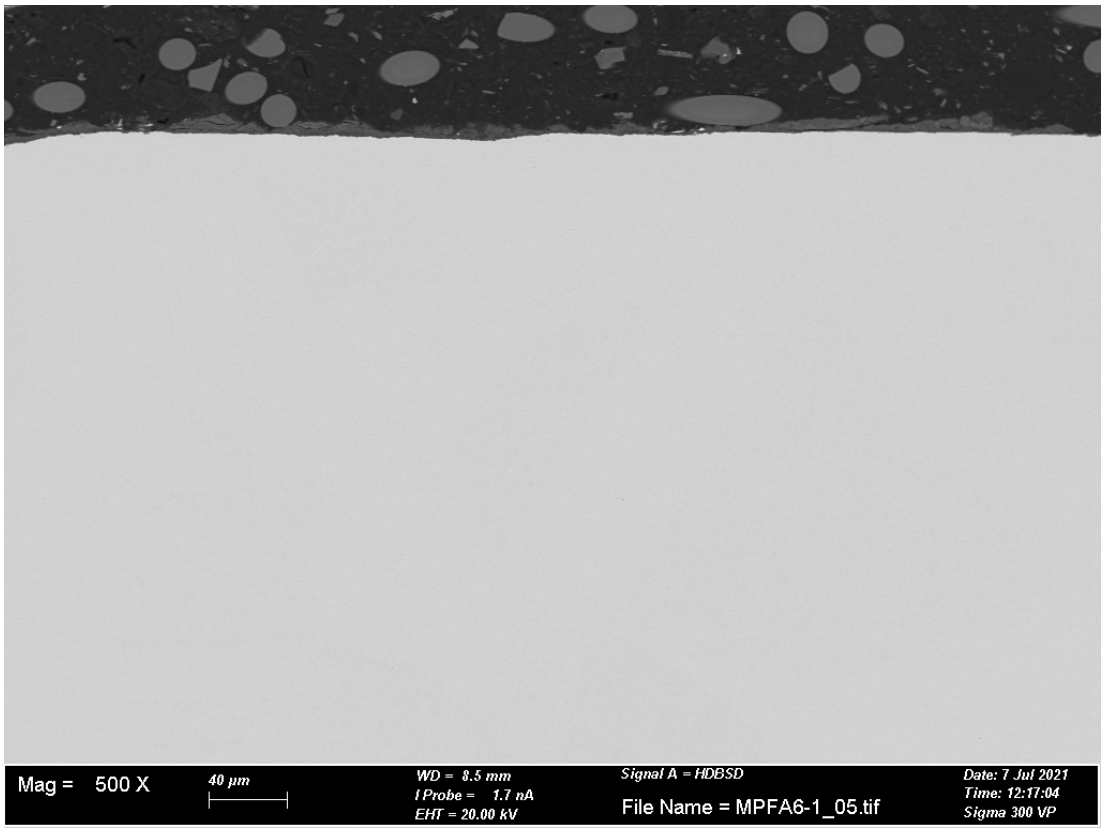

Figure 3-50. *SEM image overview of cross section at ×500 magnification, MPFA1.*

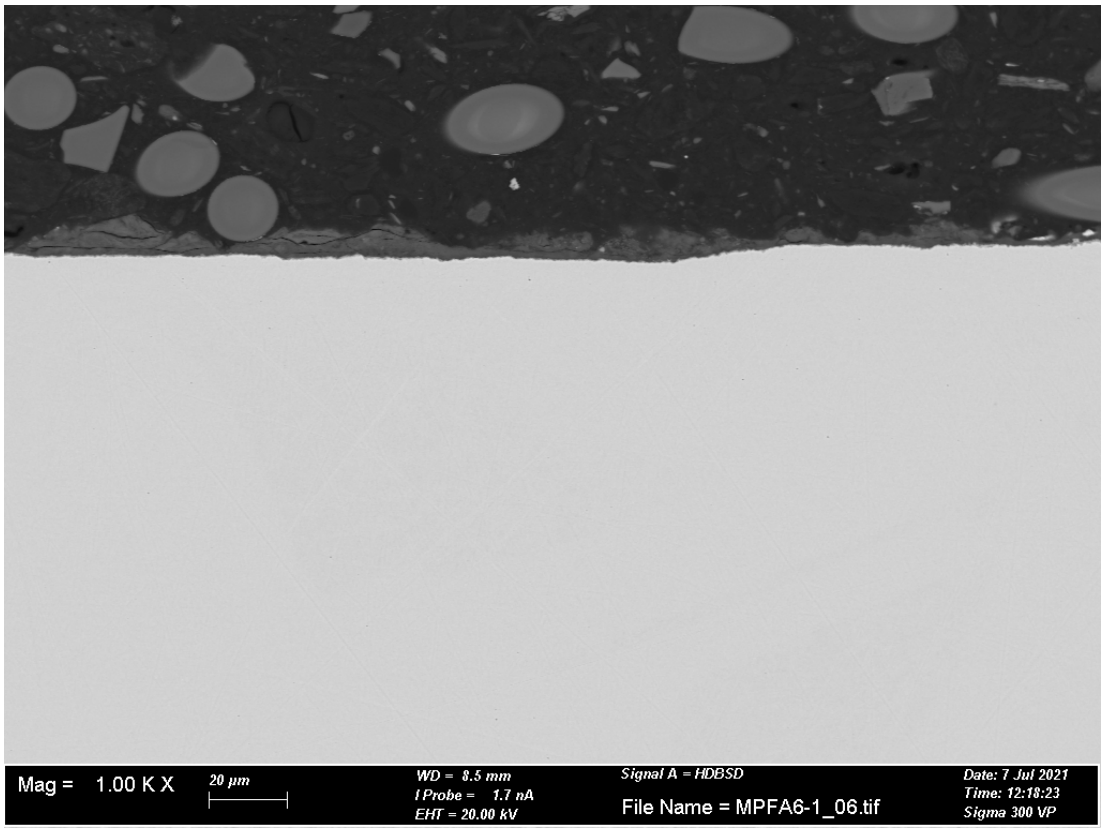

Figure 3-51. *SEM image overview of cross section at ×1 000 magnification, MPFA1.*

3.4 LFA2

An overview of filter housing LFA2 is presented in Figure 3-52, with its designated area for sample coupons marked with a black rectangle. Sample preparation was carried out equivalently as for PC901. An overview of the four sample coupons for filter housing LFA2 can be seen in Figure 3-53 along with their designated surface analysis sites, indicated with red rectangles.

3.4.1 Surface analysis

SEM/EDS

SEM/EDS analysis was carried out on the surface of the samples. Images showed clear machining marks from the manufacturing of the filter housings, similar to the previous filter housings. Elemental analysis on the surface showed mainly copper and oxygen with bentonite clustered and spread on most surfaces. Small amounts of iron and chlorine were detected for LFA2, and the level of sulfur was generally < 1 at%, see Figures 3-54–3-61 and corresponding tables. Similar to previous filter housings, light grey areas appear to be bare copper surface with a thin oxide layer and darker areas to be bentonite and corrosion products.

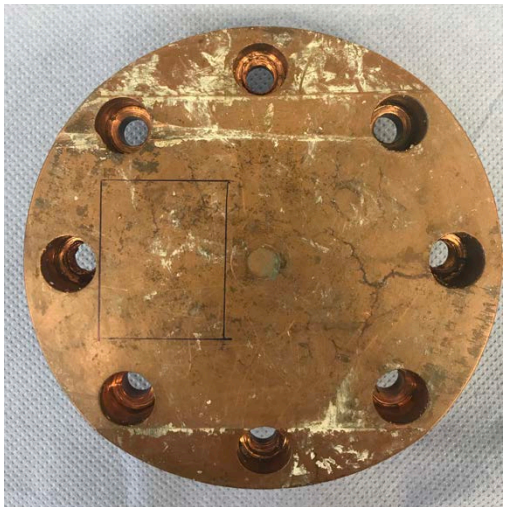

Figure 3-52. *Overview of filter housing LFA2 and the area, marked with a black rectangle, of which sample coupons for analysis were to be taken.*

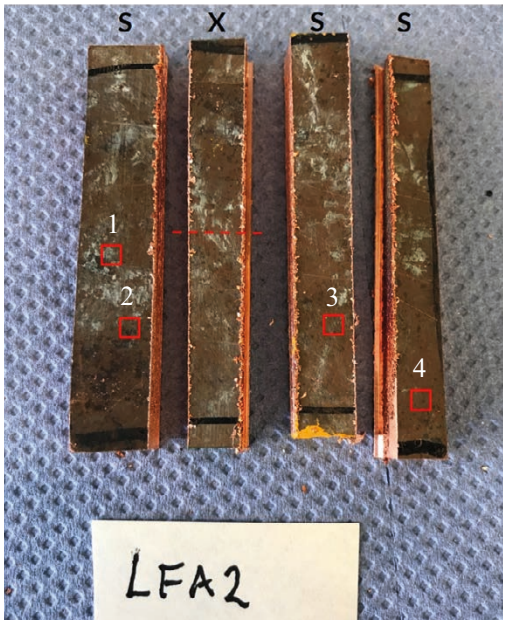

Figure 3-53. *The four test coupons taken from filter housing LFA2. 'S' denotes coupons chosen for surface analysis and 'X' for cross section analysis.*

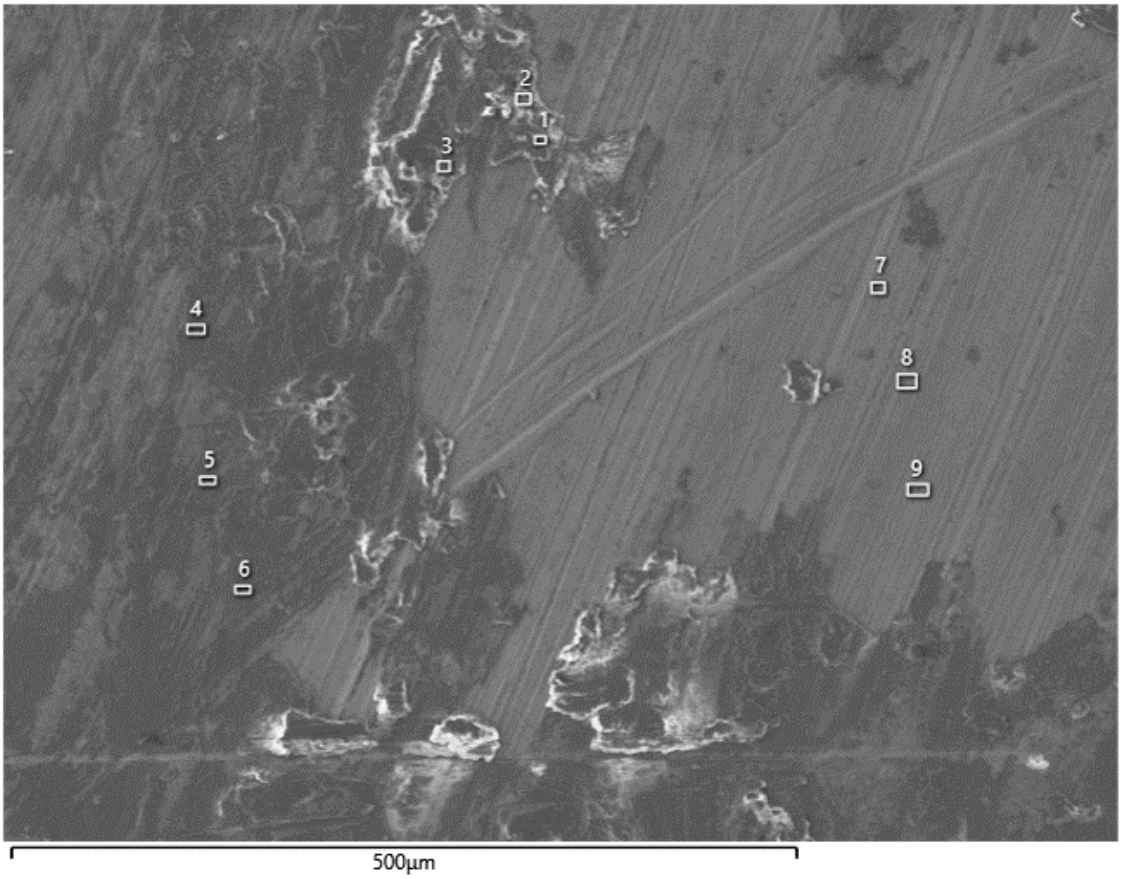

Element (At%)	1	2	3	4	5	6	7	8	9
O	48.88	42.27	46.54	45.35	44.37	44.1	5.47	7.24	5.97
Na	2.06	1.95	1.84	1.69	1.31	1.87			
Mg	1.59	1.77	1.72	1.63	1.62	1.59			
Al	10.98	12.7	11.64	10.02	9.78	9.62	0.15		
Si	29.06	32.71	28.97	25.61	24.4	23.73	0.35	0.3	0.19
S		0.3	0.36	0.26	0.16	0.25	0.41	0.71	0.62
Cl	0.23	0.32	0.31	0.73	1.26	1.12	0.57	0.53	0.4
K	0.33	0.27	0.12	0.13		0.14			
Ca	0.88	0.91	1.3	1.4	1.09	1.46	0.29	0.5	0.49
Fe	2.13	2.79	2.4	2.2	2.28	2.2			
Cu	3.85	4.01	4.8	10.98	13.74	13.91	92.76	90.71	92.33
Total	100	100	100	100	100	100	100	100	100

Figure 3-54. *SEM image of LFA2 site 1. The EDS result of LFA2 site 1 is shown in the table.*

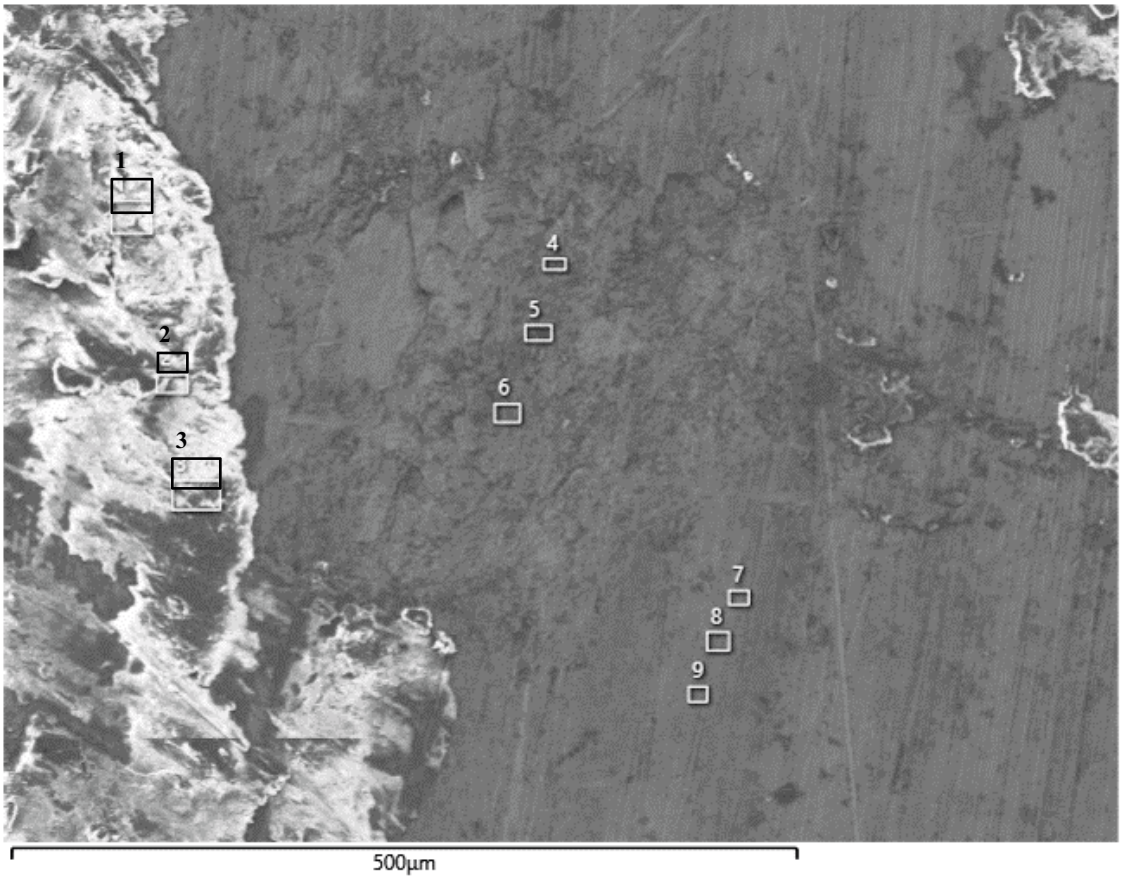

Element (At%)	1	2	3	4	5	6	7	8	9
O	49.3	45.66	48.58	29.68	24.86	15.62	14.1	14.03	14.21
Na	2.09	1.65	1.78						
Mg	1.64	1.54	1.77	0.85	1.04	0.58	0.31	0.35	0.3
Al	11.19	10.3	10.93	2.56	1.25	0.4	0.34	0.3	0.35
Si	27.3	26.72	28.14	6.2	3	0.91	0.73	0.66	0.56
P								0.12	0.08
S	1.02	0.82	0.29	1.29	0.97	0.89	0.94	0.85	0.94
Cl	0.31	0.92	0.3	0.67	1.48	0.7	0.97	0.95	0.91
K	0.26	0.19	0.55		0.19				
Ca	2.35	1.97	1.39	14.01	14.18	9.25	4.78	4.23	4.19
Ti	0.31	0.21	0.22						
Fe	1.85	2.4	2.74		1.46				
Cu	2.38	7.62	3.31	44.74	51.57	71.65	77.83	78.49	78.46
Total	100	100	100	100	100	100	100	100	100

Figure 3-55. *SEM image of LFA2 site 2. The EDS result of LFA2 site 2 is shown in the table.*

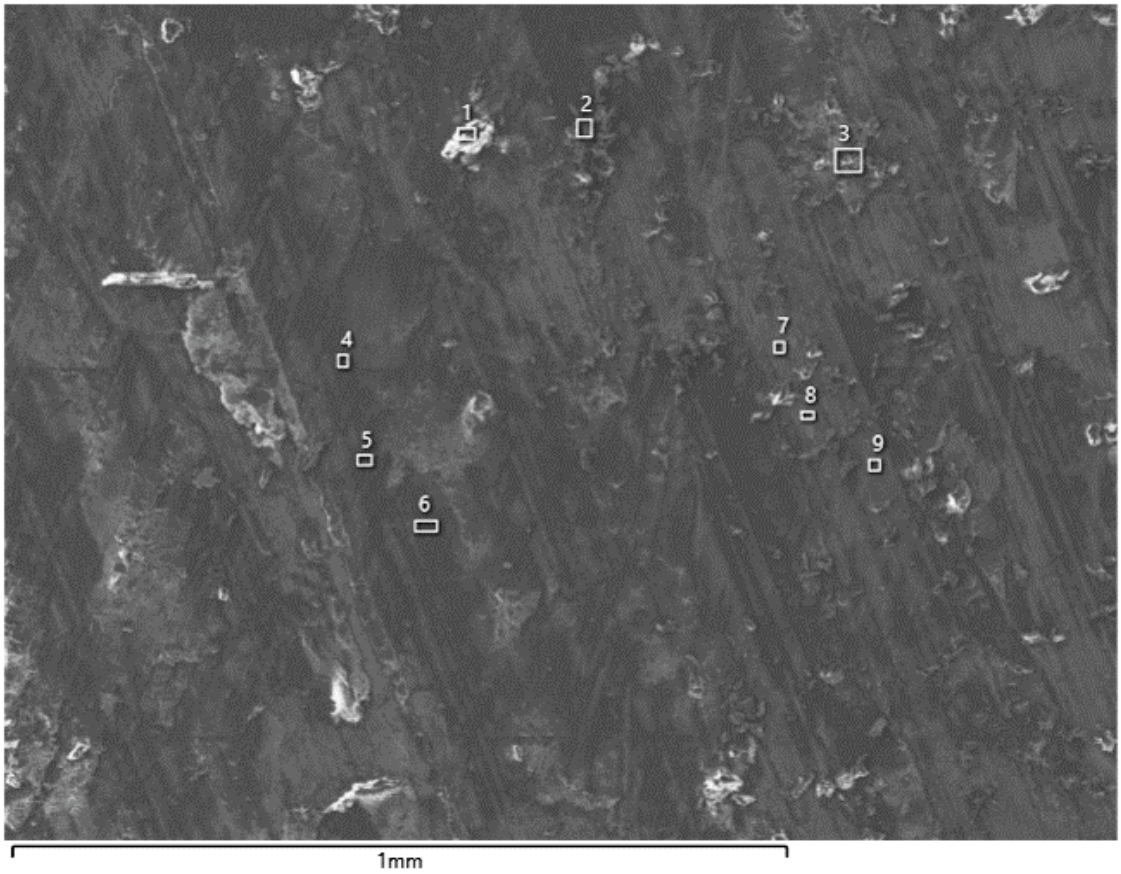

Element (At%)	1	2	3	4	5	6	7	8	9
O	46.11	36.92	42.76	40.99	36.64	41.91	15.14	6.46	13.83
Na	1.7	1.19	1.3	1.09	0.95	1.29			
Mg	1.72	1.61	1.65	1.53	1.47	1.53	0.51	0.27	0.66
Al	10.37	10.38	10.37	9.61	8.76	10.02	1.96	0.46	1.32
Si	26.17	26.73	26.93	24.57	21.55	24.62	4.54	1.03	2.82
S	0.53	0.68	0.33	0.32	0.39	0.23	0.2	0.19	0.54
Cl	0.62	1.26	0.69	1.59	1.55	1.03	2.38	0.45	0.88
K	0.45	0.34	0.2	0.16	0.13	0.16			
Ca	1.79	3.47	2.33	1.72	1.6	1.27	0.55	1.64	3.04
Ti	0.21				0.3				0.29
Fe	1.49	3.64	2.33	2.23	2.1	2.35	0.64		0.55
Cu	8.83	13.78	11.12	16.18	24.57	15.59	74.08	89.49	76.07
Total	100	100	100	100	100	100	100	100	100

Figure 3-56. *SEM image of LFA2 site 3. The EDS result of LFA2 site 3 is shown in the table.*

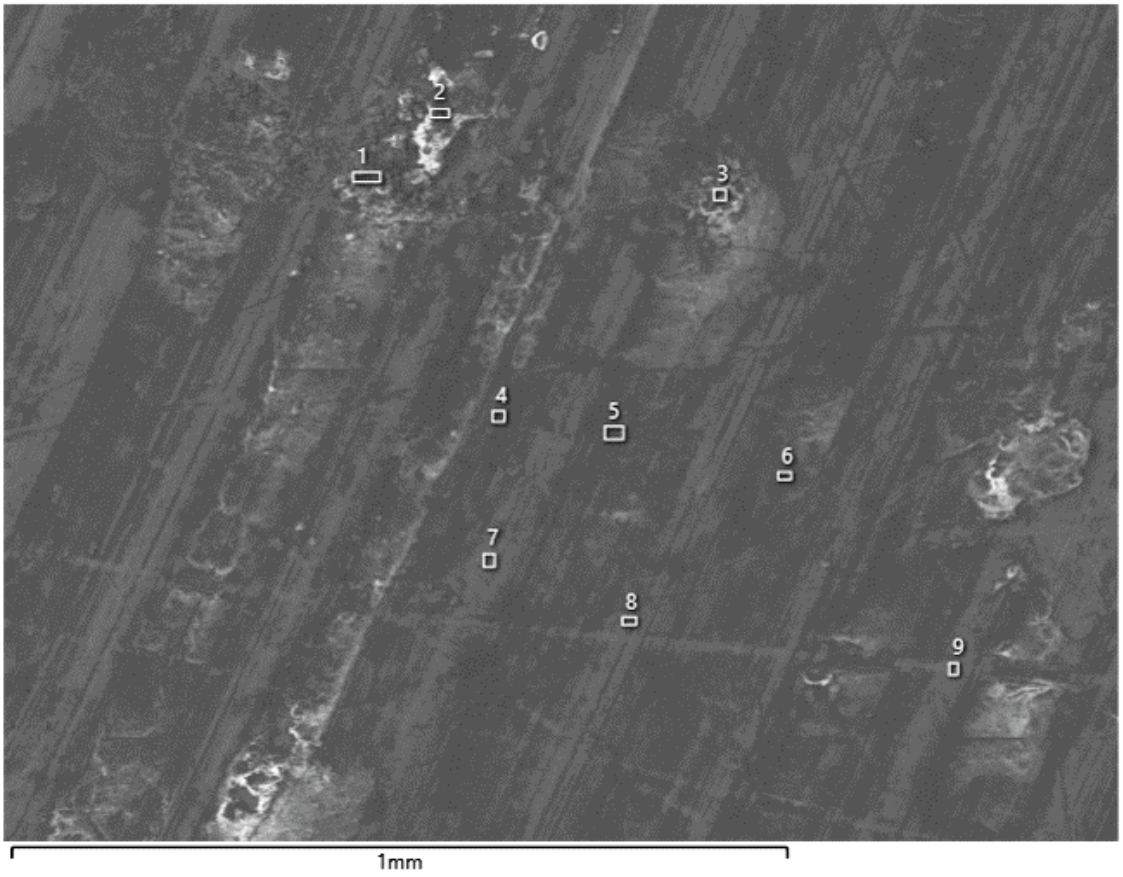

Element (At%)	1	2	3	4	5	6	7	8	9
O	15.16	47.51	43.75	40.23	40.51	36.39	9.72	19.81	8.77
Na	0.3	2.05	1.61	0.97	1.23	1.01			
Mg	0.14	1.65	1.52	1.53	1.66	1.45		1	
Al	1.05	11.01	9.8	7.73	10.05	8.18	1.03	3.97	0.9
Si	2.05	27.16	25.4	18.57	25.17	19.75	2.2	8.86	1.91
S	0.11	0.43	3.86	0.44	0.35	0.3	0.16	0.28	
Cl	0.08	0.21	0.29	0.38	0.63	0.61	1.06	0.65	1.14
K	0.08	0.29	0.47	0.16	0.15	0.12			
Ca	0.37	1.16	1.35	5.15	1.66	1.75	0.65	1.06	0.29
Ti					0.17				
Fe	79.75	3.55	4.46	2.14	2.58	2.3		0.86	
Cu	0.9	4.98	7.49	22.71	15.83	28.14	85.18	63.52	86.98
Total	100	100	100	100	100	100	100	100	100

Figure 3-57. *SEM image of LFA2 site 4. The EDS result of LFA2 site 4 is shown in the table.*

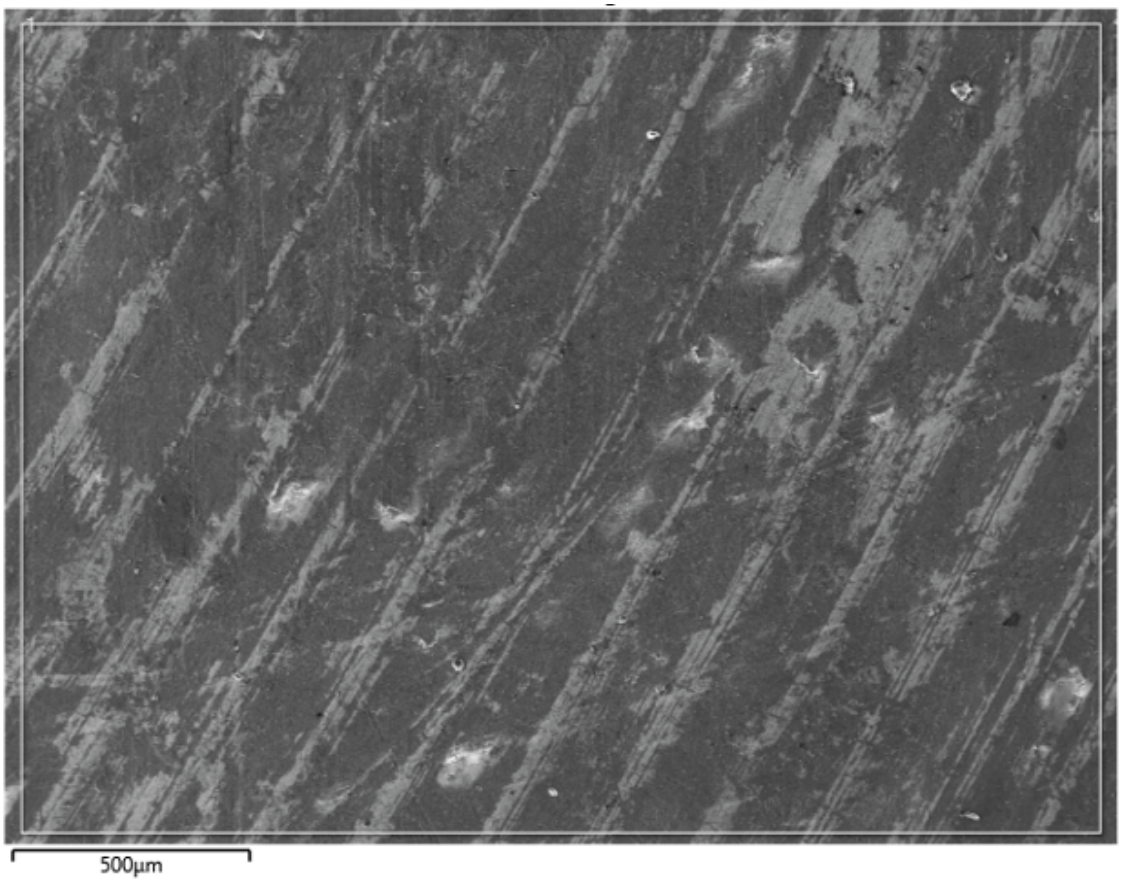

Element (At%)	1
O	58.04
Na	1.47
Mg	1.45
Al	7.43
Si	17.22
S	0.27
Cl	0.52
Ca	1.1
Fe	0.88
Cu	11.53
In	0.08
Total	100

Figure 3-58. *SEM image of LFA2 site 1. The EDS result of LFA2 site 1 is shown in the table. EDS over larger area.*

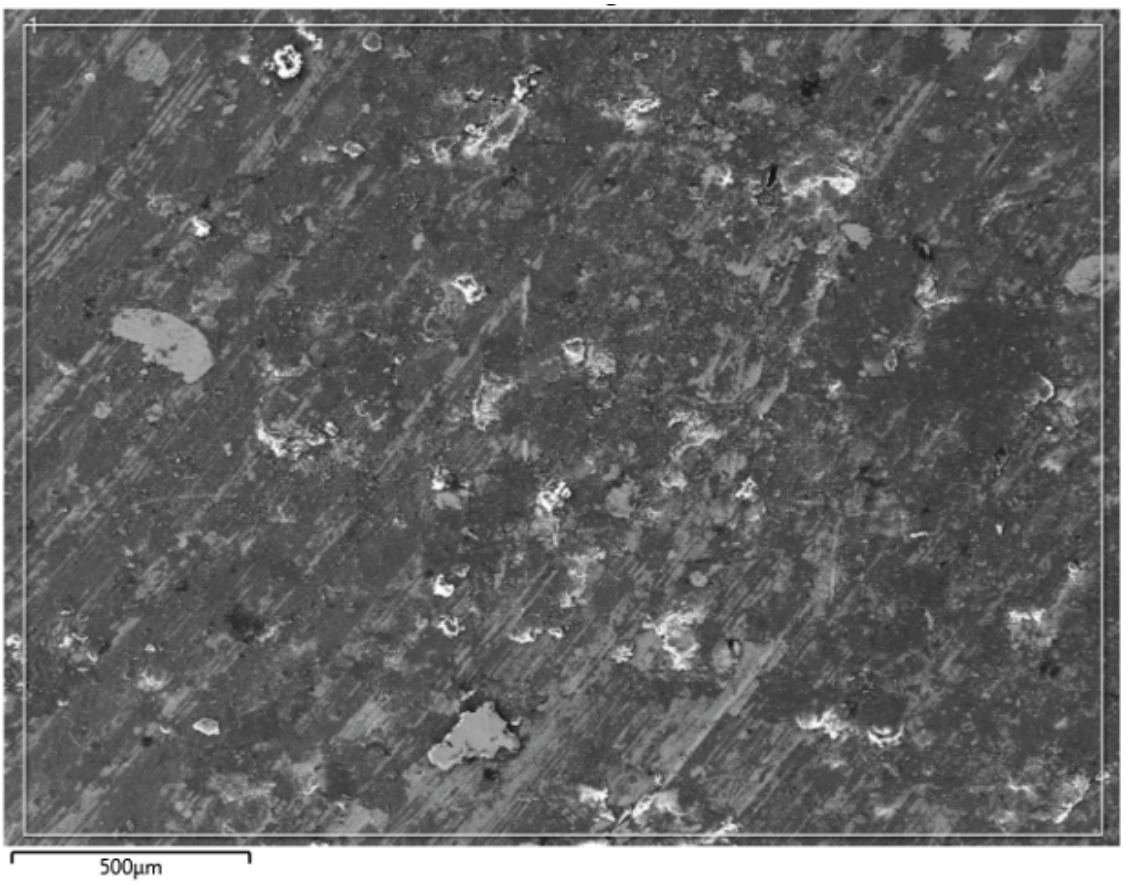

Element (At%)	1
O	55.43
Na	1.8
Mg	1.45
Al	7.59
Si	17.14
S	0.55
Cl	0.36
K	0.19
Ca	1.56
Ti	0.15
Fe	2.19
Cu	11.58
Total	100

Figure 3-59. *SEM image of LFA2 site 2. The EDS result of LFA2 site 2 is shown in the table. EDS over larger area.*

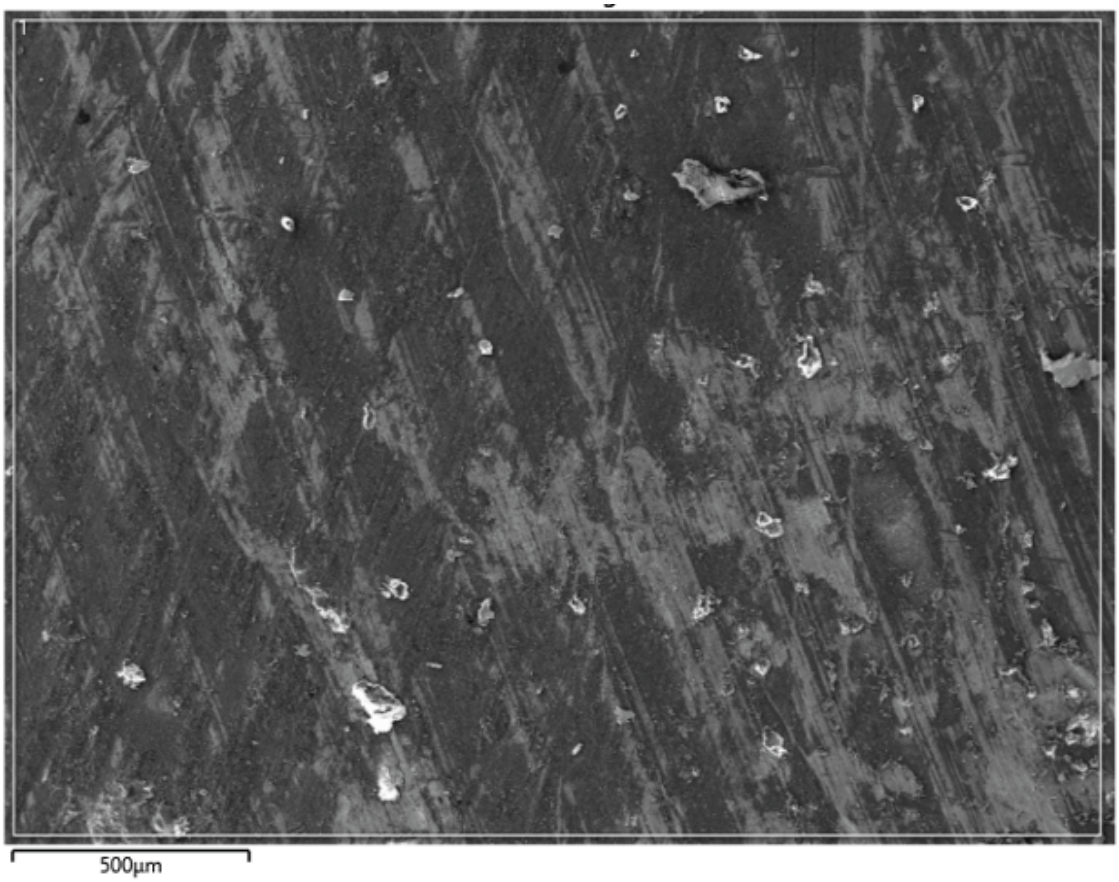

Element (At%)	1
O	54.35
Na	1.44
Mg	1.46
Al	7.42
Si	17.11
S	0.38
Cl	0.69
K	0.12
Ca	1.22
Fe	0.83
Cu	14.98
Total	100

Figure 3-60. *SEM image of LFA2 site 3. The EDS result of LFA2 site 3 is shown in the table. EDS over larger area.*

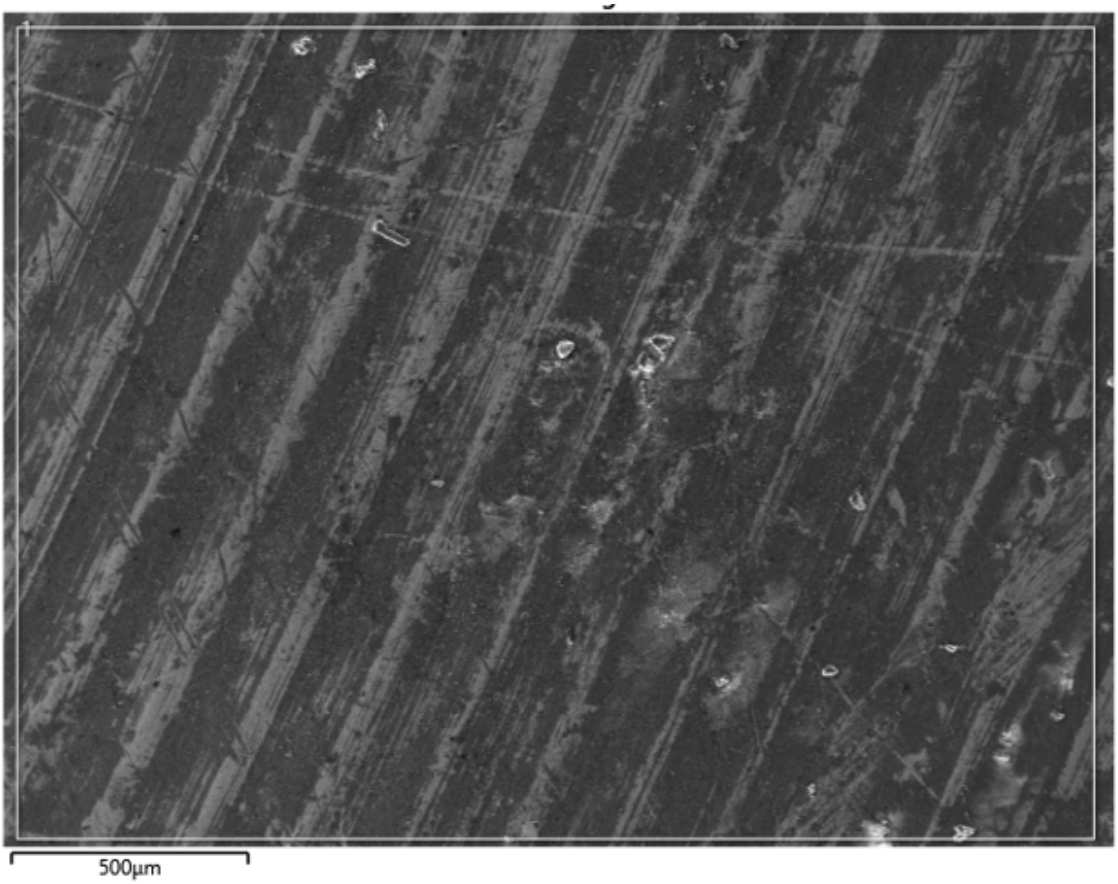

Element (At%)	1
O	55.53
Na	1.49
Mg	1.45
Al	7.39
Si	16.92
S	0.31
Cl	0.5
Ca	1.23
Fe	0.81
Cu	14.35
Total	100

Figure 3-61. *SEM image of LFA2 site 4. The EDS result of LFA2 site 4 is shown in the table. EDS over larger area.*

XRD

Corrosion products were analyzed in the XRD on the sample coupon surfaces. Small peaks of cuprite could be found at an angle of 36.5 2θ which can be seen in Figure 3-62.

FTIR/IRRAS

IRRAS measurements were made on the LFA2 coupon sites and their corresponding IR-spectra can be seen in Figure 3-63. The cuprite peak around 630 cm^{-1} is less visible for LFA2 than for PC901. Malachite double peaks around 1 300–1 600 cm^{-1} are less visible for LFA2 than the other filter housings. The peaks at 1 000 cm^{-1}, 3 600 cm^{-1}, and double peaks at 500–600 cm^{-1} indicate bentonite. Several sites for LFA2 show a distinct peak at 1 100 cm^{-1} indicating the presence of sulfate mineral (e.g. $CaSO_4$).

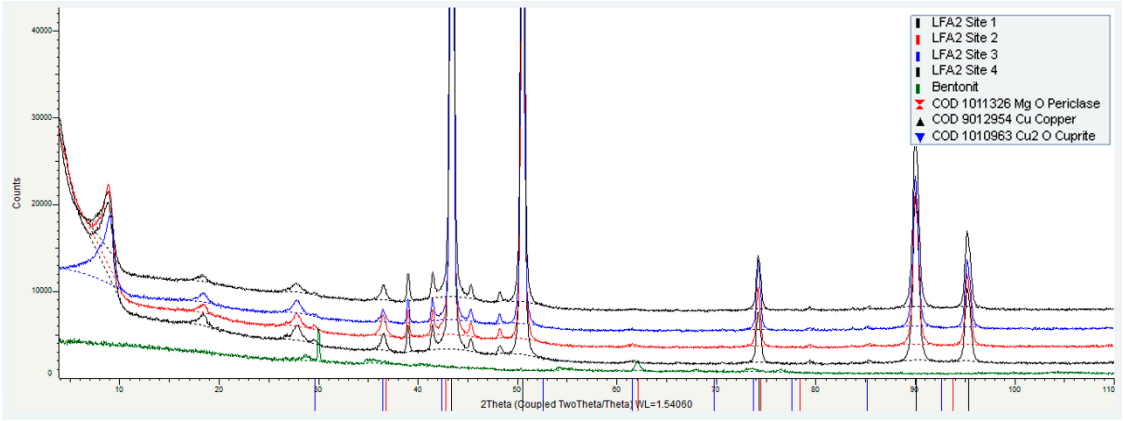

Figure 3-62. *XRD diffractograms obtained from the surface of LFA2.*

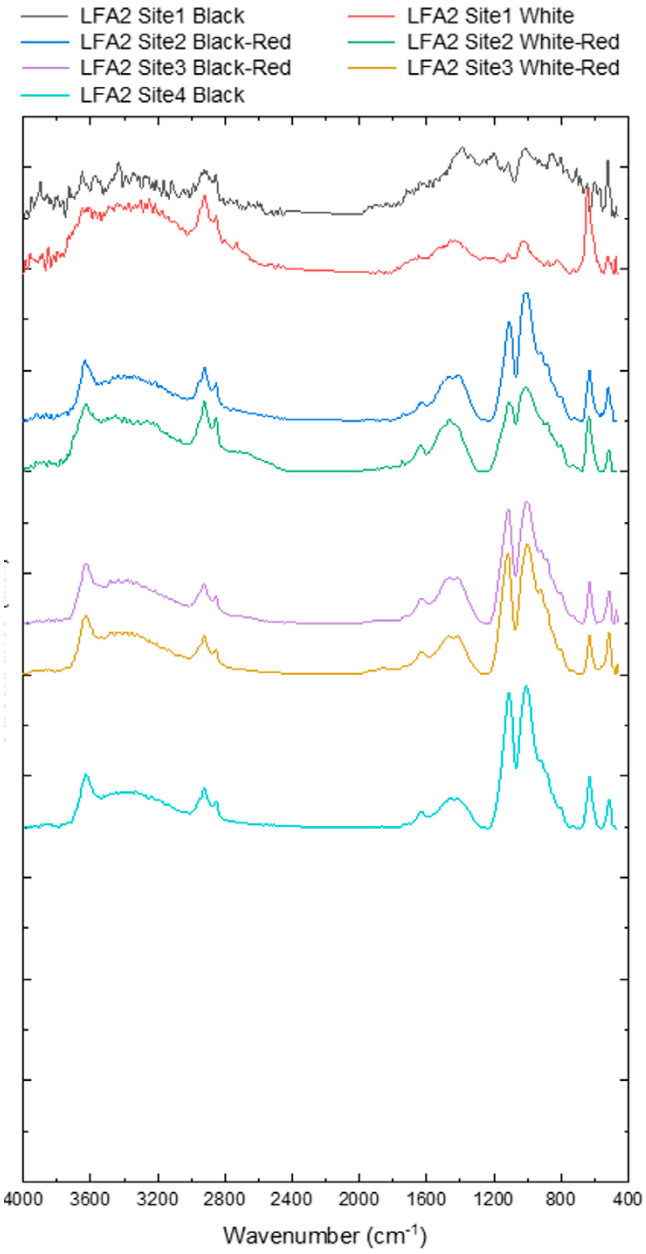

Figure 3-63. *Infrared spectra from FTIR/IRRAS measurement on surface of sample LFA2.*

3.4.2 Cross section analysis

SEM/EDS

The cross section samples cut in half, cast into epoxy resin while mounted surface to surface, polished and analysed with SEM/EDS. Figures 3-64–3-65 and corresponding tables were analysed after dry grinding. Figures 3-66–3-70 were analysed after diamond polishing. The cross section images showed that the surfaces in general had a machined appearance with no clear signs of localised corrosion. The SEM images show a thin oxide layer between 1 and 5 µm, which can be noted in some cases to be rather porous (Figure 3-66). In the right-hand side Figures 3-69–3-70, a porous films can be seen, similar to the porous oxide observed in Figure 3-44. The EDS result show signs of sulfur being present in the cross section of one sample with a tendency to slightly enhanced levels farther out on the oxide layer (Figure 3-66). Since this trend is also seen for calcium the most likely source is precipitation of $CaSO_4$ from the bentonite clay. The detection of ca 20 at% silicon and 9 at% aluminium suggests that the adherent layer in Figure 3-65 is bentonite clay.

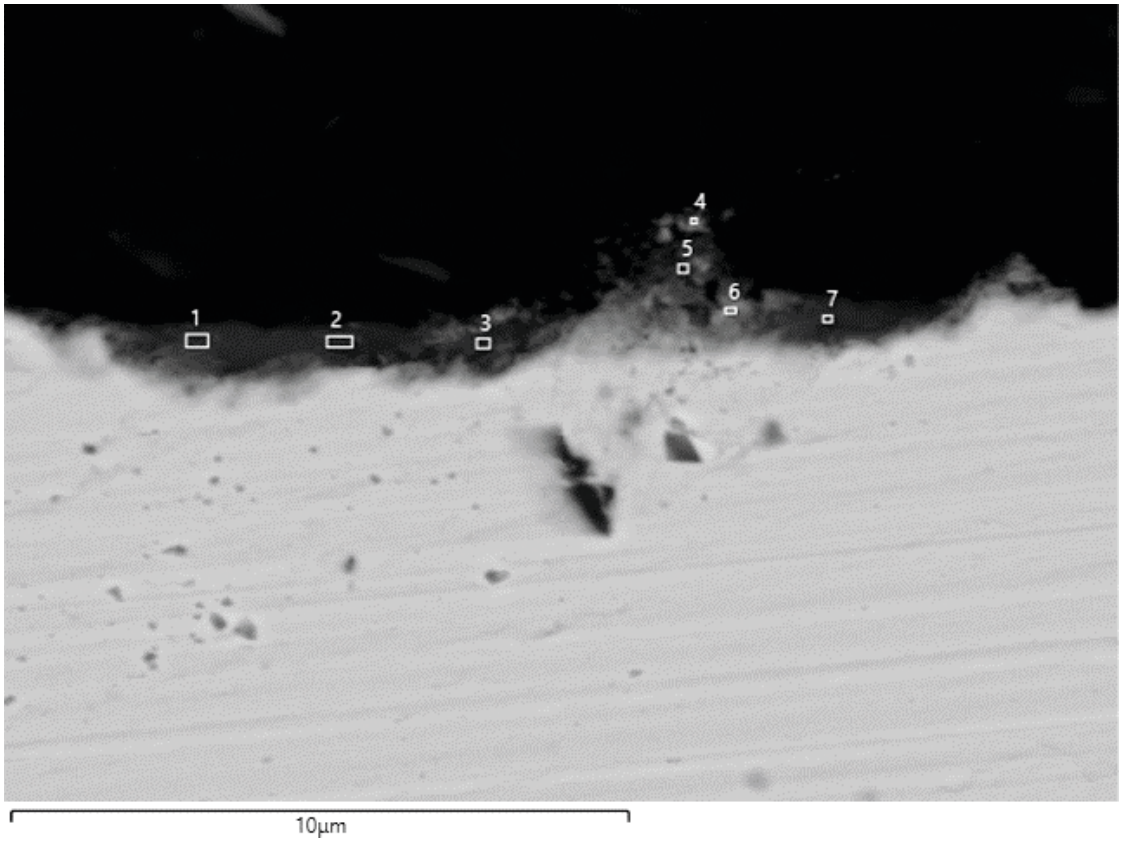

Element (At%)	1	2	3	4	5	6	7
O	37.12	36.13	34.84	12.47	14.22	18.38	38.9
Na	0.7	0.99					0.68
Mg	1.74	1.74	1.46	1.01	1.33	1.4	1.94
Al	10.64	10.34	9.69	7.08	6.59	7.07	10.32
Si	26.91	26.8	26.34	10.28	13.71	17.62	26.54
S	0.28	0.45	0.29		0.27	0.28	0.27
Cl	0.45	0.41	0.36		0.39	0.16	0.31
K	0.31	0.35	0.39	0.57	0.52	0.23	0.54
Ca	1.16	1.41	1.68	0.51	0.96	1.14	1.64
Ti						0.32	
Fe	4.03	3.4	3.9	0.54	1.37	1.75	3.77
Cu	16.67	17.97	21.06	67.53	60.64	51.66	15.09
Total	100	100	100	100	100	100	100

Figure 3-64. *SEM image of the cross section of LFA2. The EDS result of the cross section of LFA2 is shown in the table.*

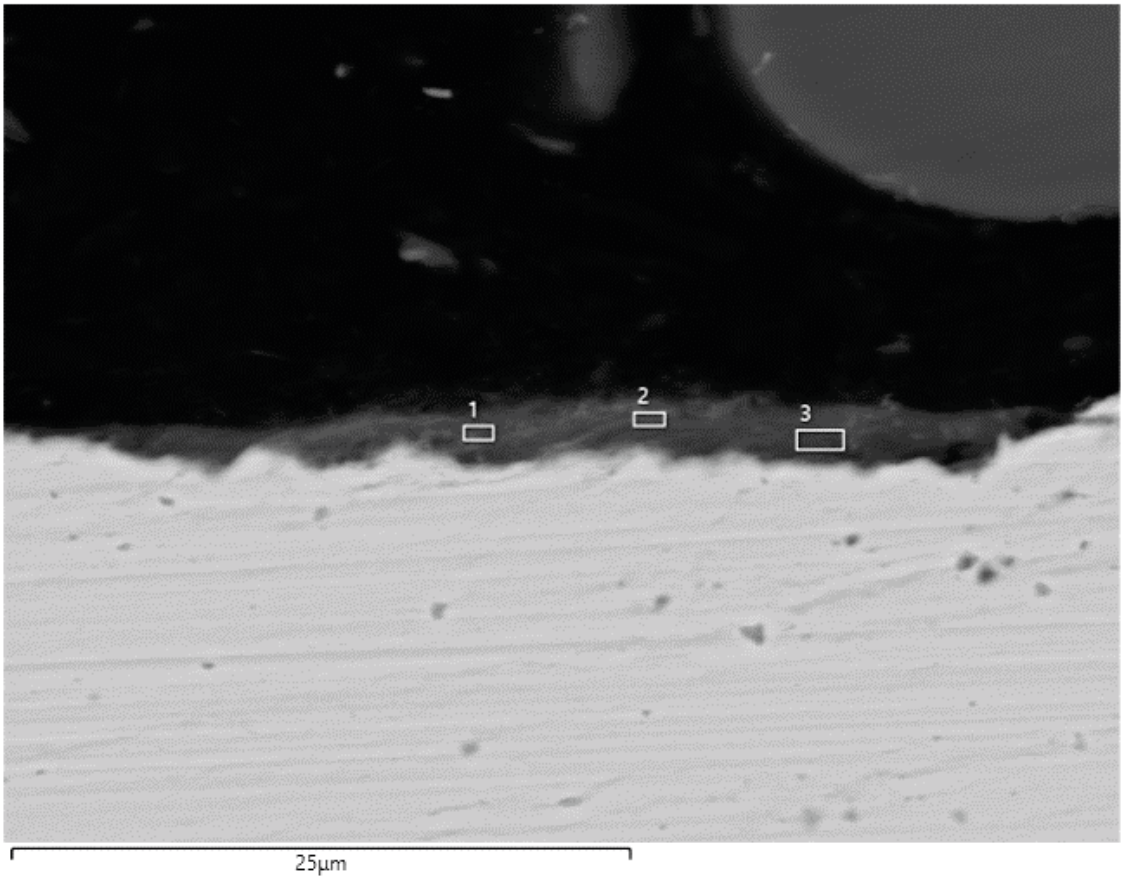

Element (At%)	1	2	3
O	53.74	51.02	54.68
Na			0.83
Mg	1.39	1.56	1.33
Al	8.67	8.89	8.93
Si	21.87	23.19	23.27
S	0.18	0.2	0.65
Cl	0.66	0.71	0.52
K	0.11	0.13	0.15
Ca	0.92	0.52	0.8
Fe	1.19	1.11	1.08
Cu	11.28	12.67	7.76
Total	100	100	100

Figure 3-65. *SEM image of the cross section of LFA2. The EDS result of the cross section of LFA2 is shown in the table.*

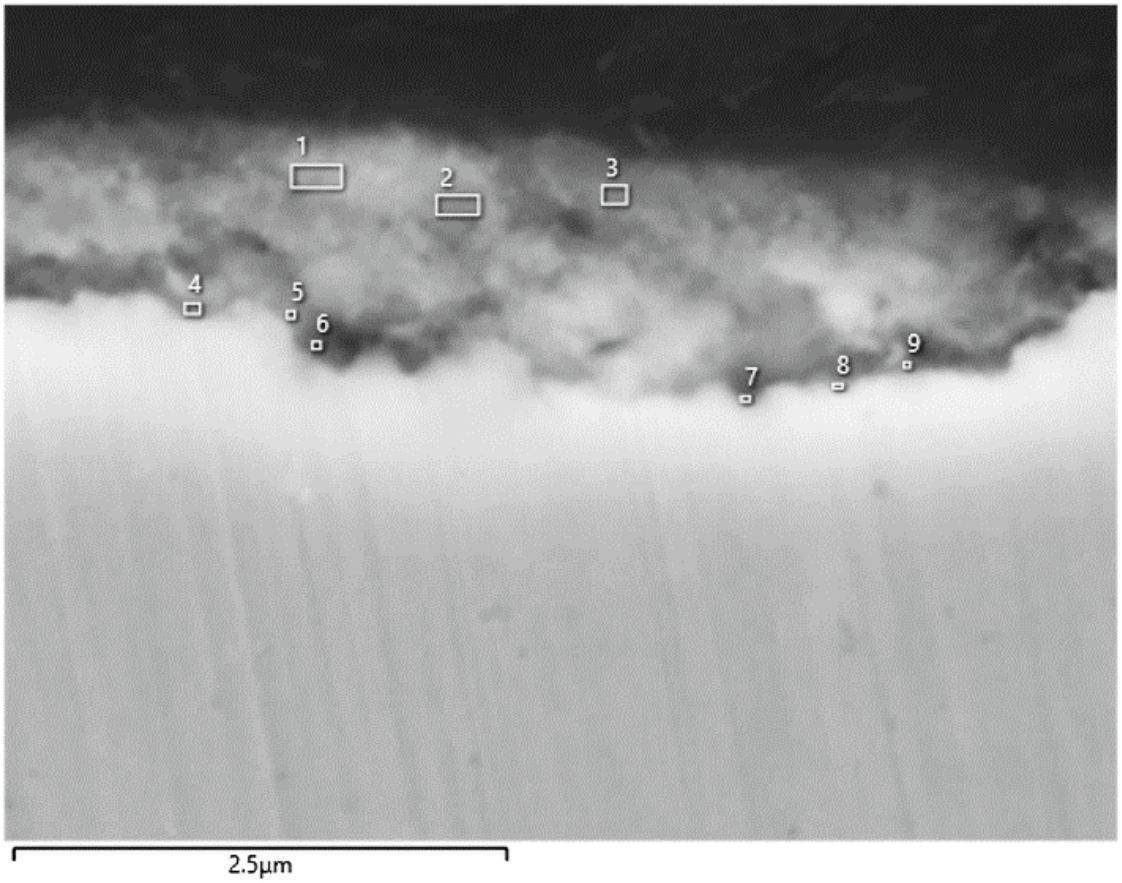

Element (At%)	1	2	3	4	5	6	7	8	9
O	42.46	42.68	41.1	22.5	23.86	17.56	15.11	17.59	16.15
Na	17.92	15.62	18.86	16.13	15.05	14.27			9.23
Mg	0.79	0.62	0.63	0.52					
Al	0.73	0.56	0.69	0.55	0.37	0.33			
Si	1.49	1.42	2.05	0.89	0.9	0.85	0.68	1.02	1.41
S	5.35	5.39	5.72	4.22	4.16	3.9	1.9	2.05	2.42
Cl	1.92	2.1	1.64	4.83	4.31	4.03	1.71	2.19	3.46
Ca	3.02	4.55	3.74	0.98	1.11	0.93	0.75	0.77	0.85
Cu	26.31	27.07	25.57	49.39	50.23	58.13	79.85	76.38	66.47
Total	100	100	100	100	100	100	100	100	100

Figure 3-66. *SEM image of the cross section of LFA2, diamond polished. The EDS result of the cross section of LFA2, diamond polished, is shown in the table.*

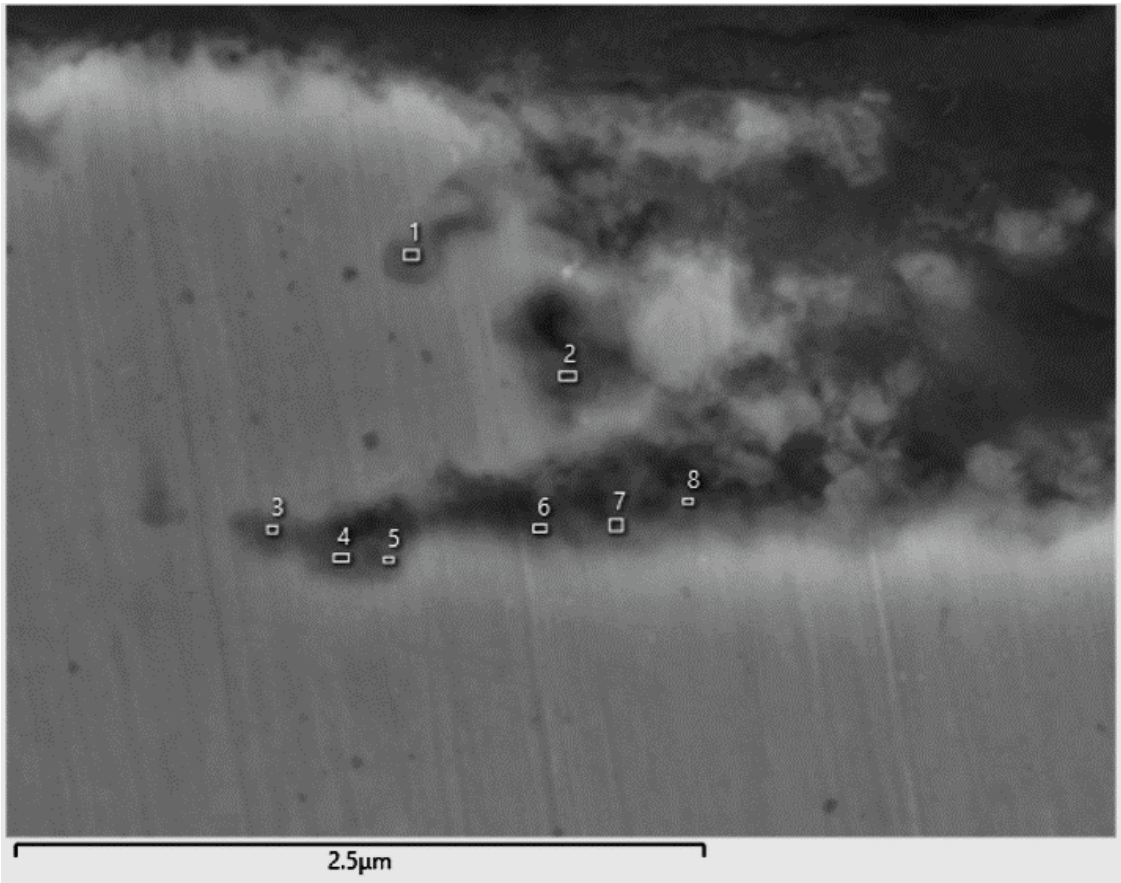

Element (At%)	1	2	3	4	5	6	7	8
O	9.46	20.59	11.08	14.24	15.84	20.42	25.76	29
Mg								1.14
Si	0.18	0.24	0.22	0.15	0.1	0.23	0.26	0.59
S	0.2	0.45		0.12	0.35	0.36	0.4	0.47
Cl		0.58	0.3	0.39	0.25	0.58	0.65	0.61
Ca	0.14	0.27	0.13	0.44	0.42	1.6	1.99	2.73
Fe	0.12	0.14	0.1	0.14	0.16			0.16
Cu	89.9	77.72	88.18	84.51	82.88	76.81	70.94	65.29
Total	100	100	100	100	100	100	100	100

Figure 3-67. *SEM image of the cross section of LFA2, diamond polished. The EDS result of the cross section of LFA2, diamond polished, is shown in the table.*

Figure 3-68. *SEM image overview of cross section at ×140 magnification, LFA2.*

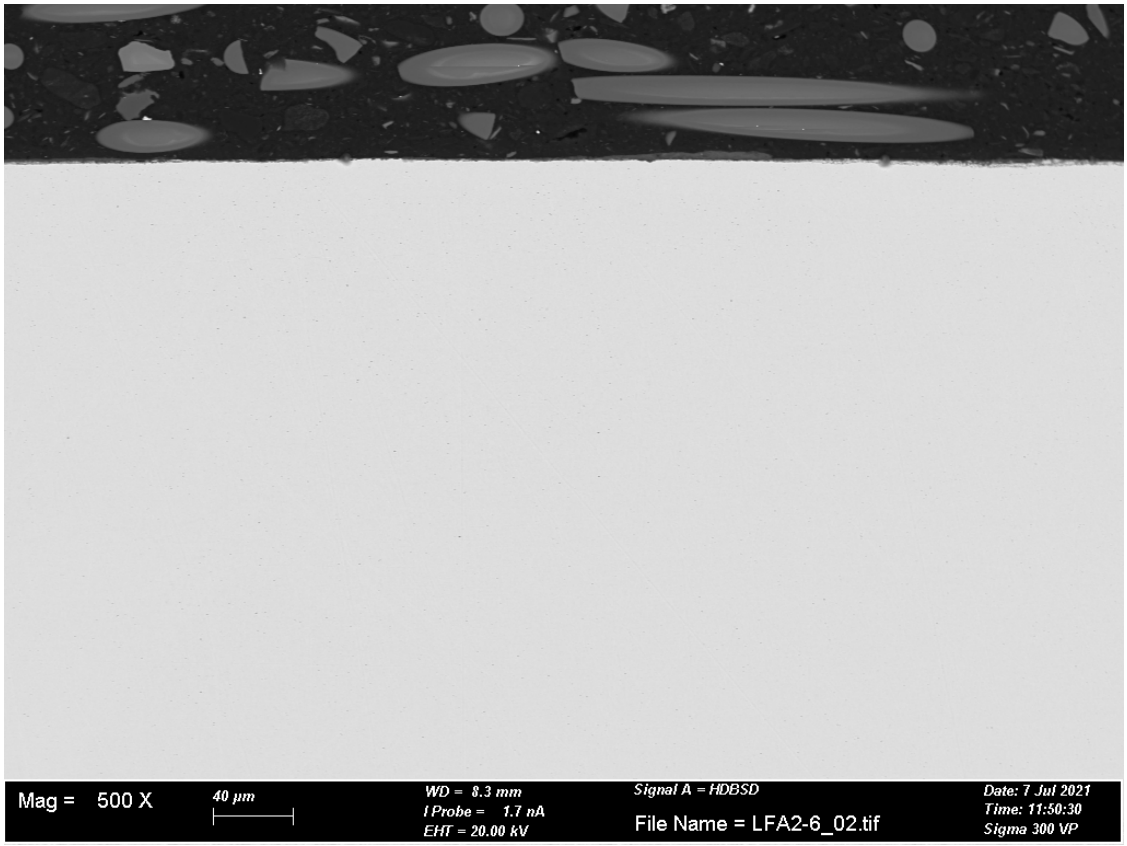

Figure 3-69. *SEM image overview of cross section at ×500 magnification, LFA2.*

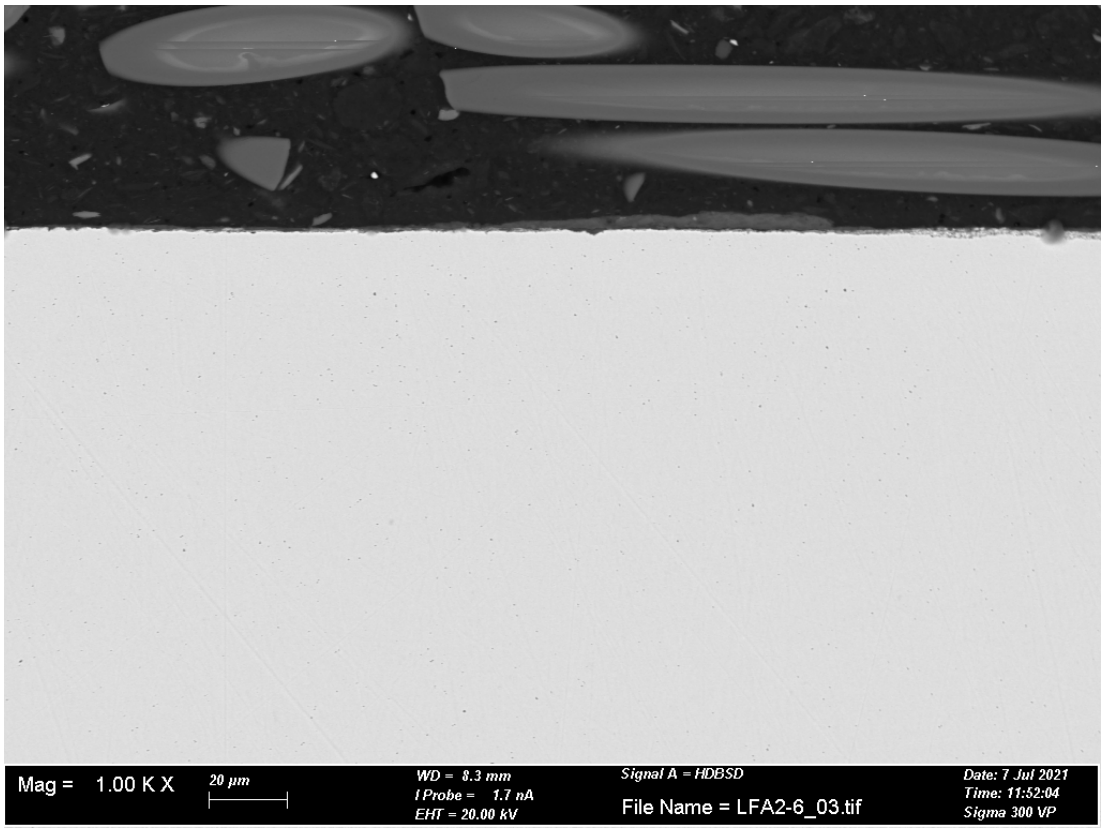

Figure 3-70. *SEM image overview of cross section at ×1 000 magnification, LFA2.*

3.5 UFA4

In Figure 3-71, an overview of filter housing is presented UFA4, with the designated areas for sample coupons marked with a black rectangle. Sample preparation was carried out the same way as PC901 and LFA2. An overview of the four sample coupons for filter housing UFA4 can be seen in Figure 3-72 along with their designated surface analysis sites, marked with red rectangles. A black reticulated pattern was observed on the surface of filter housing UFA4. Analysis sites 1, 3 and 4 were chosen to include the black reticulated pattern in an attempt to determine its composition.

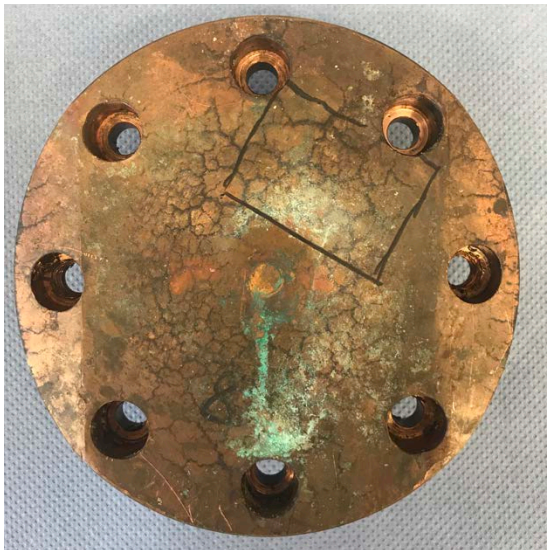

Figure 3-71. *Overview of filter housing UFA4 and the area of which sample coupons for analysis was taken, marked with a black rectangle.*

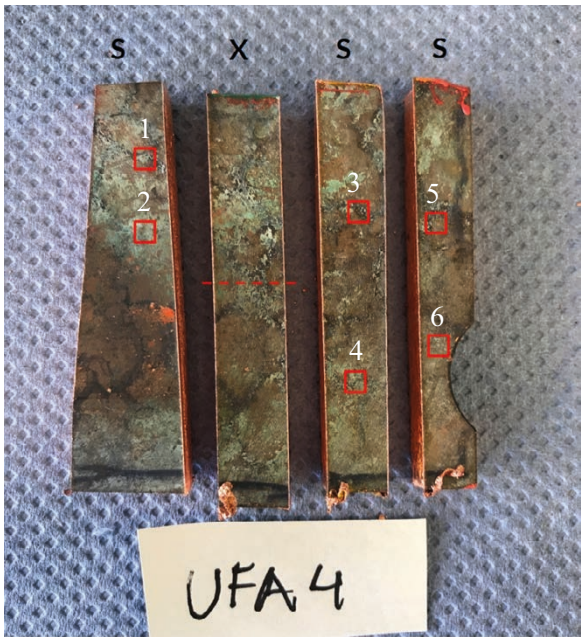

Figure 3-72. *The four test coupons taken from filter housing UFA4. 'S' denotes coupons chosen for surface analysis and 'X' for cross section analysis.*

3.5.1 Surface analysis

SEM/EDS

SEM/EDS analysis was carried out on the surface of the samples. Images showed clear machining marks from manufacturing of the filter housings similar to those of previous filter housings. Elemental analysis on the surface showed mainly copper and oxygen along with the constituents of bentonite. Small amounts of chlorine, iron, and sulfur were also observed for UFA4 which can be seen in Figures 3-73–3-84 and corresponding tables. As noted for the samples above, the level of sulfur was generally found to be low and accompanied with similar levels of calcium and iron, or calcium or iron, which is expected since the bentonite clay contains small amounts of $CaSO_4$ and FeS_2. However, the EDS-analysis of an area of a few mm^2 on site 5 of sample UFA4 shows a few at% more sulfur than what can be explained by $CaSO_4$ and FeS_2 and thus indicating the possible formation of copper sulfide (Figure 3-83). Grey areas appear to be bare copper surface with a thin oxide layer and darker as well as bright white areas appear to be bentonite and corrosion products. The dark reticulated pattern seen in Figures 3-71-3-72 is not clearly distinguishable in the SEM images in Figures 3-73, 3-75–3-76.

Element (At%)	1	2	3	4	5	6	7	8	9
N			14.86						
O	63.72	63.53	56.89	38.26	20.7	39.01	63.72	59.88	60.67
Na	3.17	4.93	4.76	3.26		3.86	2.97	3.51	3.19
Mg	1.52		0.96				1.38	1.78	1.42
Al	7.27	6.64	5.43	0.73		0.82	4.33	5.66	4.9
Si	17.43	15.91	11.08	1.58	1.04	1.51	10.38	13.77	11.64
P						0.21			
S	1.01	1.05	0.79	2.33	1.27	2.97	0.77	1.04	1.15
Cl	0.27	0.75	0.44	0.93	0.72	0.5	0.67	1.06	0.69
K	0.23	0.27	0.13				0.17	0.17	0.23
Ca	0.99	1.31	0.75	0.33	0.41	0.32	6.21	0.46	4.72
Ti	0.19	0.22	0.11						
Fe	0.43	0.54					0.52	0.64	0.69
Cu	3.76	4.86	3.8	52.59	75.87	50.81	8.86	12.03	10.69
Total	100	100	100	100	100	100	100	100	100

Figure 3-73. *SEM image of UFA4 site 1. The EDS result of UFA4 site 1 is shown in the table.*

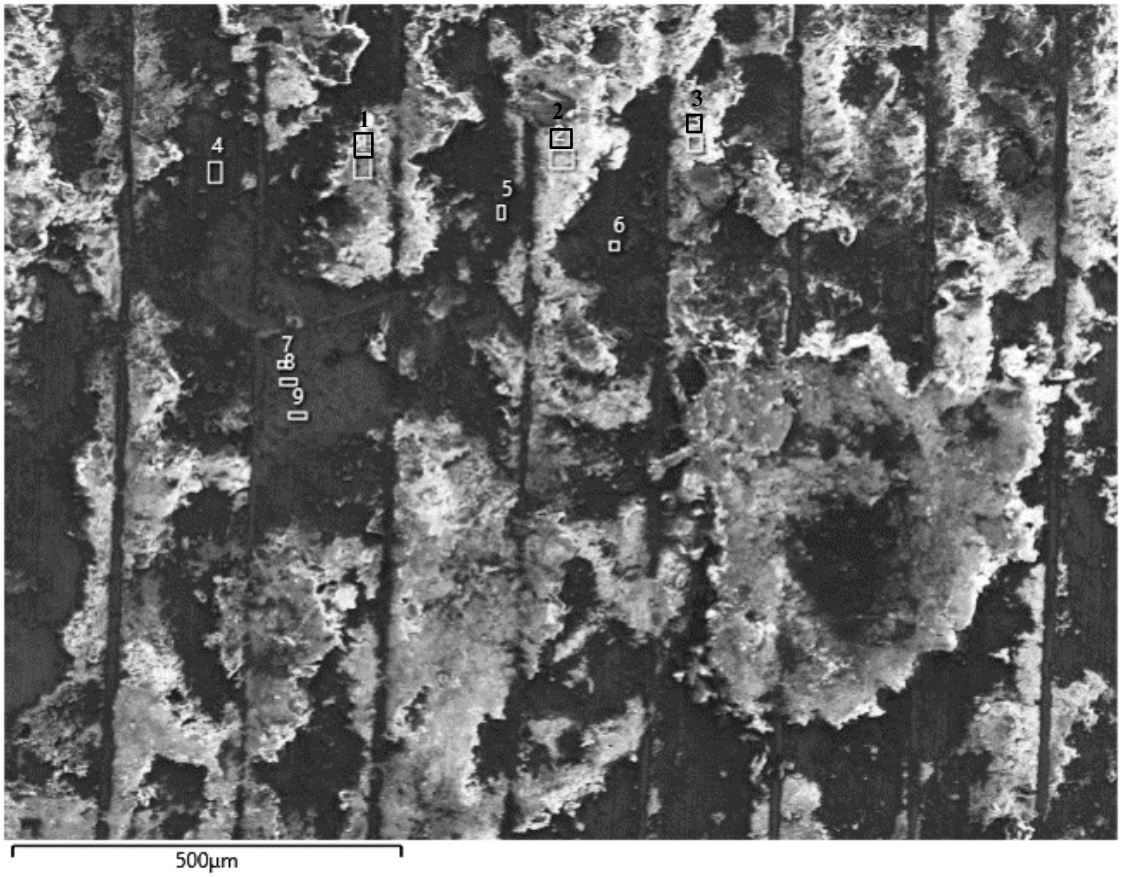

Element (At%)	1	2	3	4	5	6	7	8	9
O	59.84	61.44	63.44	51.8	57.52	54.21	20.43	20.81	22.45
Na	1.03	4.87	5.67	3.15	2.36	3.04			
Mg	0.87			0.9					
Al	8.78	4.11	4.95	4.34	4.59	4.59	0.9	0.84	
Si	3.9	8.81	11.39	9.76	10.59	11.36	1.35	1.54	0.56
S	4.07	2.02	1.68	0.66	0.73	1.12	0.8	1.04	1.32
Cl	0.51	3.96	1.39	2.5	6.84	7.38	0.59	1.16	1.11
K	0.18	0.18	0.35	0.25	0.28	0.33			
Ca	4.3	1.74	1.68	0.62	0.73	1.14	0.66	0.96	1.09
Ti	1.21	0.57	0.74			0.49	1.06	0.39	
Cr	0.32								
Fe	2.51		1.4	0.98	0.82	1.17	1.05	1.67	
Cu	7.31	12.29	7.29	25.02	15.53	15.17	73.15	71.58	73.48
Zn	5.17								
Total	100	100	100	100	100	100	100	100	100

Figure 3-74. *SEM image of UFA4 site 2. The EDS result of UFA4 site 2 is shown in the table.*

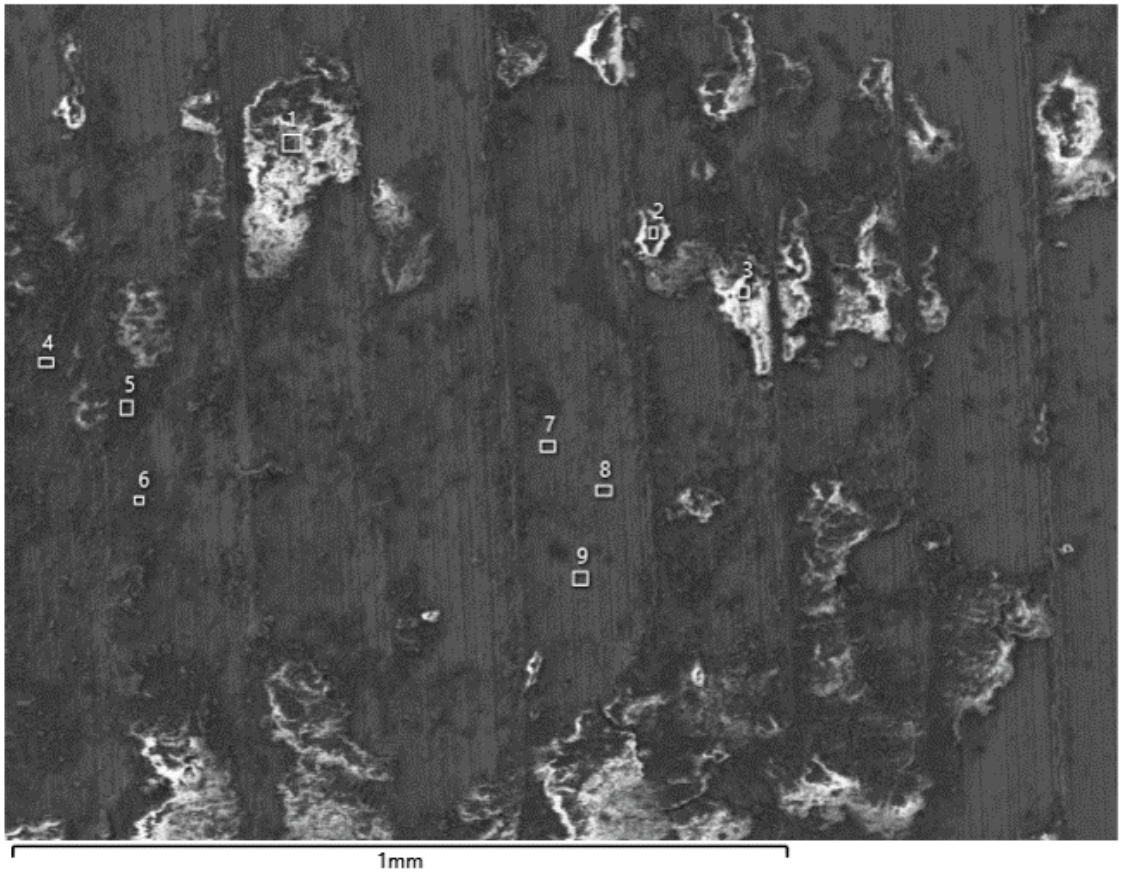

Element (At%)	1	2	3	4	5	6	7	8	9
O	39.2	39.75	49.37	27.83	33.49	20.85	11.82	13.8	13.75
Na	3.08	2.21	2.63	1.06	8.93				
Mg	1.44	1.57	1.5	0.89	0.76	0.68			
Al	6.32	5.06	8.68	3.27	2.97	2.41	0.38	0.76	0.41
Si	16.2	12.34	25.04	7.73	7.4	6.01	0.74	1.55	0.82
P							0.34	0.46	0.48
S	1.76	1.29	0.61	3.5	4.16	1.91	5.24	7.68	7.44
Cl	0.7	1.4	0.19	0.64	0.42	1.76	1.11	0.63	0.66
K	0.26	0.24	0.35	0.18					
Ca	1.61	1.65	1	1.49	0.68	0.85		0.35	0.34
Ti		0.39							
Cr				0.43					
Fe	1.74	1	0.89	9.69	1.33	8.84			
Cu	27.68	33.1	9.74	43.28	39.86	56.69	80.37	74.76	76.09
Total	100	100	100	100	100	100	100	100	100

Figure 3-75. *SEM image of UFA4 site 3. The EDS result of UFA4 site 3 is shown in the table.*

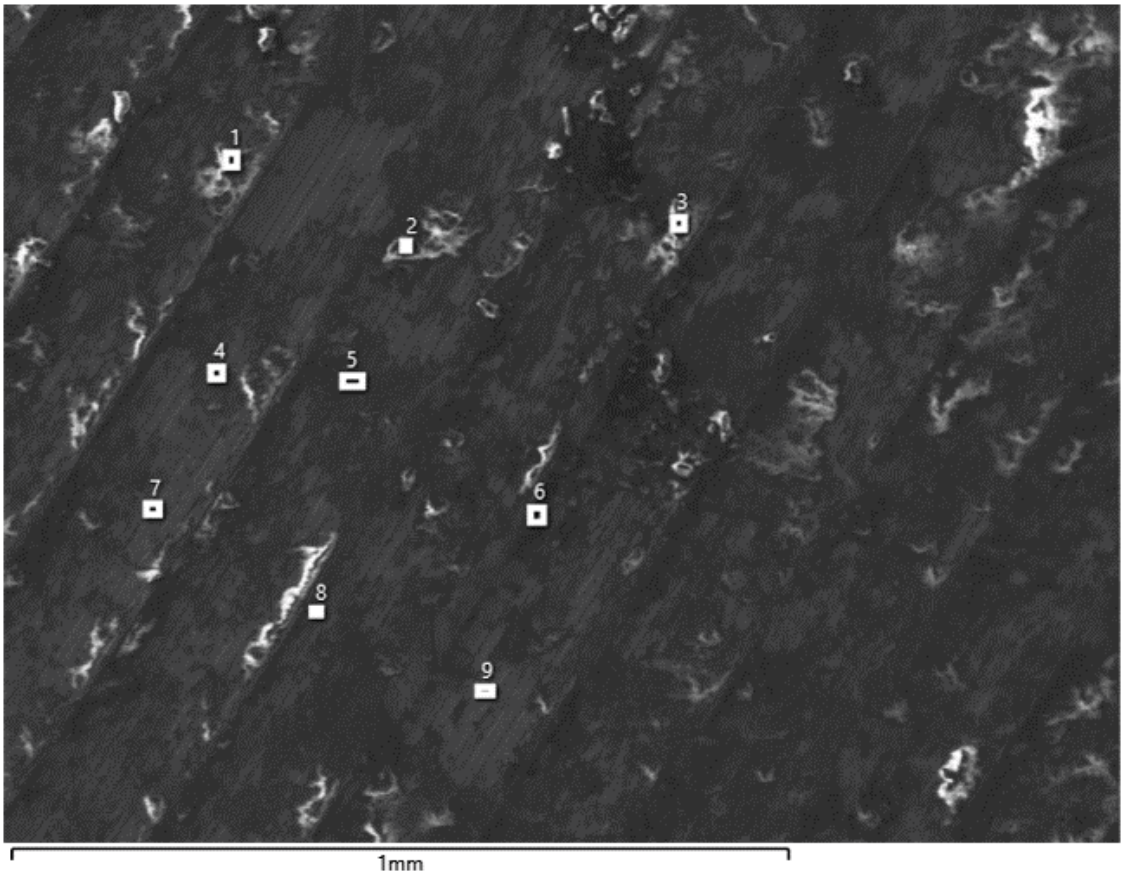

Element (At%)	1	2	3	4	5	6	7	8	9
O	42.44	39.97	41.79	27.23	31.85	30.24	11.39	12.4	11.65
Na	1.81	1.6	1.27	0.62	0.89	0.87			
Mg	1.58	1.5	1.54	0.96		1.07	0.3	0.22	0.41
Al	8.55	7.3	5.19			4.18	0.46	0.7	1.06
Si	20.99	18.44	11.31	6.62	5.99	9.64	0.92	1.43	2.53
P			0.15				0.12		
S	0.85	0.85	5.29	1.12	1.41	1.72	1.08	0.84	0.39
Cl	0.56	0.87	1.67	0.84	1.35	2.06		4.86	0.95
K	0.25	0.27	0.36			0.35			
Ca	1.5	1.08	6.46	1.34	1.59	3.74	2.22	1.23	0.39
Ti	0.55		9.82			4.71			
Fe	1.64	1.85	2.57	0.95	1.08	1.94			
Cu	19.28	26.28	12.57	54.43	51.13	39.46	83.53	78.32	82.61
Br				5.88	4.71				
Total	100	100	100	100	100	100	100	100	100

Figure 3-76. *SEM image of UFA4 site 4. The EDS result of UFA4 site 4 is shown in the table.*

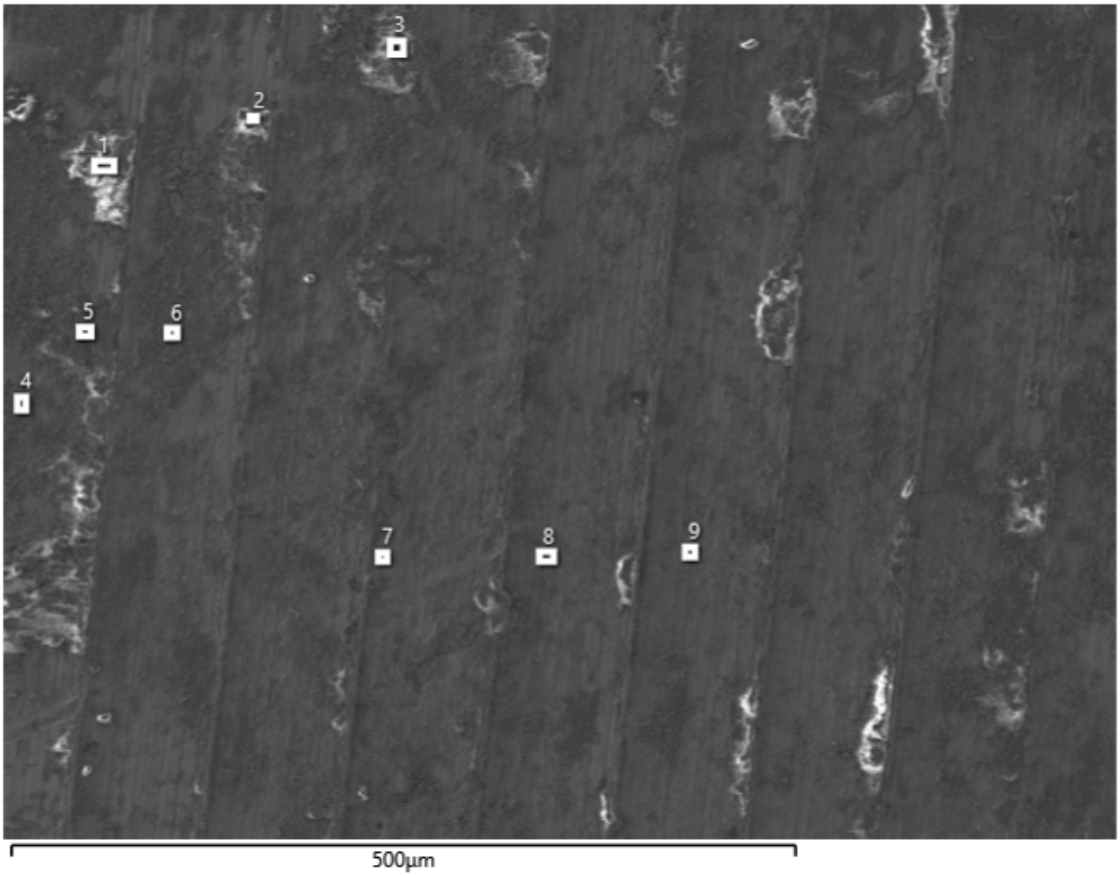

Element (At%)	1	2	3	4	5	6	7	8	9
O	39.49	38.82	39.29	39	40.51	36.89	8.79	18.37	15.98
Na	1.36	1.06	1.48	1.11	1.39	1.25		0.26	
Mg	1.29	0.87	1.51	1.38	1.52	1.23		0.6	0.4
Al	7.28	8.08	6.98	7.5	8.5	6	0.26	2.01	1.22
Si	18.8	22.6	18.23	19.05	22	15.1	0.52	4.56	2.79
P								0.18	0.48
S	1.18	1.09	1.52	1.35	1.47	1.04	1.79	2.13	5.88
Cl	2.44	0.56	0.72	0.95	0.64	1.04	0.28	0.61	0.28
K	0.27	3.98	0.23	0.2	0.27	0.21			
Ca	1.21	0.9	4.12	1.13	1.52	1.77	0.58	0.89	0.45
Ti		0.39							
Fe	1.53	1.58	2.28	2.05	2.53	1.95			
Cu	25.16	20.09	23.66	26.27	19.65	33.53	87.78	70.39	72.52
Total	100	100	100	100	100	100	100	100	100

Figure 3-77. *SEM image of UFA4 site 5. The EDS result of UFA4 site 5 is shown in the table.*

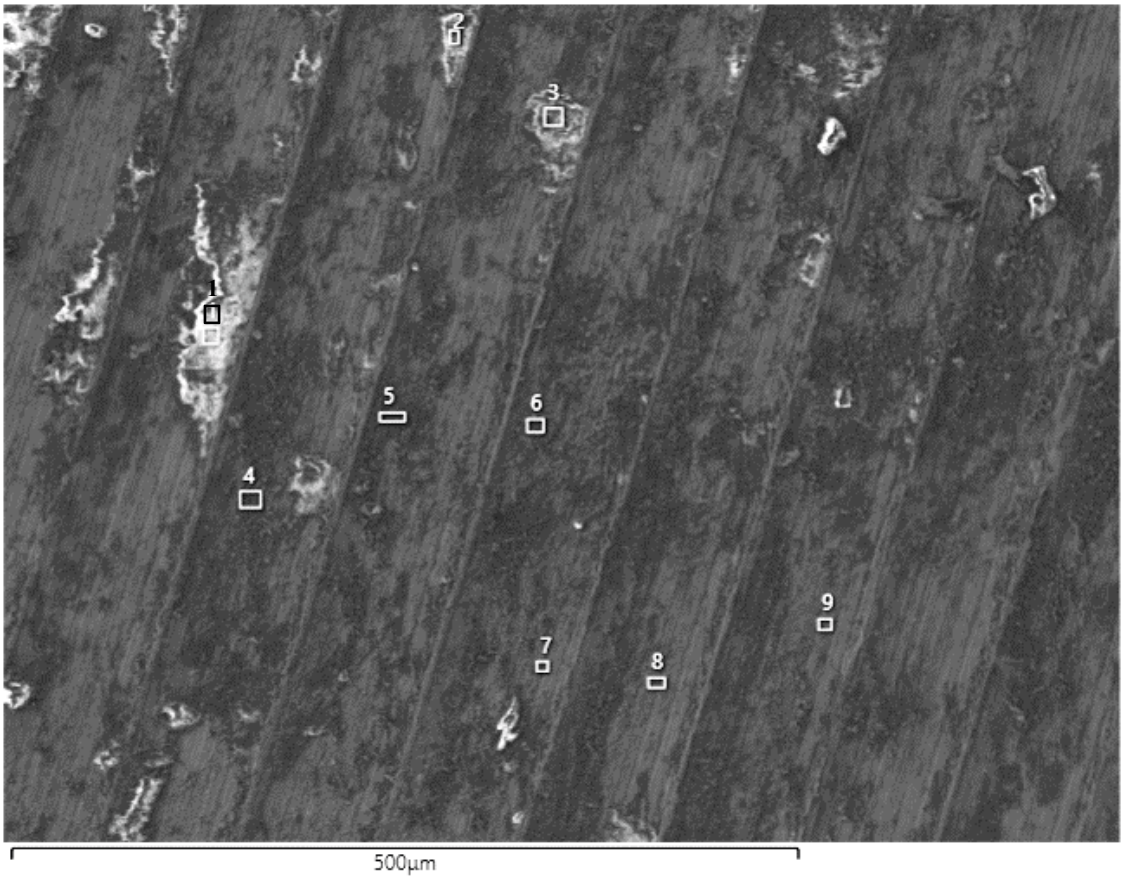

Element (At%)	1	2	3	4	5	6	7	8	9
O	43.45	42.04	42.84	35.85	34.5	31.91	12.81	15.25	10.78
Na	1.57	1.37	1.75	0.63					
Mg	2.05	2.16	1.95	1.49	1.39	1.18	0.44	0.57	
Al	9.42	8.94	9.39	6.42		3.63	1.26	1.68	0.48
Si	24.02	22.59	23.33	16.42	15.43	9.39	2.89	3.97	1.17
P						0.3	0.22	0.23	0.19
S	0.81	1.14	0.83	1.69	1.34	3.66	2.78	3.69	2.71
Cl	0.32	0.41	0.38	0.47	0.43	0.42	0.18	0.3	0.24
K	0.19	0.17	0.25	0.3	0.23				
Ca	0.75	1.05	0.85	4.56	4.84	9.83	0.92	0.56	0.54
Fe	1.65	1.68	2	2.97	2.96	1.65		0.95	
Cu	15.76	18.45	16.45	29.2	26.76	38.04	78.5	72.79	83.89
Br					12.12				
Total	100	100	100	100	100	100	100	100	100

Figure 3-78. *SEM image of UFA4 site 6. The EDS result of UFA4 site 6 is shown in the table.*

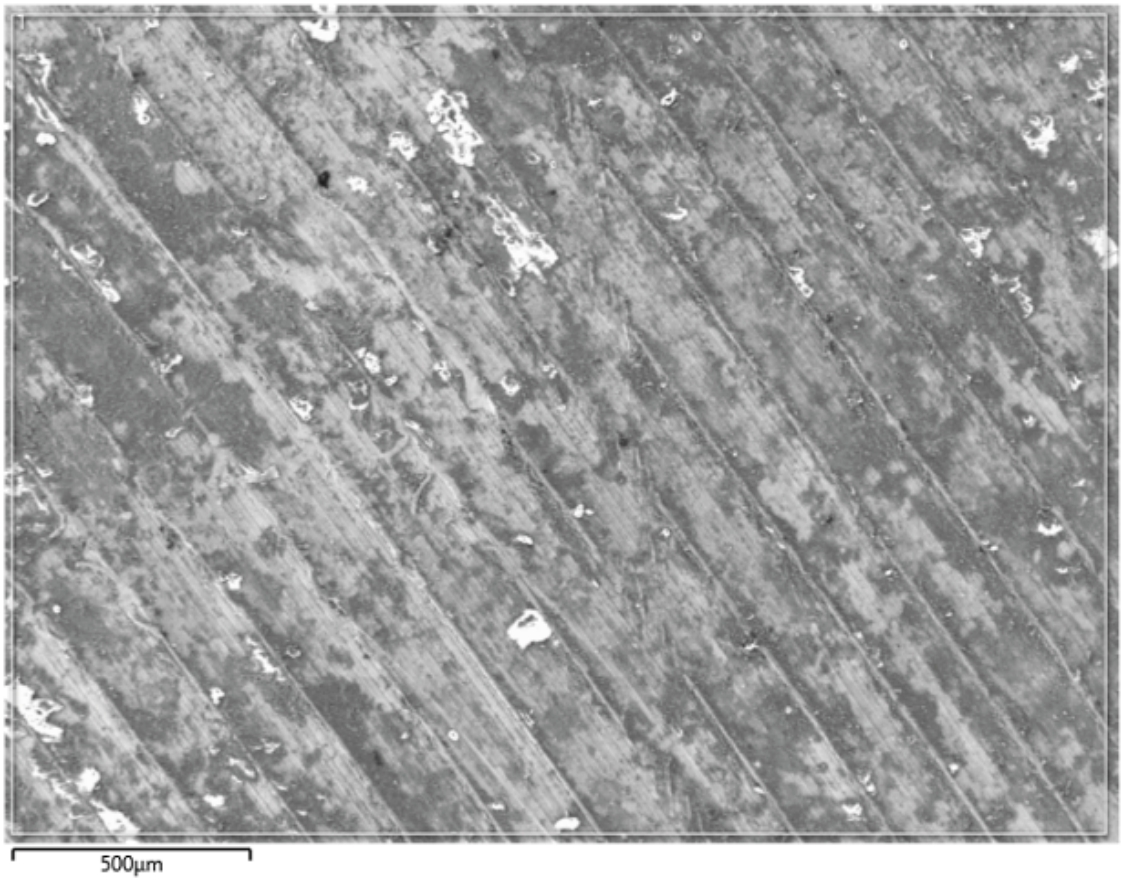

Element (At%)	1
O	50.74
Mg	1.35
Al	4
Si	8.95
S	2.28
Cl	0.98
K	0.19
Ca	1.67
Ti	0.19
Fe	0.92
Cu	28.74
Total	100

Figure 3-79. *SEM image of UFA4 site 1. The EDS result of UFA4 site 1 is shown in the table. EDS over larger area.*

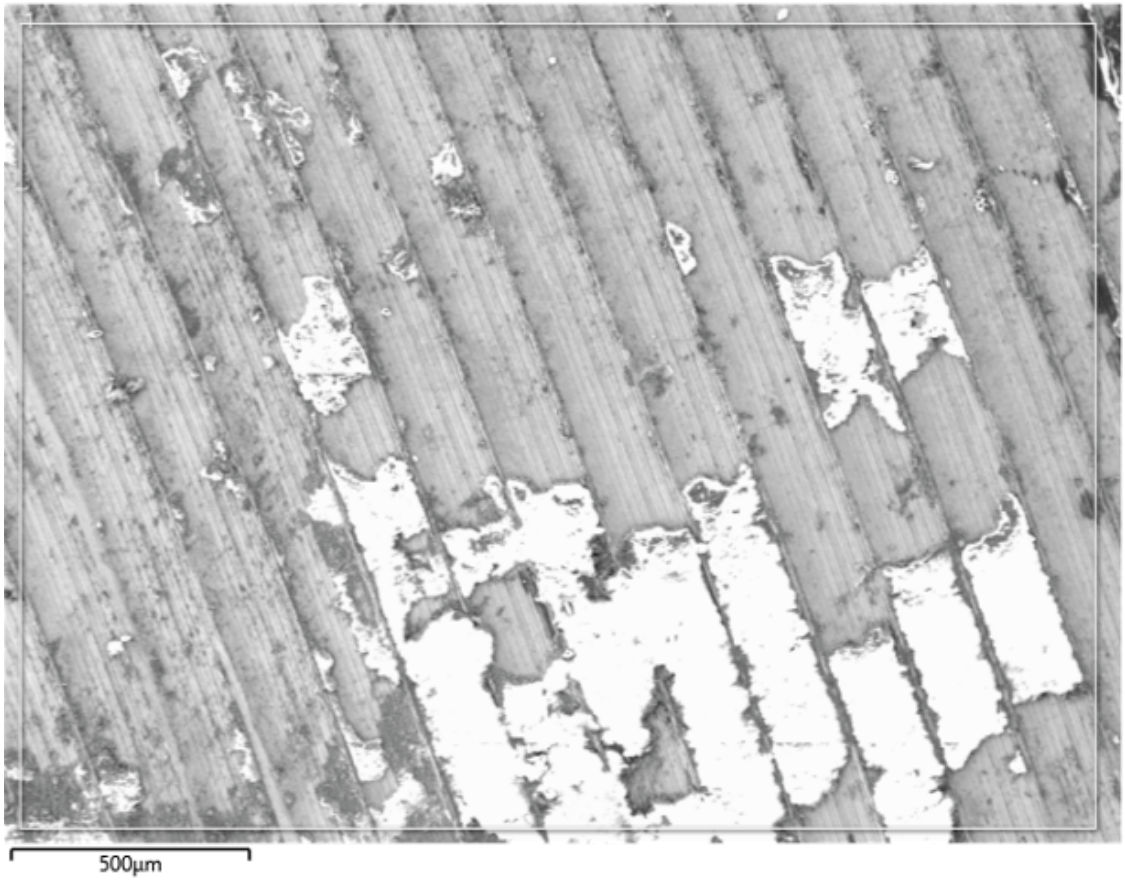

Element (At%)	1
O	40.37
Na	2.5
Mg	1.01
Al	3.68
Si	7.91
S	1.44
Cl	1.16
K	0.15
Ca	1.06
Ti	0.44
Fe	0.47
Cu	39.82
Total	100

Figure 3-80. *SEM image of UFA4 site 2. The EDS result of UFA4 site 2 is shown in the table. EDS over larger area.*

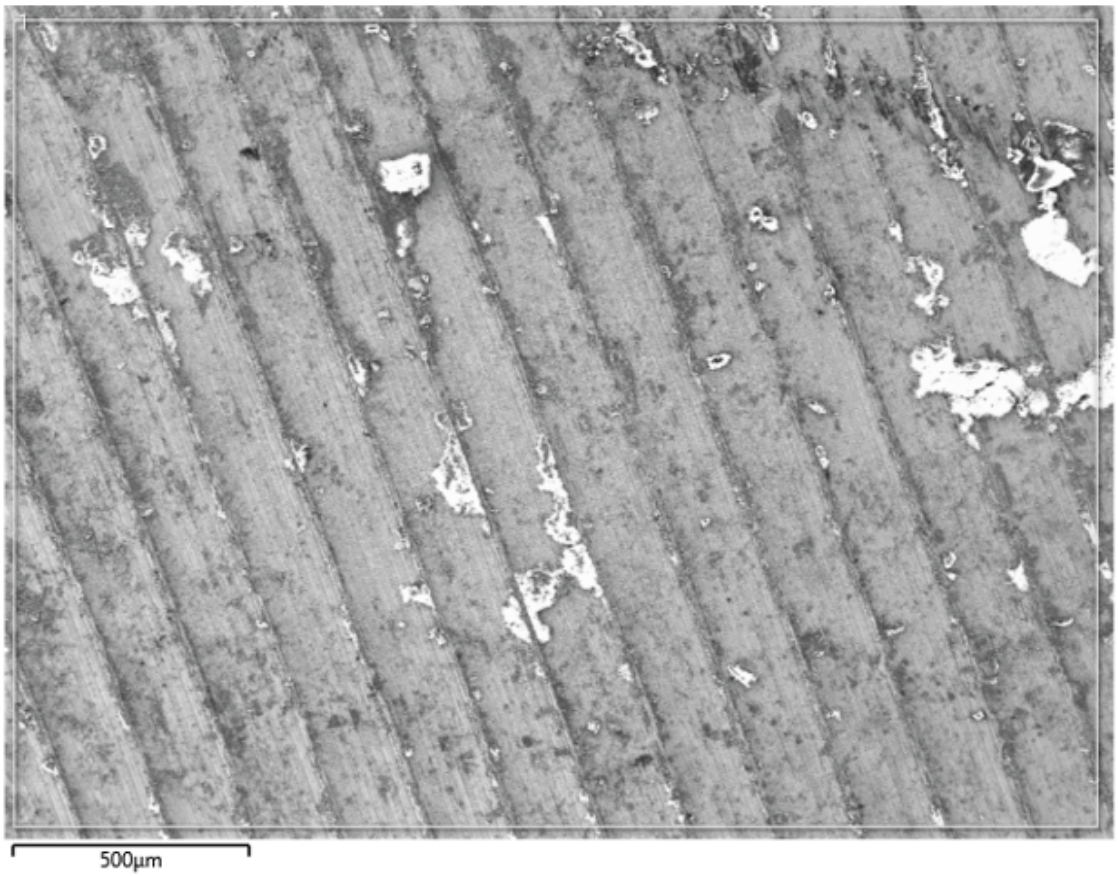

Element (At%)	1
O	40.98
Mg	0.98
Al	2.63
Si	5.76
P	0.12
S	2.04
Cl	1.31
Ca	1.06
Ti	0.28
Fe	0.46
Cu	44.37
Total	100

Figure 3-81. *SEM image of UFA4 site 3. The EDS result of UFA4 site 3 is shown in the table. EDS over larger area.*

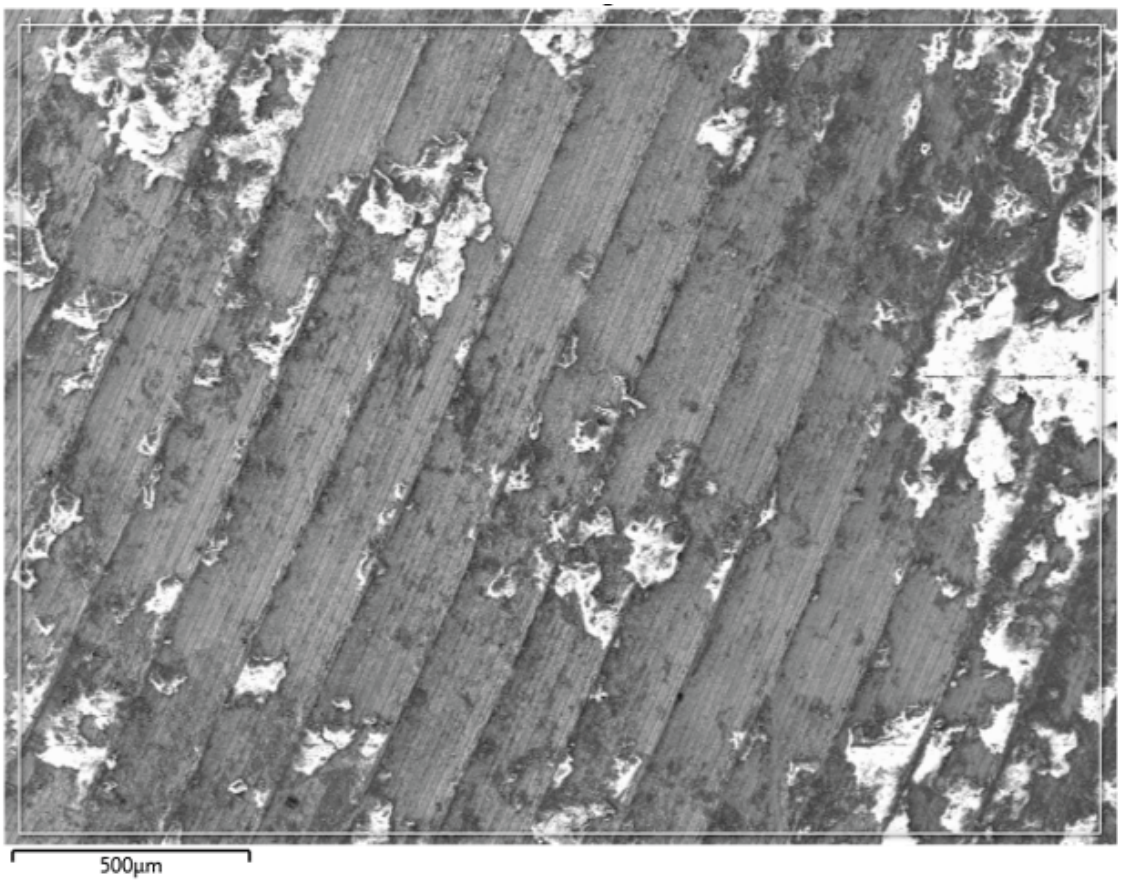

Element (At%)	1
O	49.72
Mg	1.26
Al	4.3
Si	9.56
P	0.11
S	1.96
Cl	0.98
Ca	1.47
Fe	0.64
Cu	30.01
Total	100

Figure 3-82. *SEM image of UFA4 site 4. The EDS result of UFA4 site 4 is shown in the table. EDS over larger area.*

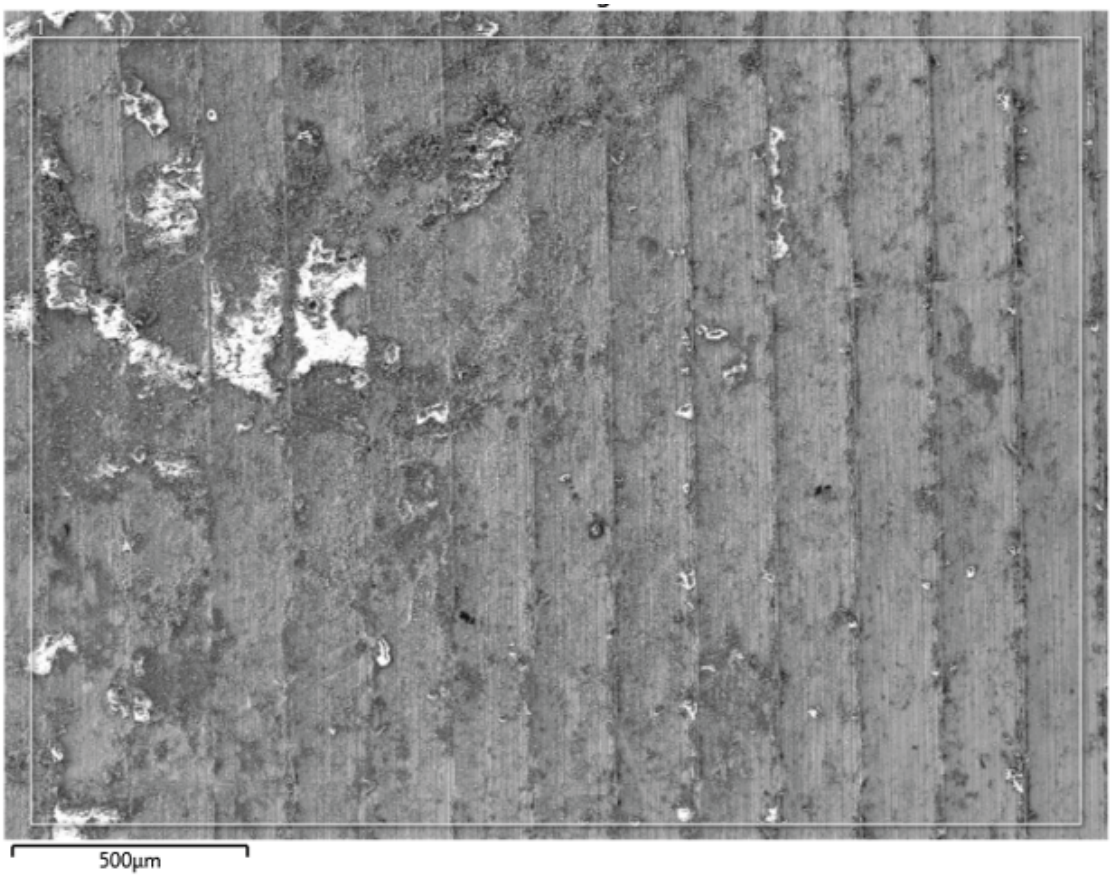

Element (At%)	1
O	47.65
Mg	1.09
Al	2.84
Si	6.46
P	0.3
S	4.25
Cl	0.68
Ca	0.85
Fe	0.53
Cu	35.36
Total	100

Figure 83. *SEM image of UFA4 site 5. The EDS result of UFA4 site 5 is shown in the table. EDS over larger area.*

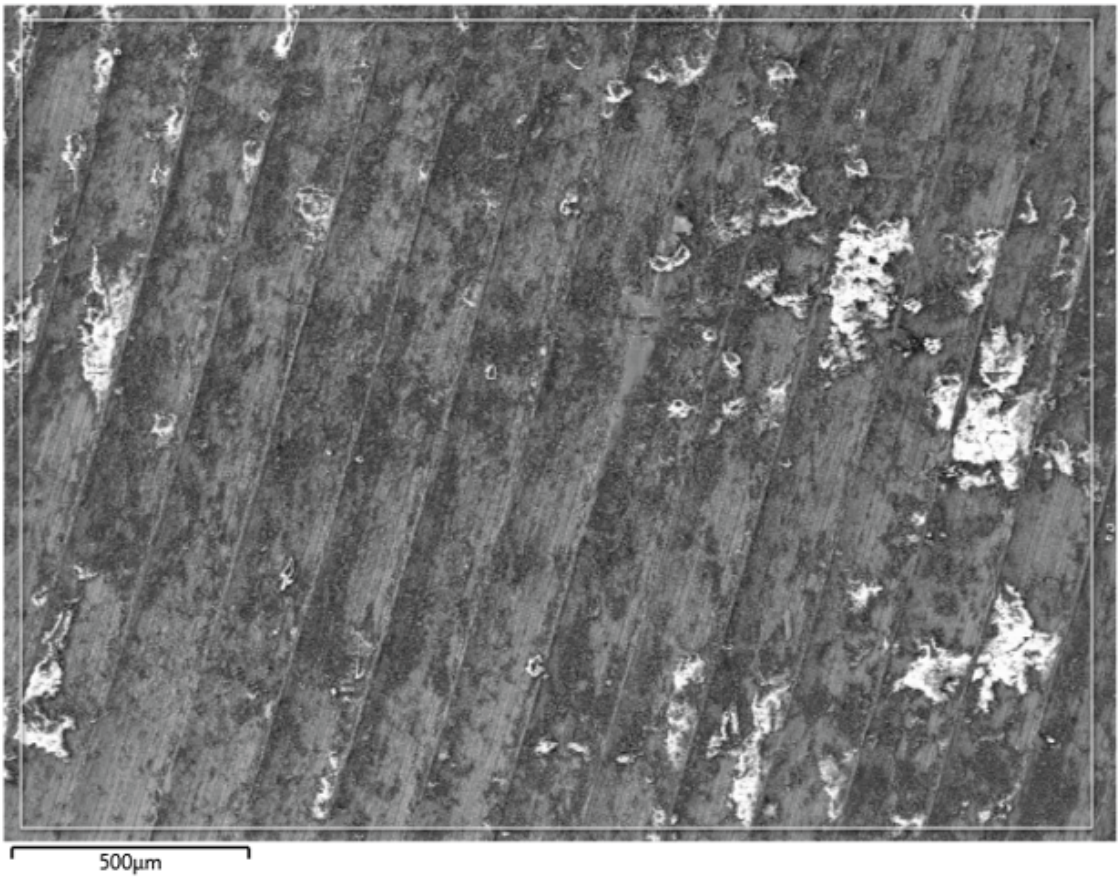

Element (At%)	1
O	51.2
Mg	1.41
Al	5.33
Si	12.33
P	0.15
S	2.23
Cl	0.5
Ca	1.83
Fe	0.92
Cu	24.12
Total	100

Figure 3-84. *SEM image of UFA4 site 6. The EDS result of UFA4 site 6 is shown in the table. EDS over larger area.*

XRD

Corrosion products were analysed in the XRD on the sample coupon surfaces. Small peaks of cuprite could be found at an angle of 36.5 2θ along with peaks originating from metallic copper, which can be seen in Figure 3-85.

FTIR/IRRAS

IRRAS measurements were made on the UFA4 coupon sites and their corresponding IR-spectra can be seen in Figure 3-86. A Peak around 630 cm^{-1} can be seen for a few sites indicating the presence of cuprite. Double peaks around 1 300–1 600 cm^{-1} indicates malachite. Peak at 1 000 cm^{-1}, 3 600 cm^{-1}, and double peaks at 500–600 cm^{-1} indicate bentonite. Site 3 show a peak at 1 100 cm^{-1} which could indicate adsorbed sulphate or precipitated sulphate minerals.

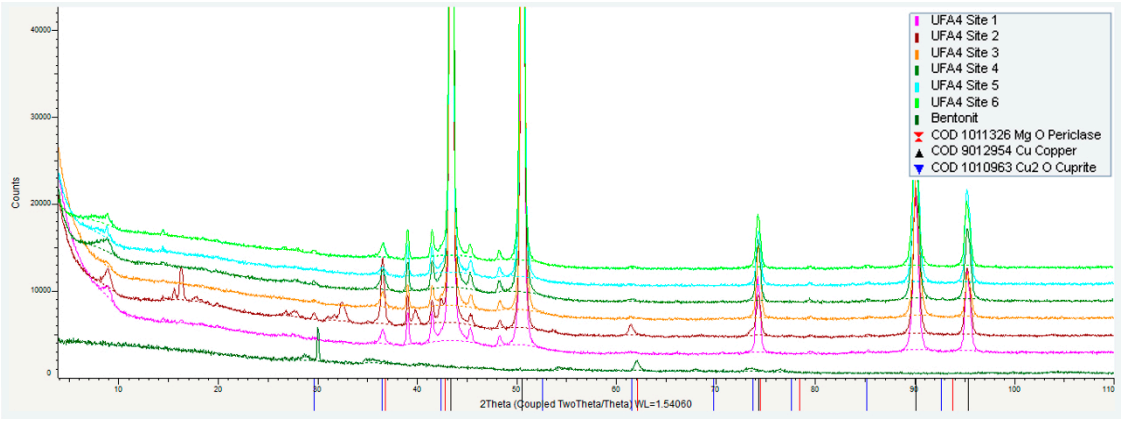

Figure 3-85. *XRD diffractograms obtained from the surface of UFA4.*

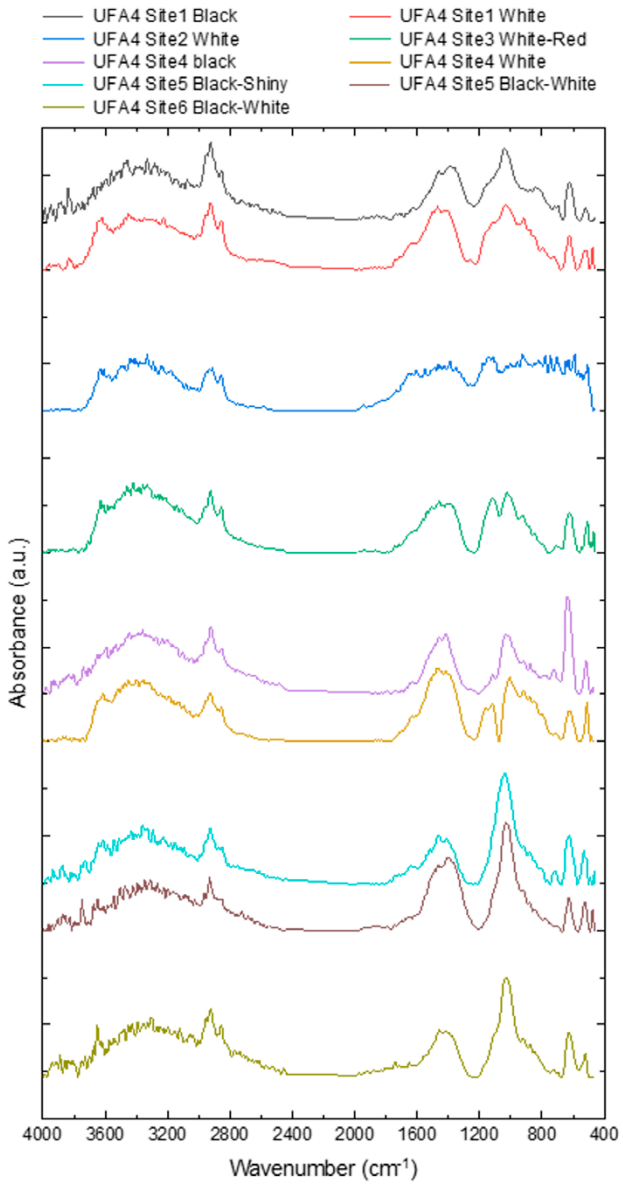

Figure 3-86. *Infrared spectra from FTIR/IRRAS measurement on surface of sample UFA4.*

3.5.2 Cross section analysis

SEM/EDS

The cross section samples were cut in half, cast into epoxy resin while mounted surface-to-surface, polished and analysed with SEM/EDS. Figures 3-87–3-89 were analysed after dry grinding. Figure 3-90–3-94 were analysed after diamond polishing. The cross section images show that the surfaces generally displayed a slightly rough appearance. The SEM images show a slightly thicker oxide layer than PC901 and LFA2. The EDS result show signs of sulfur being present in the cross section of the sample with a tendency of enhanced levels farther out in the oxide layer (Figure 3-90). As there only seem to be minimal amounts of bentonite present in this micrograph, and since the levels of calcium and iron are very low, the most likely origin of the enhanced levels of sulfur is the sulfidation of the underlying copper oxide film and the resulting formation of copper sulfide. Molybdenum was detected in Figure 3-91 scan 11. Due to overlapping peaks in the EDS spectra molybdenum could be a misidentification of sulfur.

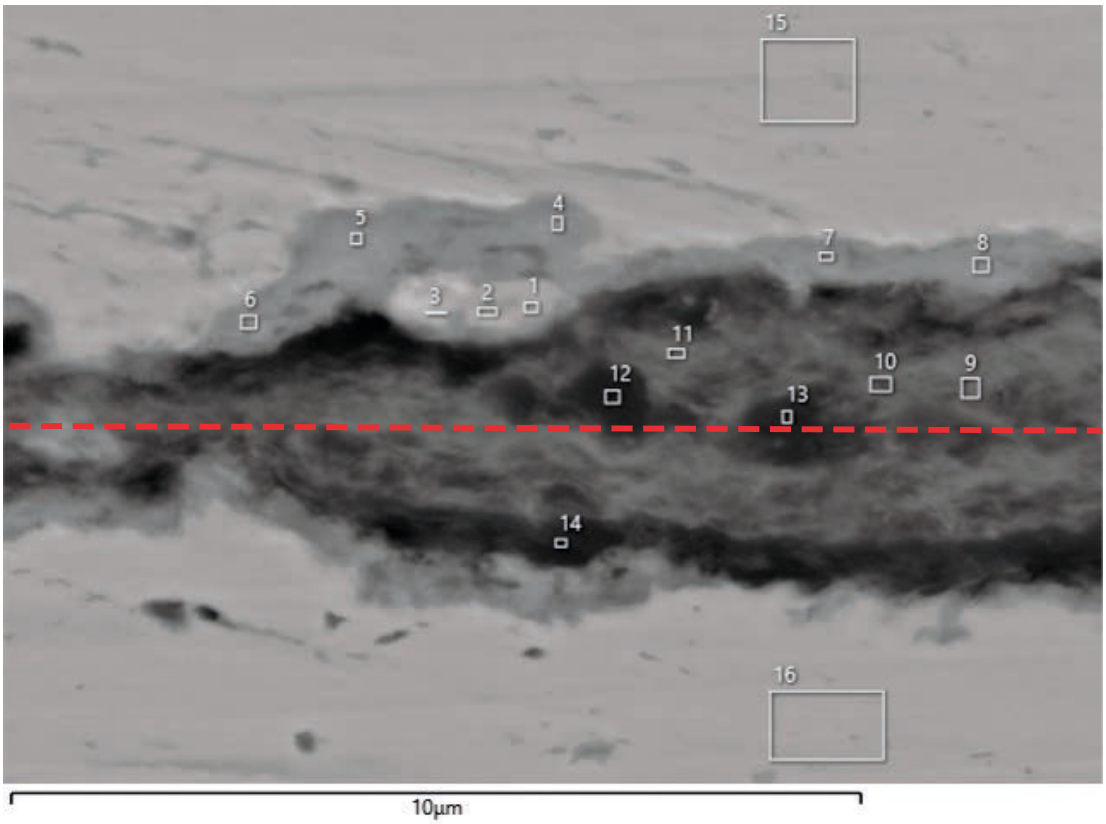

Element (At %)	1	2	3	4	5	6	7	8	9	10	11	12	13	14	15	16
O	9.94	8.47	7.8	7.87	9.88	12.98	12.39	12.33	26.31	28.89	28.64	44.99	47.93	34.97		
Na														0.33		
Mg	0.35	0.32	0.43			0.46			0.89	0.84	0.89	0.89	0.89	1.49		
Al	1.21	1.28	1.2		0.42	1.87	1.09	1.03	3.74	3.95	4.15	1.53	1.57	7.06		
Si	2.19	2.24	2.43	0.24	1	4.17	2.57	2.43	9.13	10.2	10.34	4.43	4.03	17.2		
S	0.15			0.31	1.2	1.04	0.94	0.94	0.54	0.57	0.53	0.73	0.96	0.74		
Cl	0.51	0.26	0.19	1.98	1.71	1.3	1.55	1.48	0.22	0.16	0.29	0.18	0.09	0.24		
K										0.18	0.15		0.22	0.16		
Ca	0.17	0.13			0.25	0.23	0.2		0.3	1.91	2.09	25.95	27.11	2.21		
Ti														0.17		
Mn												0.57	0.6			
Fe	0.13				0.23	0.41	0.27	0.32	0.7	0.74	0.75	0.49	0.44	1.74		
Cu	85.36	87.32	87.94	89.61	85.3	77.55	80.99	81.48	58.18	52.55	52.17	20.25	16.16	33.68	100	100
Total	100	100	100	100	100	100	100	100	100	100	100	100	100	100	100	100

Figure 87. *SEM image of the cross section of UFA4. The image shows the two surfaces of the cross section sample mounted surface to surface. This method was chosen to protect the oxide layer during polishing of the sample. A red dashed line indicates the rough location of the half way point. The EDS result of the cross section of UFA4 is shown in the table.*

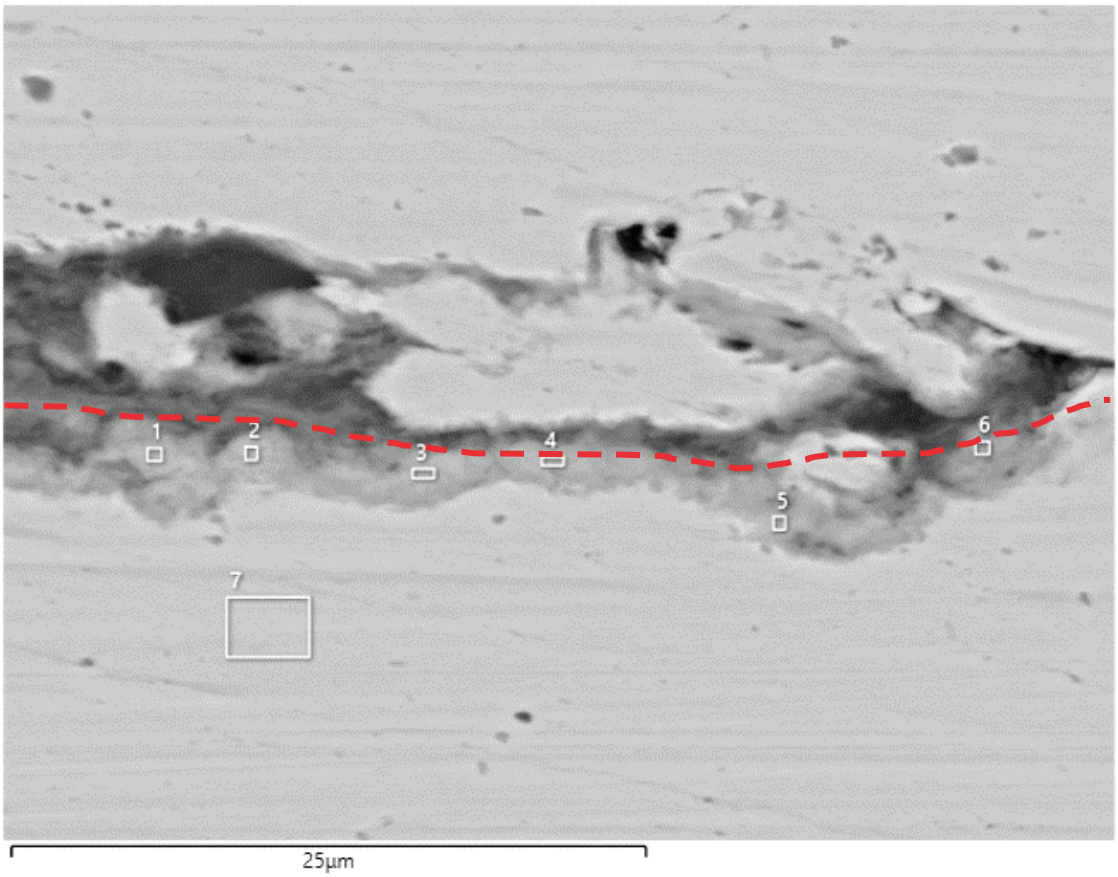

Element (At%)	1	2	3	4	5	6	7
O	14.41	12.5	11.62	11.39	12.05	22.29	
Mg						0.39	
Al	0.42	0.85	0.23	0.26	0.25		
Si	1.19	1.82	0.61	0.78	0.32	3.51	
P		0.11					
S	1.19	1.65	1.97	1.83	1.48	0.4	
Cl	0.98	0.99	1.21	1.14	1.07	0.4	
Ca	0.3	0.2	0.15	0.33	0.67	0.34	
Cu	81.5	81.88	84.21	84.26	84.15	70.24	100
Br						2.43	
Total	100	100	100	100	100	100	100

Figure 3-88. *SEM image of the cross section of UFA4. The image shows the two surfaces of the cross section sample mounted surface to surface. In this image a copper particle seems to be present between the two surfaces. A red dashed line indicates the rough location of the separation of the two surfaces. The EDS result of the cross section of UFA4 is shown in the table.*

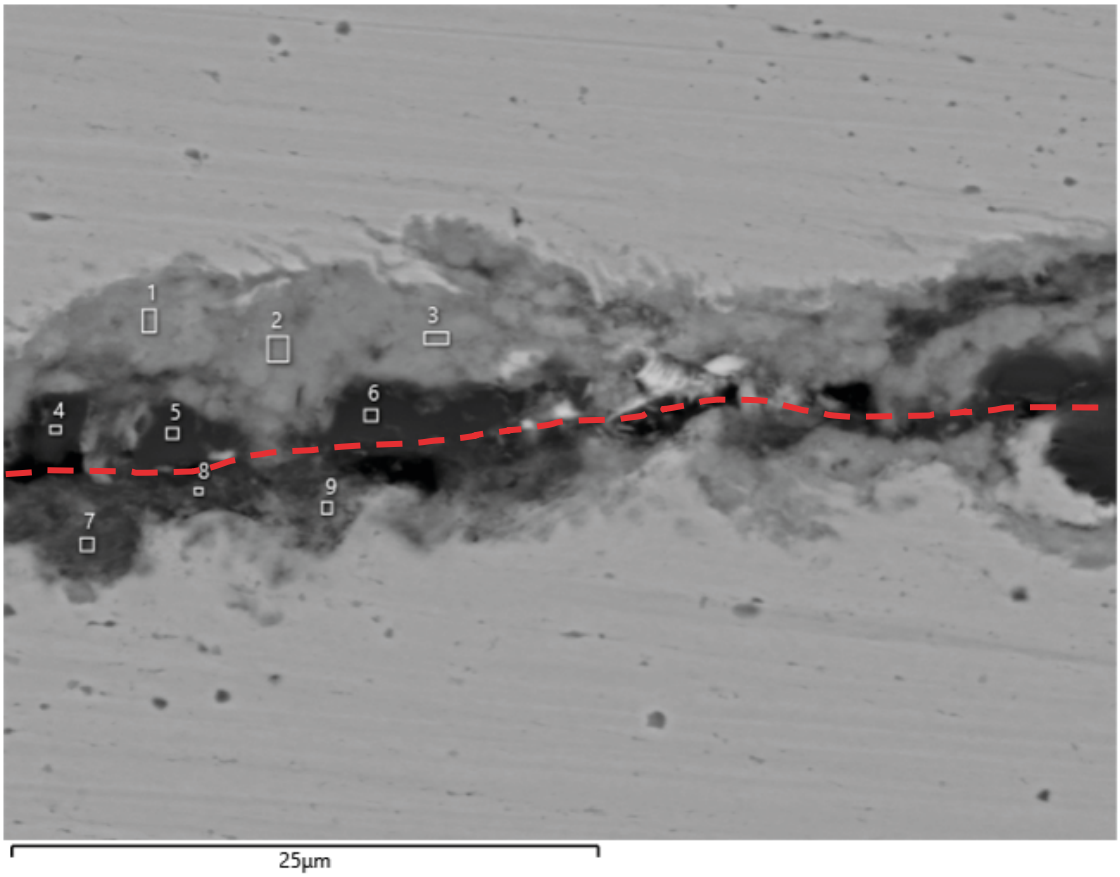

Element (At%)	1	2	3	4	5	6	7	8	9
O	14.49	18.09	18.61	44.77	5.11	3.3	31.03	28.02	19.95
Na				1.07					
Mg				1.26				1.08	0.88
Al	0.17	0.36		6.62	0.23		7.13	5.52	4.66
Si	0.53	1.09	0.56	24.99	89.8	93.67	18.12	21.65	15.78
P							0.09		
S	0.59	0.38		0.18			0.73	1.39	1.53
Cl	1.17	1.6	1.2	0.2	0.3		1.97	1.12	1.85
K				0.12			0.16	0.14	0.19
Ca		0.2		14.4			0.77	0.86	1.37
Ti				0.31				0.13	
Fe		0.2		0.36			1.71	1.4	1.59
Cu	83.05	78.08	79.64	5.71	4.55	3.03	38.29	38.69	52.21
Total	100	100	100	100	100	100	100	100	100

Figure 3-89. *SEM image of the cross section of UFA4. The image shows the two surfaces of the cross section sample mounted surface to surface. A red dashed line indicates the rough location of the separation of the two surfaces. The EDS image of the cross section of UFA4 is shown in the table.*

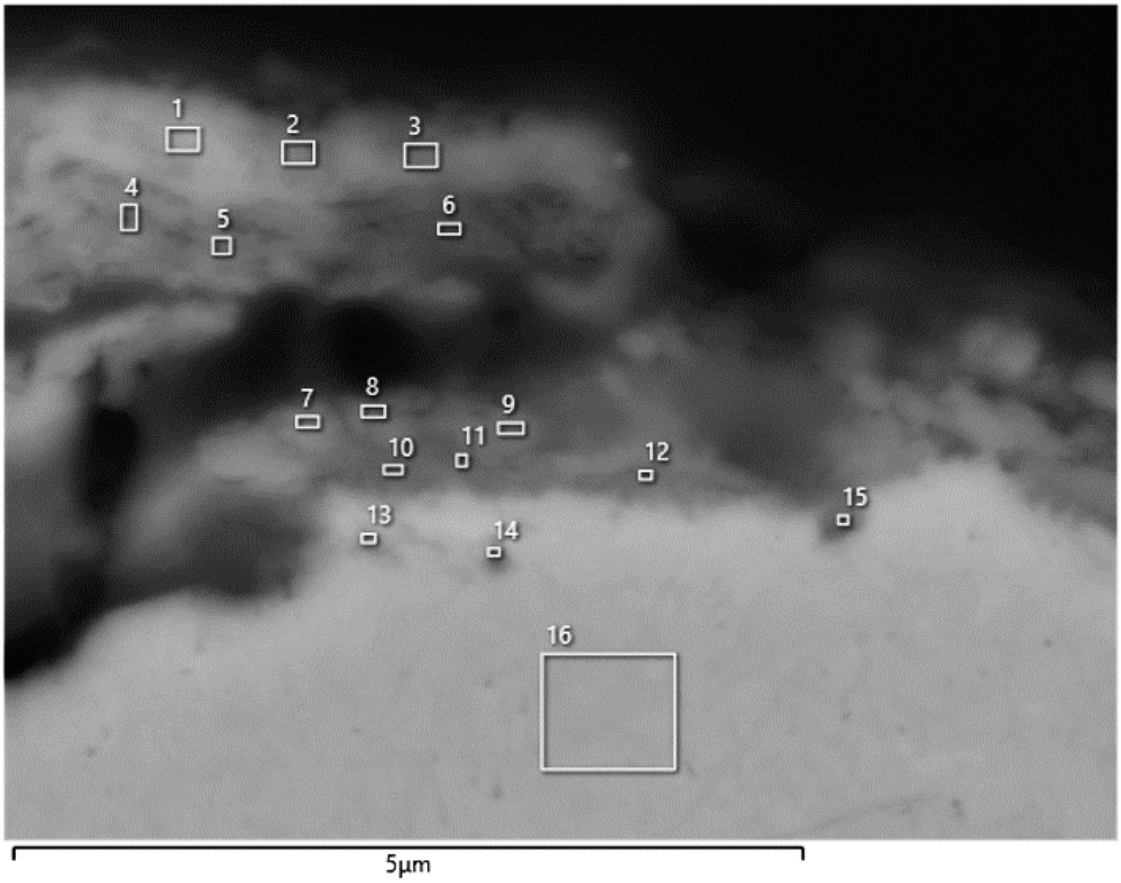

Element (At%)	1	2	3	4	5	6	7	8	9	10	11	12	13	14	15	16
O	29.44	29.32	30.03	29.18	28.21	27.06	44.33	43.68	48.04	39.13	41.18	35.23	23.44	17.26	27.8	
Mg	1.3	1.31	1.77	0.94	1.04	1.99	0.85	1.02	1.06		0.77	0.83				
Al	0.37	0.38	0.36			0.4		0.1								
Si	0.8	0.85	1.05	0.88	0.62	1.02	2.12	2.44	5.65	3.74	4.18	2.96	1.04	1.05	2.72	
P	0.4	0.65	0.74	0.47	0.39	0.61	0.22	0.27	0.28		0.24	0.25				
S	12.48	13.07	12.59	10.59	11.11	10.68	4.22	4.3	4.11	3.04	3.13	3.01	1.37	1	1.92	
Cl	0.65	0.75	0.79	0.75	0.73	0.81	0.7	0.73	0.6	0.74	0.64	0.62	0.32	0.25	0.37	
Ca	0.3	0.46	0.42	0.31	0.31	0.46	0.25	0.24	0.26	0.2	0.19	0.22	0.15			
Cu	54.26	53.21	52.25	56.88	57.58	56.96	47.31	47.22	40.02	53.17	49.67	56.88	73.68	80.44	67.18	100
Total	100	100	100	100	100	100	100	100	100	100	100	100	100	100	100	100

Figure 3-90. *SEM image of the cross section of UFA4, diamond polished. The EDS result of the cross section of UFA4, diamond polished, is shown in the table.*

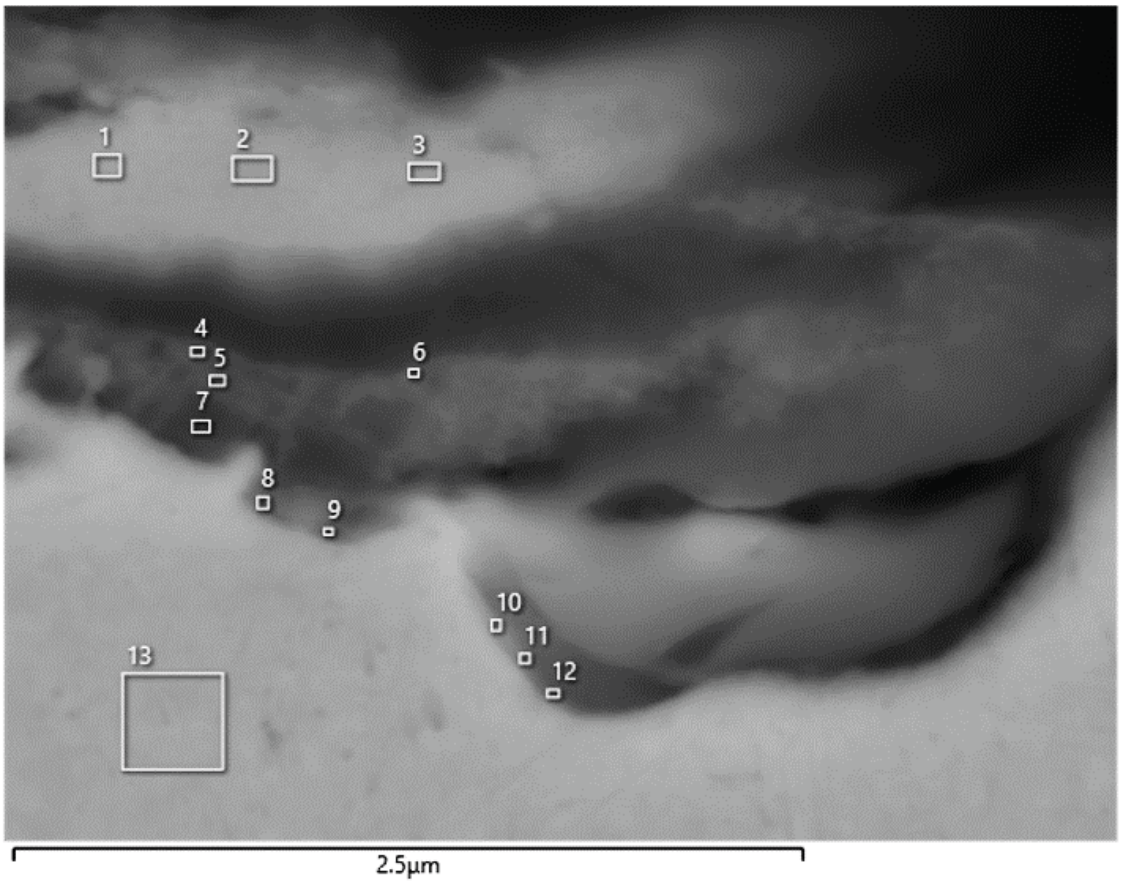

Element (At%)	1	2	3	4	5	6	7	8	9	10	11	12	13
O	42.85	42.05	43.35	48.07	47.17	50.95	46.59	34.06	29.06	15.16	13.8	17.52	
Mg		0.47	0.73	0.54	0.5	0.44	0.64						
Al			0.29										
Si	0.67	1.6	1.16	0.63	0.62	0.65	0.46	0.38			0.28	0.51	
S	2.54	2.58	2.78	3.46	3.5	3.65	3.4	1.73	1.31	0.41		0.56	
Cl	0.69	0.65	0.67	0.49	0.46	0.4	0.43	0.27	0.27				
Ca	0.32	0.25	0.28	0.31	0.31	0.28	0.18	0.12					
Cu	52.92	52.39	50.75	46.51	47.44	43.63	48.3	63.44	69.37	84.43	85.56	81.41	100
Mo											0.37		
Total	100	100	100	100	100	100	100	100	100	100	100	100	100

Figure 3-91. *SEM image of the cross section of UFA4, diamond polished. The EDS result of the cross section of UFA4, diamond polished, is shown in the table.*

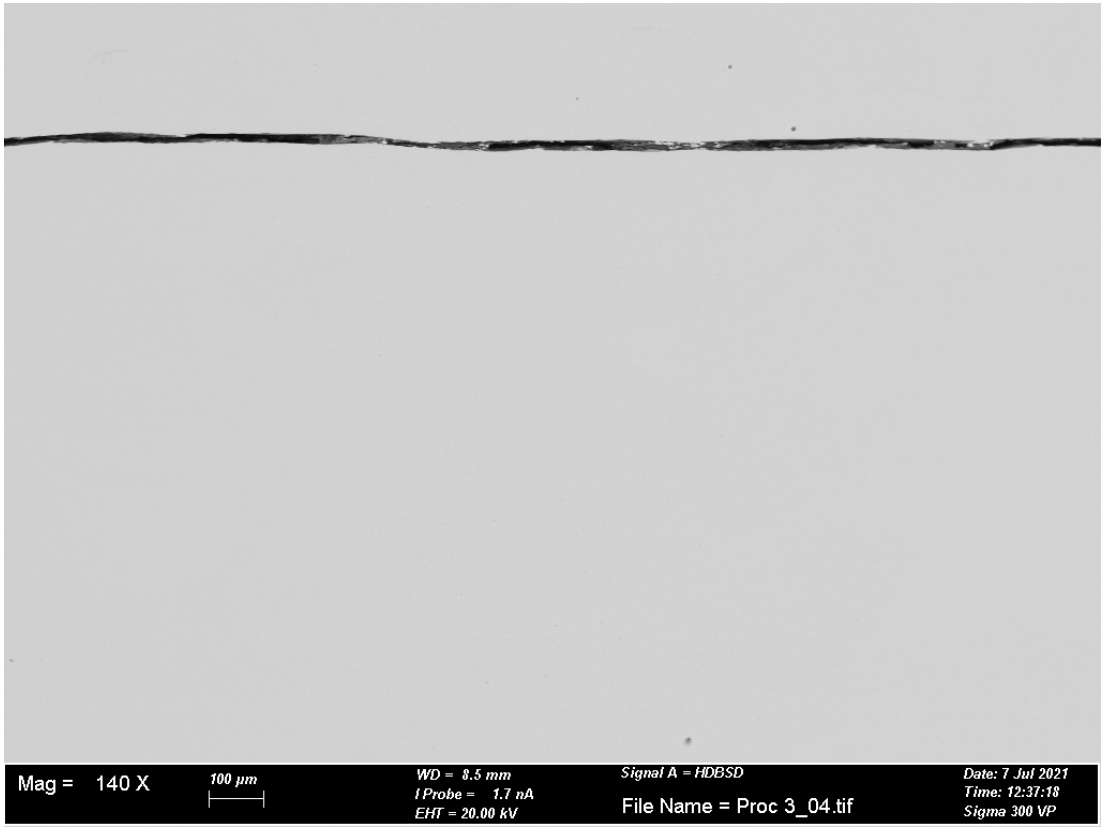

Figure 3-92. *SEM image overview of cross section mounted in epoxy resin surface to surface at ×140 magnification, UFA4.*

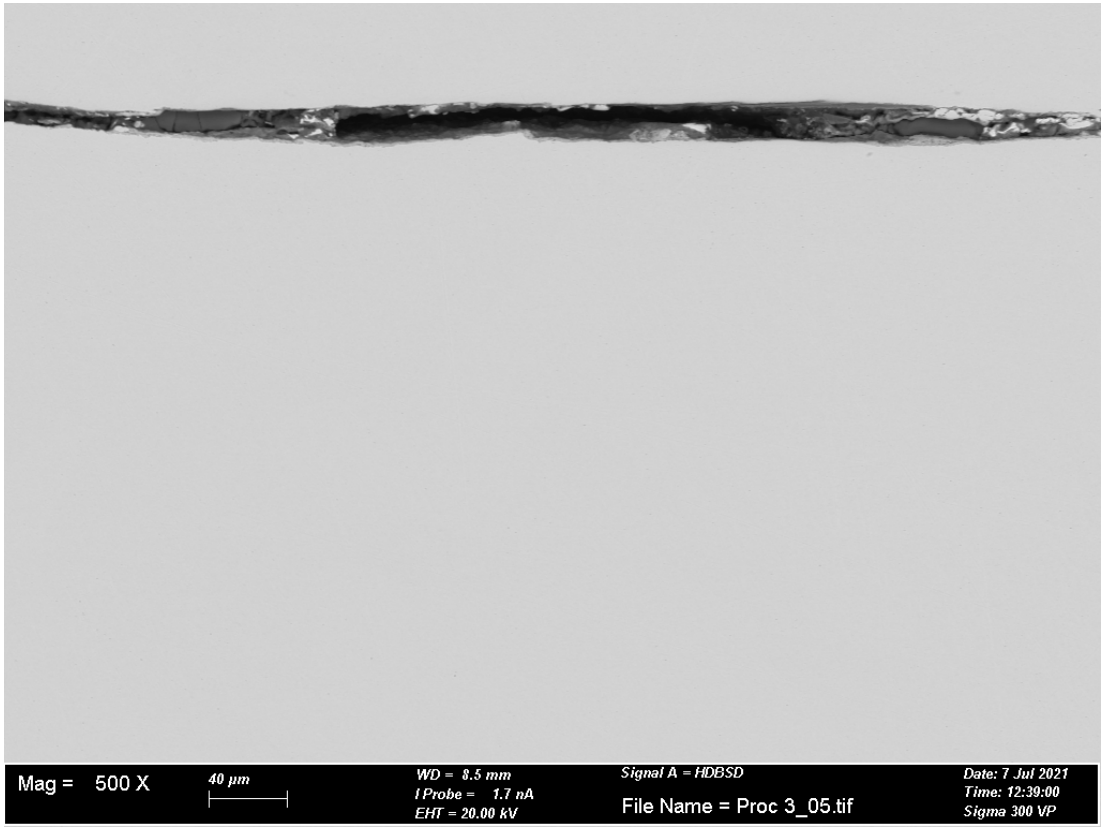

Figure 3-93. *SEM image overview of cross section mounted in epoxy resin surface to surface at ×500 magnification, UFA4.*

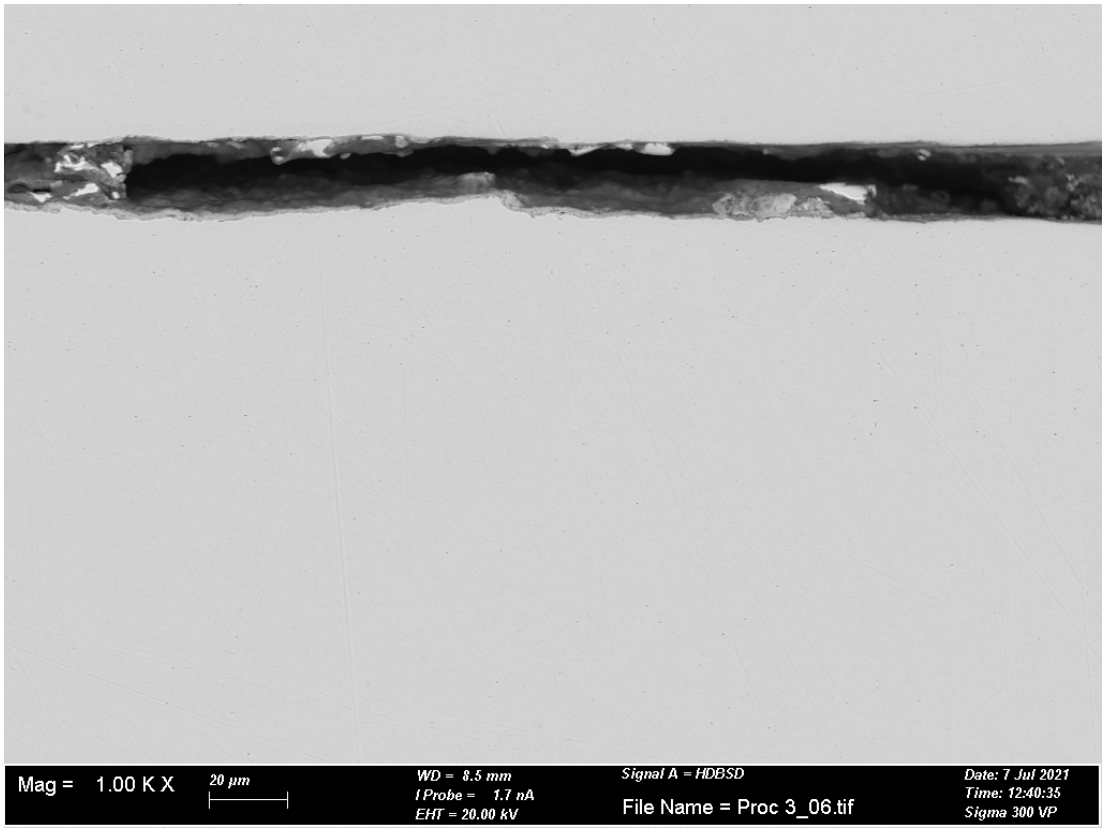

Figure 3-94. *SEM image overview of cross section mounted in epoxy resin surface to surface at ×1 000 magnification, UFA4.*

3.6 Examination of canister mantle surface

The Lasgit canister surface was examined by SKB staff in April 2021, i.e. a few months after retrieval when it was kept at the Canister Laboratory in Oskarshamn. The canister surface was documented by taking photographs of areas with typical appearance indicating different compositions of corrosion products and/or surface deposits.

It was generally found that the canister surface had small dark brown or black patches, of which some had a green-blue interior (Figure 3-95). Another common feature of the canister surface was the dark reticulated pattern seen e.g. on the canister surface in Figure 3-1d, on the filter housings LFA2 and UFA4 in Figure 3-1c and 3-1d, as well as on the canister base in Figure 3-95.

Close-up photos were taken of the different type areas and the deposits were removed in order to see how it had affected the underlying copper surface. Typical dark patches are shown in Figure 3-96, which is a detail from the canister base near the position of the filter housing PC901. As can be seen in Figure 3-1a, the same type of dark patches were found on the filter housing. In the photo depicted in Figure 3-96, the dark deposits have been scraped off at three positions, clearly revealing the band pattern from the machining of the canister components and showing that at these positions any influence of corrosion was, at most, less than the depth of the original deformation of the surface caused during manufacturing.

An example of an area with typical green-blue corrosion products is shown in Figure 3-97. Some of the deposit was scraped of using a scalpel. The deposit was found to be very loosely attached to the surface, easily flaking off when scraping the area, and the underlying copper surface displayed the band pattern resulting from machining of canister components.

An example of an area displaying the dark reticulated pattern is shown in Figure 3-98. As can be seen in the middle of the photo, part of the deposit forming the pattern was scraped off using a scalpel and just as for the other types of corrosion products and deposits found, no visible corrosion of the underlying copper surface was observed.

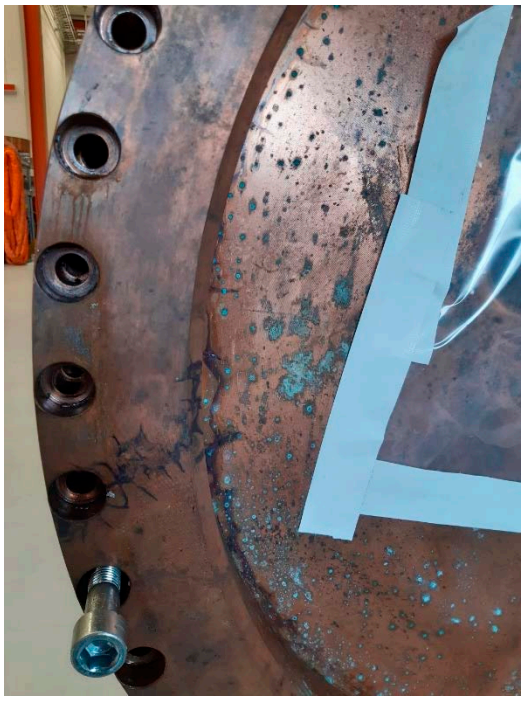

Figure 3-95. *Canister base after retrieval.*

Figure 3-96. *Close-up of area of the canister base, with dark patches near the position of PC901.*

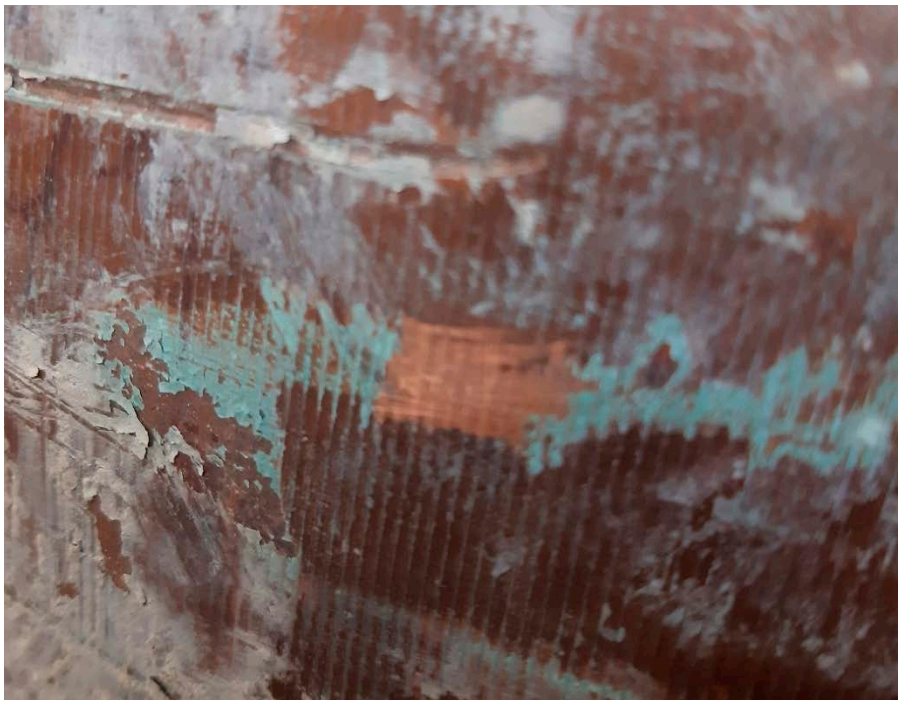

Figure 3-97. *Close-up of area with green-blue deposits, of which some has been removed using a scalpel.*

Figure 3-98. *Close-up of area with the typical dark reticulated pattern. Some of the deposit has been removed using a scalpel.*

The state of the Lasgit canister upon deposition is shown in three photographs in Figure 3-99. Figure 3-99a shows the lower part of the canister upon deposition, displaying one filter assembly and the axial purple markings spaced by 45° for filter assembly placement. In Figure 3-99b, filter assembly FLA4 is visible in the bottom left part of the image and the total stress sensor PC902 is visible in the top right part of the image. Additionally, in Figure 3-99b, a green-blue line of corrosion products can vaguely be seen above the total stress sensor, indicated by a black arrow. This line of corrosion products is also visible in the bottom part of Figure 3-99c, showing the Lasgit canister in the Äspö HRL tunnel before deposition. An additional, larger green-blue area is clearly visible in Figure 3-99c, partly covering filter assembly MPFA3. It is thus clear that some green-blue copper corrosion products were already present on the canister upon deposition. The same region where the green-blue corrosion products are observed in Figure 3-99c is also marked with a black rectangle in Figure 1-3c, here, the corrosion products are no longer clearly visible. Additionally, the large region of green-blue corrosion products partly covering filter assembly MPFA3 in Figure 3-99c is not visible on the same filter housing upon retrieval of the canister on January 25, as clearly shown in Figure 1-3a. By this comparison, the corrosion products from before deposition of the Lasgit canister are much less visible on the canister after retrieval.

Since it was observed that green-blue corrosion products were present on the canister upon deposition, and seemed to have diminished to some extent during deposition, it is interesting to investigate the origin of the green-blue corrosion products present after retrieval of the canister to the Canister Laboratory. It should be noted that approximately one month passed between retrieval of the canister form the deposition hole until it was brought to the Canister Laboratory. During this time, the canister was exposed to the ambient atmosphere of the Äspö HRL tunnel. The area marked with a grey rectangle in Figure 1-3 is where the material characterised with XRD (and imaged with optical microscopy – Figure 2-2) was sampled. A close-up photograph of the same area is shown in Figure 3-100b, which also clearly shows the reticulated pattern, which could be suggested to be templated from saturated bentonite. Such templating may have resulted from the gas injection leading to a gas flow along the bentonite–canister interface rather than through the bentonite. This was suggested by Harrington et al. (2008) seeing as the initial gas flow occurred at 775 kPa, much lower than what would be expected from gas flow through saturated bentonite. Such a gas flow along the canister wall could be perceived to locally dry and crack the bentonite, leading to flow channels which would eventually fill with pore water, and the eventual formation of a thin cuprite film.

The left-hand side of Figure 3-100a shows the same area as in Figure 3-100b, however when the Lasgit canister is being retrieved from the deposition hole. It should again be noted that the two images (showing partly the same area) are taken roughly one month apart, with Figure 3-100a taken first upon retrieval. It can thus be concluded that the green-blue corrosion products observed in Figure 3-100b, and characterised with XRD, formed after canister retrieval but before examination at the Canister Laboratory. It can, however, not be excluded that similar-looking corrosion products noted on other parts of the Lasgit canister may have formed during the course of the Lasgit experiment.

A scrape sample was taken from the large area of green-blue deposits marked with a grey rectangle in Figure 1-3c. A close-up of the sample is shown in Figure 2-2. The sample was examined using XRD and XRF. In the evaluation of the XRD data (Figure 3-101) the dominant phase was identified as paratacamite (possibly clinoatacamite; a chemically very similar mineral). Both can be expressed as $Cu_2(OH)_3Cl$. The minor phases were calcite and halite, and in the low angle region some smectite reflections were probably present, however the intensity is in the range of the background noise. The XRD reference data used for identification were halite (COD 96-900-8679), calcite (ICSD 98-016-9917), paratacamite (COD 96-900-7605), clinoatacamite (ICSD 98-026-0350) and atacamite (ICSD 98-015-3706). Formation of paratacamite as a copper corrosion product in chloride rich waters is not unexpected (Huttunen-Saarivirtta et al. 2017, Johansson et al. 2020, Karnland et al. 2009). It is therefore concluded that the observed paratacamite formed from oxic corrosion after retrieval and during the one month storage in the deposition tunnel, which had a temperature of 10–16 °C and a humidity of 52–82 %RH (see Appendix B). The source of chloride could either have been groundwater during the exposure in the deposition hole, or groundwater dripping onto the canister during storage in the Äspö tunnel after retrieval. The latter is considered more probable, as these corrosion products appear patch-wise on the canister.

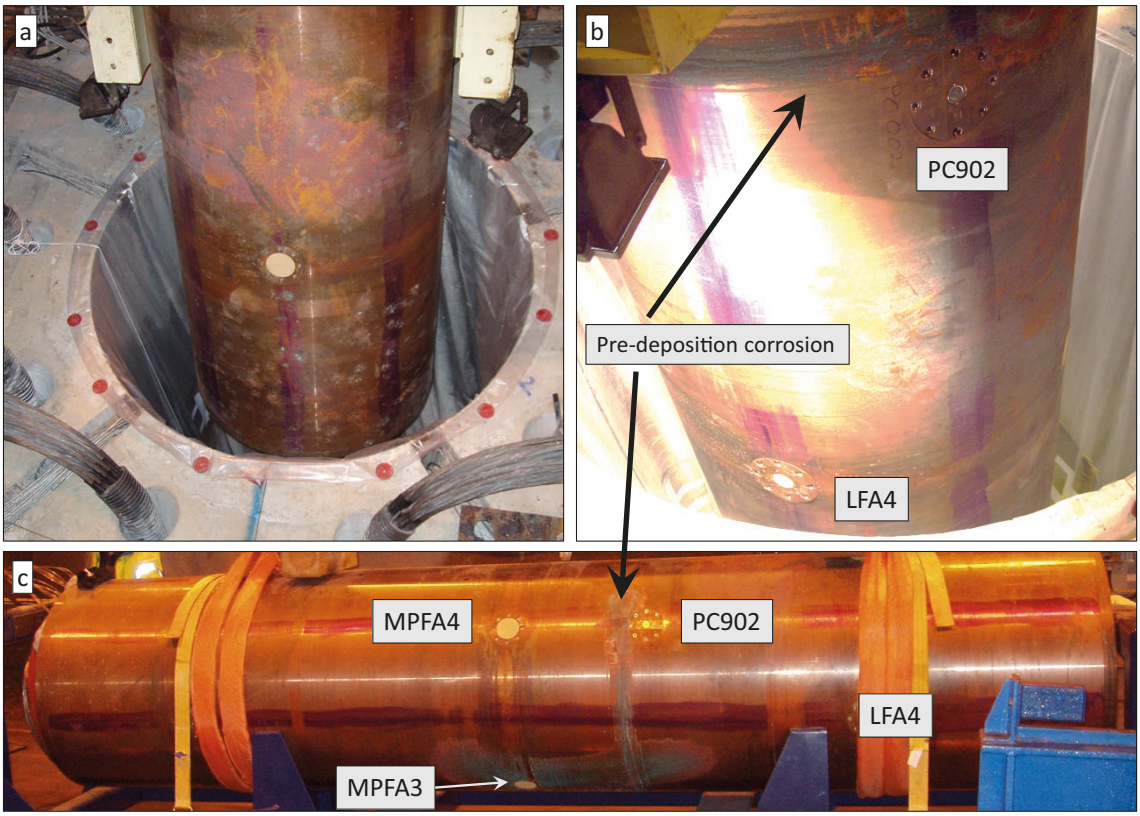

Figure 3-99. *The pictures show the Lasgit canister before deposition, (a) showing the bottom part of the canister, (b) showing the bottom part as well as the total stress sensor PC902, (c) showing a side view of the entire canister highlighting the presence of green-blue corrosion products on the canister at deposition.*

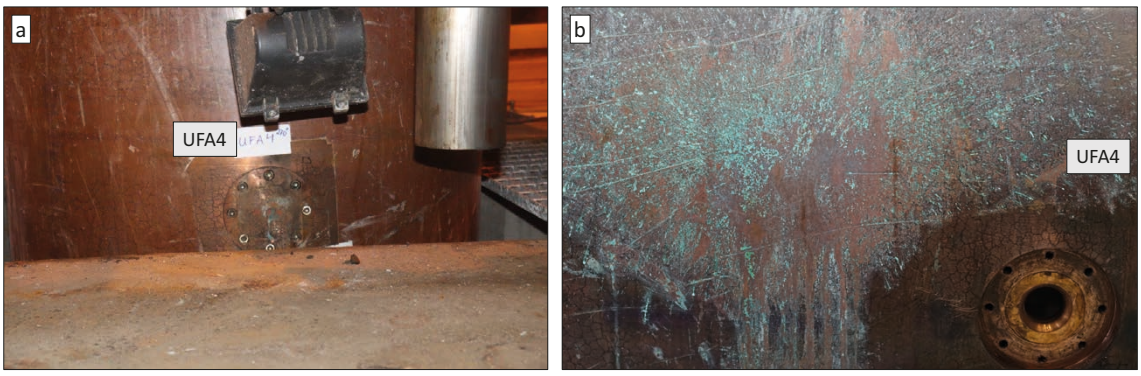

Figure 3-100. *The same area of the Lasgit canister photographed directly upon retrieval from the deposition hole at the Äspö HRL (a), and after arrival to the Canister laboratory in Oskarshamn (b). Note that the image to the left was taken roughly one month prior to the image to the right.*

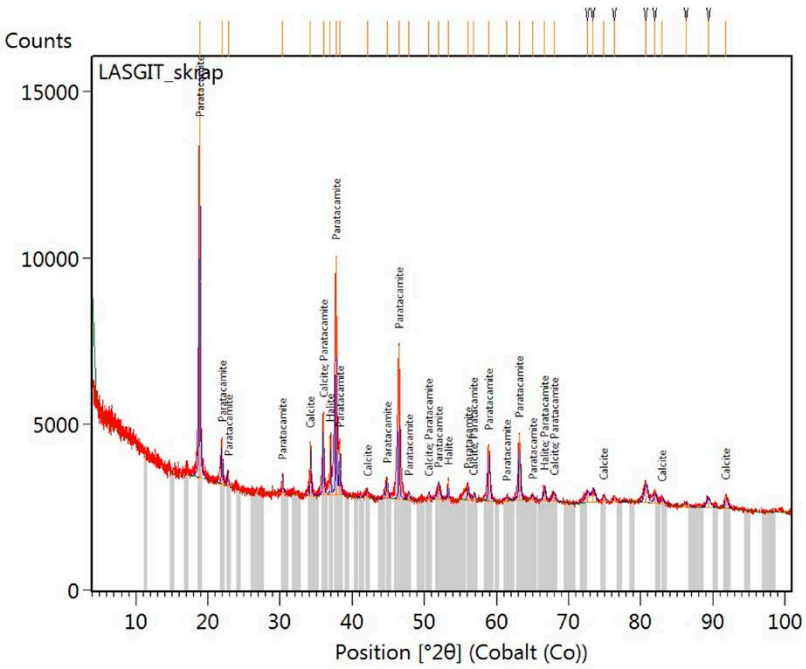

Figure 3-101. *XRD pattern of the scraping sample from the Lasgit canister surface. The reflections are marked with corresponding phases.*

Analysis with XRF confirmed the chemical interpretation of the XRD data. The sample was dominated by Cu (64 wt% CuO), Cl (20 wt%) and Ca (9 wt% CaO). Minor levels of Mg, Si and Al indicate that there are some low levels of smectite present in the sample, as expected due to the bentonite contact with the canister. The Si/Al ratio of the scraping sample was 2.95, which is very close to the 2.97 of a MX80 sample, a similar but not identical bentonite to one used in the experiment (Table 3-2). The Al and Si content of the scraping sample indicated that it contains approximately 4 wt% montmorillonite.

Table 3-2. XRF data of the scraping sample. All values in wt%. Scraping I and II indicate two preparations and measurements of the same powdered sample.

Identifier	Na_2O	MgO	Al_2O_3	SiO_2	P_2O_5	SO_3	Cl	K_2O	CaO	TiO_2	MnO	Fe_2O_3	CuO
Lasgit scrpaing I		0.78	1.16	3.21	0.71	1.13	19.91	0.11	8.77	0.04	0.02	0.56	63.62
Lasgit scraping II		0.34	0.67	2.18	0.32	1.16	20.62	0.11	10.04	0.05	0.02	0.58	63.59
Average		0.56	0.91	2.70	0.51	1.15	20.26	0.11	9.40	0.04	0.02	0.57	63.60
Std dev		0.22	0.24	0.51	0.20	0.02	0.36	0.00	0.64	0.00	0.00	0.01	0.01
MX80 batch 2015 SKB sample id c65ef8	1.82	2.45	22.05	65.56	0.01	0.58	0.00	0.67	1.66	0.22	0.02	4.97	0.00

3.7 Microbially influenced corrosion of cast iron

A filter housing at the base of the canister was opened for the first approximately 20 days of artificial hydration. This led to the presence of stagnant water in the canister insert, which in turn resulted in extensive corrosion of the insert base (Figure 2-3). The composition of the iron corrosion products were not characterized, however, samples were taken to investigate the possible presence of sulfate reducing or sulfur oxidizing bacteria. The amount of water which entered the canister as a result of the open filter housing can be estimated to approximately 7 cm from the distinct line of corrosion on the cast iron insert in Figure 2-3(c). The circular hole in Figure 2-3(a) and (b) was connected to the filter assembly, whereas the water inlet occurred through the filter housing situated in the square-shaped hole visible in Figure 2-3(b).

The results presented in Table 3-3 show the presence of 1.4 to 25 million bacteria per gram of sampled material, distributed as 1.4–1.6 million in the corrosion products and 25 million in the water. Additionally, a smaller number of archaea (approximately 100 000 per gram) was collected from the copper plate sample. The analysis displayed the presence of sulfur oxidizing bacteria in the sample from the copper plate and in the water sample.

Table 3-3. Summary of the QuantArray®-MIC results obtained for samples copper canister, cast iron insert, and water. Estimated gene copies above PQL are highlighted with bold text.

Sample name **Sample date**	**Copper canister** **14/04/2021**	**Cast iron insert** **14/04/2021**	**Water** **14/04/2021**
Microbially Induced Corrosion	*cells/g*	*cells/g*	*cells/c*
Total Bacteria (EBAC)	**1.64E+06**	**1.42E+06**	**2.52E+07**
Total Archaea (ARC)	**3.17E+05**	<2.00E+04	<1.00E+04
Sulfate Reducing Bacteria (APS)	< 2.00E+04	<2.00E+04	<1.00E+04
Sulfate Reducing Archaea (SRA)	<2.00E+04	<2.00E+04	<1.00E+04
Methanogens (MGN)	<2.00E+04	<2.00E+04	<1.00E+04
MIC Hydrogenase (MicH)	<2.00E+04	<2.00E+04	<1.00E+04
TatC Translocase (TatC)	<2.00E+04	<2.00E+04	<1.00E+04
Acetogens (AGN)	<2.00E+04	<2.00E+04	<1.00E+04
Fermenters (FER)	<2.00E+04	<2.00E+04	<1.00E+04
Iron Reducing Bacteria – Other (IRB)	<2.00E+04	<2.00E+04	<1.00E+04
IRB *Geobacter* (IRG)	<2.00E+04	<2.00E+04	<1.00E+04
IRB *Shewanella* (IRS)	<2.00E+04	<2.00E+04	<1.00E+04
Iron Reducing Archaea (IRA)	<2.00E+04	<2.00E+04	<1.00E+04
Iron Oxidizers (FeOB)	<2.00E+04	<2.00E+04	<1.00E+04
Manganese Oxidizing Bacteria (MnOB)	<2.00E+04	<2.00E+04	<1.00E+04
Sulfur Oxidizing Bacteria (SOB)	**1.88E+03 (J)**	<2.00E+04	**1.31E+06**
Denitrifying Bacteria (nirK)	<2.00E+04	<2.00E+04	<1.00E+04
Denitrifying Bacteria (nirS)	<2.00E+04	<2.00E+04	<1.00E+04
Ammonia Oxidizing Bacteria (AMO)	<2.00E+04	<2.00E+04	<1.00E+04
Nitrite Oxidizing Bacteria (NOR)	<2.00E+04	<2.00E+04	<1.00E+04
Nitrogen Fixers (NIF)	<2.00E+04	<2.00E+04	<1.00E+04
Burkholderia cepacian Exopolysaccharide (BCE)	<2.00E+04	<2.00E+04	<1.00E+04
Deinococcus spp. (DCS)	<2.00E+04	<2.00E+04	<1.00E+04
Meiothermus spp. (MTS)	<2.00E+04	<2.00E+04	<1.00E+04

J = Estimated gene copies below PQL but above LQL (Lower and Practical Quantitation Limit)
< = Result not detected

4 Discussion

In general, it was found that the filter housings had corroded to a very limited extent. No signs of localized corrosion were observed at the macroscopic level, and in the samples of cross-sections examined by SEM, no clear signs of micro-scale localized corrosion was observed either. It should be noted that the Lasgit experiment was not intended for the detection or measurement of corrosion of the filter housings and as such the analyses carried out in this work were limited to the material available which was not ideal for the study of corrosion mechanisms or quantification.

The scrape samples of green-blue copper corrosion products, characterised with XRD, can be concluded from photographs to have formed between retrieval of the Lasgit canister from the deposition hole and characterisation at the Canister Laboratory. It can also be concluded that some areas of similar green-blue corrosion products were already present on the Lasgit canister upon deposition and experiment initiation. These corrosion products were barely visible upon characterization at the Canister Laboratory, as shown by the comparison of the filter assembly MPFA in Figure 3-99c and Figure 1-3a, before and after deposition, respectively. It has not been possible to identify the nature of the green-blue corrosion products present during deposition. In Figure 3-99c, the filter assembly in the bottom part of the canister is partly covered by the green-blue corrosion products. The same area is shown in Figure 1-3a without the green-blue corrosion products. Figure 1-3a instead displays an area of darker corrosion products. It can, however, not be concluded that all of the observed instances of green-blue corrosion products documented after canister retrieval (for example shown in Figure 3-95–3-97) actually formed after canister retrieval. It also cannot be concluded that all green-blue corrosion products on the canister are indeed paratacamite, as the scrape sample, since also malachite was observed on the filter houses.

SEM micrographs taken at magnification ×1 000 or lower, show a relatively smooth surface profile with shallow pits or other, possibly corrosion-induced, defects and a generally thin oxide film (e.g. Figures 3-27, 3-51, 3-70, 3-94). However, locally there are a few observations of up to 10 µm thick oxide (e.g. Figures 3-44–3-46) and 5 µm pits or defects (e.g. Figure 3-25). It is not possible to quantify with accuracy how much of this oxide that was present from prior to exposure, and how much that had formed due to corrosion during the exposure, or possibly after retrieval. No efforts were carried out to determining the specific influence of the rather unique starting conditions for the Lasgit experiment, with weakly oxidizing and saturated conditions, as it should be noted that such conditions are unlikely in the planned final repository. Two SEM micrographs taken normal to the P901 filter house surface, namely Figure 3-12 and 3-14, show EDS measurements of the entire micrograph, indicating a surface relatively free from bentonite. Here, there is roughly a 1:2 oxygen–copper relationship, suggesting a cuprite film with a thickness in the order of the penetration depth of the EDS i.e micron scale. This would indicate that it is possible, or even probable, that a cuprite film of this thickness is present throughout the copper, albeit in many cases covered by bentonite. At some smaller spots for the other filter housings, similar cuprite films could be inferred by the same argument, see spots 4–6 in Figure 3-36, spots 7–9 in Figure 3-54, and spots 7–9 in Figure 3-74. This correlates with the SEM cross sections, which display oxide layers in the range of a few, up to ten micrometres. It may be roughly estimated that, based on the shiny appearance of the filter housings in photos taken prior to the installation and exposure, the thickness of the initially present oxide may on average have been of the order of tens up to a few hundred nanometer (Leygraf et al. 2019).

The visual appearance of the as-received filter housings for analysis varied slightly, with different amounts of bentonite clay adhering to the surfaces, as well as some different nuances observed, particularly around the filters. Generally, the filter housings had a copper and light brown appearance, which, based on previous field studies (Gordon et al. 2017, Taxén et al. 2012, Johansson et al. 2020) suggests the presence of a film of cuprite. Under atmospheric conditions, a variety of compounds are expected to form and grow on top of an inner cuprite layer, depending on exposure conditions. Brochantite ($Cu_4SO_4(OH)_6$) or antlerite ($Cu_3(SO_4)(OH)_4$) could be expected at sulfur-polluted sites, whereas atacamite could be expected in the presence of chlorine (Fitzgerald et al. 2006, Krätschmer et al. 2002). In the present study, no brochantite or antlerite could be detected by XRD, and although sulfate was observed with FTIR, it cannot be confirmed as brochantite or antlerite. Similarly, in previous field experiment, no observations of brochantite or antlerite have been made (Gordon et al. 2017, Taxén et al. 2012, Johansson et al. 2020).

From the EDS analyses, mainly copper and oxygen was observed, with some sulfur present on the surfaces along with constituents of the bentonite clay (Si, Al). No copper sulfide (e.g. Cu_2S) corrosion products were identified in the XRD or FTIR analyses. However, a few instances of spots with elevated sulfur content were observed with EDS. At these spots, the sulfur content was not corresponding to an elevated level of Ca or Fe, which would be expected if the source of sulfur was $CaSO_4$ or FeS_2 from the bentonite clay. In these regions, sulfide corrosion or ongoing sulfidation (chemical substitution) of the Cu_2O film, could not be excluded as a perceivable cause for the enhanced level of sulfur. This is only inferred from the co-appearance of Cu, O, and S by EDS, as no Cu_2S could be identified by XRD or FTIR.

Since the XRD measurements probe at a depth of around 5 µm, and the corrosion product thicknesses for several samples were less than that, it could explain why only weak peaks of cuprite were observed. An increased signal from the surface layer could possibly be achieved by XRD at a grazing incidence, however, that is outside the scope of the current analysis. From the FTIR/IRRAS analyses, all samples had several sites that showed signs of bentonite, as signified by the large peak around 1 000 cm^{-1} (Si-O-Si) in combination with the smaller peak around 3 600 cm^{-1} (Al-OH). In addition to this, most sites also showed double peaks around 1 300–1 600 cm^{-1}, which could indicate malachite. PC901 showed signs of cuprite with a distinct (Cu-O) peak around 630 cm^{-1}, however, this peak only was visible in some areas in the other samples. No definitive detection of tenorite (CuO) was made, however, the possibility of its presence cannot be ruled out due to peak overlap between the different compounds. The samples LFA2, PC901, and UFA4 showed distinct peaks at 1 100–1 150 cm^{-1}, attributed to a sulphate group, which could possibly be adsorbed sulfate or precipitated $CaSO_4$ originating from the bentonite clay. Elemental analysis of the cross section of LFA2 showed that sulfur was present in the oxide layer. The lack of cuprite in the FTIR/IRRAS measurements could be due to the fact that the technique is optimized to measure thin films. Thick oxide layers can result in diffuse or bulk reflectance of the incoming IR-radiation which results in changes in signal intensity and peak shape. This means that data coming from the parts of the sample that is covered in thick oxides can be distorted.

The Lasgit canister was found to have contained a small amount of stagnant water resulting from a filter valve which was kept open for the first 20 days of the experiment. The extent of iron corrosion has been described in connection to Figure 2-3. The relevance of this occurrence for the safety case and further study of a scenario with a broken canister is minor. The open valve was closed after 20 days and from the corrosion line on the canister insert, the water level never reached above the level of the entry to the inlet–outlet tube at approximately 30 cm above the insert base. Thus, no further exchange of water is expected to have taken place between the canister and its environment, as a result of this open valve. The Cu-Fe galvanic corrosion in groundwater have been studied by Smart et al. (2005). If the groundwater contained oxygen, the rate of cast iron corrosion was very high, up to 100 µm per year. In oxygen-free water, the measured corrosion rates of cast iron galvanically coupled to copper were in the same range as those measured for cast iron in the absence of galvanic coupling to copper. In the Lasgit experiment it is possible that the water intruding the canister contained some amount of O_2, since the intrusion seems to have occurred rather early in the experiment, however, the period during which O_2 was available would probably have been very short due to O_2 consumption by corrosion.

Investigating the insert for evidence of microbial activity is of interest, as microbes are present where there is water. It is therefore no surprise to find microbial DNA in the water and corrosion products sampled from the interior of the canister, where stagnant water had accumulated. The applied analysis can detect the presence of live and inactive microbes, as long as their DNA is intact. Sulfur oxidizing bacteria oxidizes sulfide and elementary sulfur to sulfate or sulfuric acid. Their observed presence indicates that sulfide and/or sulfur has been present in the Lasgit canister. The origin of this sulfur could either have been sulfide from ground water, or from sulfate reduction within the canister during the Lasgit experiment. Sulfate reduction only takes place in anoxic environment. As the Lasgit experiment was terminated and the canister was opened towards the HRL tunnel air, sulfate reduction would be inhibited and sulfur oxidation could take place. Thus, sulfur oxidation would most likely have taken place after the Lasgit experiment was terminated and the inside of the canister was open to the HRL tunnel air as the filter assemblies were removed. The DNA analysis could detect inactive

sulfur oxidizing bacteria, however, since the inside of the canister was subjected to air for several months before sampling, it is probable that remnant DNA from inactive sulfate reducing bacteria was below the detection limit. Sulfur oxidation normally results in the formation of sulfuric acid, which may have accelerated the cast iron corrosion. It is thus probable that the corrosion observed on the inside of the copper base and cast iron insert has been influenced by the presence of microbial processes, especially sulfur oxidizing and sulfate reducing bacteria. However, it is difficult to quantify to what extent the observed corrosion, of the inside of the copper base and the cast iron insert, is caused by microbial processes and anoxic and/or oxic corrosion. As it was not regarded as vital for the study, no chemical analysis was performed to determine the nature of the corrosion products inside the canister.

5 Conclusions

Four filter housing from the Lasgit experiment were analyzed for corrosion using several complementary surface sensitive techniques. The nature of the experimental conditions, with presumed weakly oxidizing conditions initially and a saturated bentonite, limits the analytical value of the experiment in the safety assessment, since this combination of conditions is unlikely for the repository environment. This is additionally highlighted by the fact that the Lasgit experiment was not intended as a corrosion experiment, without pre-characterization of the included copper components.

The results of the analysis of the filter housings show that the extent of corrosion can be considered low and in accordance with experience from previous field experiments. Examination of cross-sectioned samples using SEM revealed thin layers of corrosion products and small, shallow pits or defects in the surfaces. The corrosion products cuprite, malachite, and paratacamite were identified, where the latter, which was only observed in a scrape sample, was concluded to have formed after retrieval of the canister.

References

SKB's (Svensk Kärnbränslehantering AB) publications can be found at www.skb.com/publications.

Cuss R J, Harrington J F, Noy D J, 2010. Large scale gas injection test (Lasgit) performed at the Äspö Hard Rock Laboratory. Summary report 2008. SKB TR-10-38, Svensk Kärnbränslehantering AB.

Cuss R J, Harrington J F, Noy D J, Birchall D J, Selling P, Nord M, 2022. Large scale gas injection test (Lasgit) performed at the Äspö Hard Rock Laboratory. Final report. SKB TR 22-06, Svensk Kärnbränslehantering AB.

Downs R T, Hall-Wallace M, 2003. The American Mineralogist crystal structure database. American Mineralogist 88, 247–250.

Fitzgerald K P, Nairn J, Skennerton G, Atrens A, 2006. Atmospheric corrosion of copper and the colour structure and composition of natural patinas on copper. Corrosion Science 48, 2480–2509.

Gordon A, Sjögren L, Taxén C, Johansson A J, 2017. Retrieval and post-test examination of packages 4 and 5 of the MiniCan field experiment. SKB TR-16-12, Svensk Kärnbränslehantering AB.

Gordon A, Pahverk H, Börjesson E, Johansson A J, 2018. Examination of copper corrosion specimens from ABM 45, package 5. SKB TR-18-17, Svensk Kärnbränslehantering AB.

Gražulis S, Chateigner D, Downs, R T, Yokochi A F T, Quirós M, Lutterotti L, Manakova E, Butkus J, Moeck P, Le Bail A, 2009. Crystallography Open Database – an open-access collection of crystal structures. Journal of Applied Crystallography 42, 726–729.

Gražulis S, Daškevič A, Merkys A, Chateigner D, Lutterotti L, Quirós M, Serebryanaya N R, Moeck P, Downs R T, Le Bail A, 2011. Crystallography Open Database (COD): an open-access collection of crystal structures and platform for world-wide collaboration. Nucleic Acids Research 40, D420–D427.

Gražulis S, Merkys A, Vaitkus, A, Okulič-Kazarinas M, 2015. Computing stoichiometric molecular composition from crystal structures. Journal of Applied Crystallography 48, 85–91.

Griffiths P R, de Haseth J A, 2007. Fourier transform infrared spectrometry. 2nd ed. Hoboken: NJ: Wiley-Interscience.

Harrington J F, Horseman S T, 2003. Gas migration in KBS-3 buffer bentonite. Sensitivity of test parameters to experimental boundary conditions. SKB TR-03-02, Svensk Kärnbränslehantering AB.

Harrington J F, Birchall D J, Noy D J, Cuss R J, 2008. Large scale gas injection test (Lasgit) performed at the Äspö Hard Rock Laboratory. Summary report 2007. CR/07/211N, British Geological Survey.

Huttunen-Saarivirta E, Rajala P, Bomberg M, Carpén L, 2017. EIS study on aerobic corrosion of copper in ground water: influence of micro-organisms. Electrochimica Acta 240, 163–174.

Johansson A J, Svensson D, Gordon A, Pahverk H, Karlsson O, Brask J, Lundholm M, Malmström D, Gustavsson F, 2020. Corrosion of copper after 20 years exposure in the bentonite field tests LOT S2 and A3. SKB TR-20-14, Svensk Kärnbränslehantering AB.

Karnland O, Olsson S, Dueck A, Birgersson M, Nilsson U, Hernan-Håkansson T, Pedersen K, Nilsson S, Eriksen T E, Rosborg B, 2009. Long term test of buffer material at the Äspö Hard Rock Laboratory, LOT project. Final report on the A2 test parcel. SKB TR-09-29, Svensk Kärnbränslehantering AB.

Koivula J, Pihlainen H, 2003. Further development of the structure and facrication of the final disposal canister. Test fabrication of a seamless overpack with an integrated bottom by pierce and draw process. Posiva Working Report 2003-49, Posiva Oy, Finland.

Krätschmer A, Odnewall Wallinder I, Leygraf C, 2002. The evolution of outdoor copper patina. Corrosion Science 44, 425–450.

Leygraf C, Chang T, Herting G, Odnewall Wallinder I, 2019. The origin and evolution of copper patina colour. Corrosion Science 157, 337–346.

Malvault J Y, Lopitaux J, Delahaye D, Lenglet M, 1995. Cathodic reduction and infrared reflectance spectroscopy of basic copper (II) salts on copper substrate. Journal of Applied Electrochemistry 25, 841–845.

Merkys A, Vaitkus A, Butkus J, Okulič-Kazarinas M, Kairys V, Gražulis S, 2016. COD::CIF::Parser: an error-correcting CIF parser for the Perl language. Journal of Applied Crystallography 49, 292–301.

Nieminen M, Pihlainen H, 2001. Development and manufacturing of a spent nuclear fuel disposal canister – seamless overpack, piece and draw method studied by test production and modeling. Posiva R&D Report 2001-17, Posiva Oy, Finland.

Quirós M, Gražulis S, Girdzijauskaitė S, Merkys A, Vaitkus A, 2018. Using SMILES strings for the description of chemical connectivity in the Crystallography Open Database. Journal of Cheminformatics 10. doi:10.1186/s13321-018-0279-6

Smart N R, Rance A P, Fennell P A H, 2005. Galvanic corrosion of copper-cast iron couples. SKB TR-05-06, Svensk Kärnbränslehantering AB.

Socrates G, 1994. Infrared characteristic group frequencies: tables and charts. 2nd ed. Chichester: Wiley.

Taxén C, Lundholm M, Persson D, Jakobsson D, Sedlakova M, Randelius M, Karlsson O, Rydgren P, 2012. Analyser av koppar från prototypkapsel 5 och 8. SKB P-12-22, Svensk Kärnbränslehantering AB. (In Swedish.)

Vaitkus A, Merkys A, Gražulis S, 2021. Validation of the Crystallography Open Database using the Crystallographic Information Framework. Journal of Applied Crystallography 54, 661–672.

Wersin P, Kober F (eds), 2017. FEBEX-DP. Metal corrosion and iron–bentonite interaction studies. Nagra Arbeitsbericht NAB 16-16, Nagra, Switzerland.

Appendix A

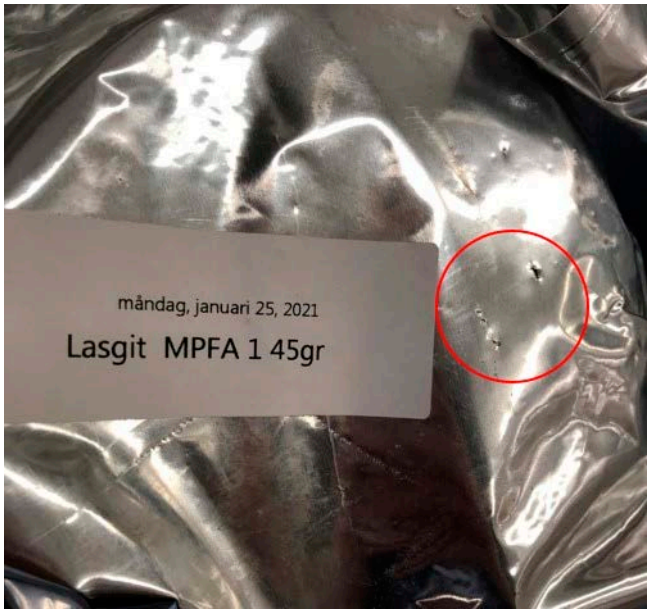

Figure A-1. *The Perforated foil package of filter housing MPFA1.*

Appendix B

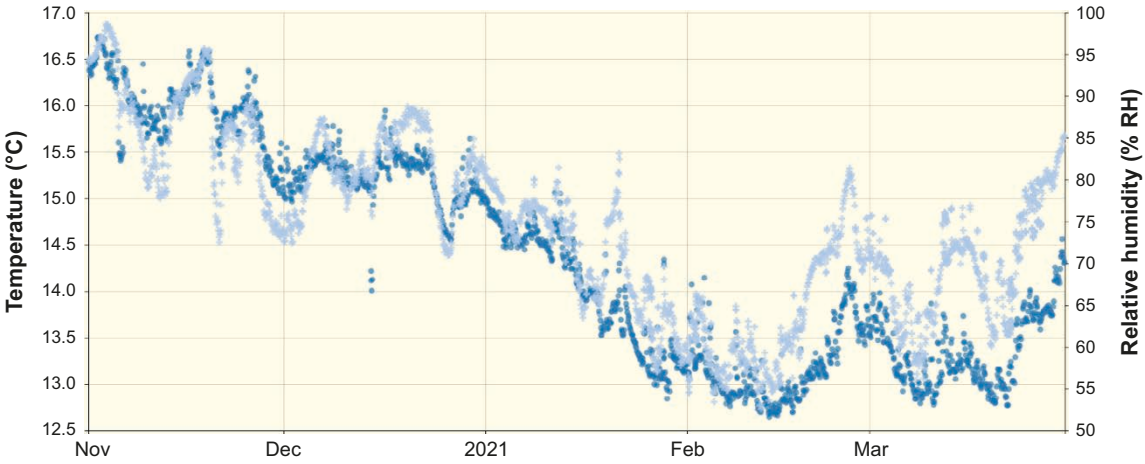

Figure B-1. *Temperature and relative humidity measured close to the Lasgit deposition hole, in the Äspö Hard Rock laboratory, where the Lasgit canister was stored for roughly one month prior to transport to the Canister Laboratory. The canister was stored in the tunnel between February and March, being subject to temperatures of 10–16 °C and humidity of roughly 52–82 %RH.*

Arkitektkopia AB, Bromma, 2022

SKB is responsible for managing spent nuclear fuel and radioactive waste produced by the Swedish nuclear power plants such that man and the environment are protected in the near and distant future.

skb.se